University of Liverpool

School of Engineering

Lattice Boltzmann modelling of immiscible two-phase flows

The Thesis is submitted in accordance with the requirements of Liverpool for the degree of Doctor in Philosophy

Author: Duo Zhang

August, 2015

Abstract

The scope of the current thesis is the comprehensive understanding of the droplet impact and spreading dynamics on flat and curved surfaces with the aim of simulating high density ratio immiscible two phase flows in porous media. Understanding the dynamic behavior of droplet impingement onto solid substrate can provide significant information about the fluid flow dynamics in porous structures. The numerically study process will be realized by using a high density ratio multi-phase lattice Boltzmann model which is able to simulate multi-phase flows in complex systems. The interfacial information between the two immiscible phases can be captured without tracking or constructing the vapour-liquid interface. A three dimensional lattice Boltzmann model is applied on the study of the impaction of a liquid droplet on a dry flat surface for a liquid-gas system with large density ratio. The impaction of liquid droplet on a curved surface for the liquid-gas system with large density ratio and low kinematic viscosity of the fluid is computed by a two-dimensional multi-relaxation-time (MRT) interaction-potential-based lattice Boltzmann model based on the improved forcing scheme. The dynamics behaviors of the spreading of the liquid droplet on the flat surface as well as the impaction of the liquid droplet on a curved surface are computed, followed by their dependence on the Reynolds number, Weber number, Galilei number and surface characteristics. Moreover, an improved force scheme is proposed for the three-dimensional MRT pseudopotential lattice Boltzmann model which is based on the improved force scheme for the Single relaxation time (SRT) pseudopotential lattice Boltzmann model and the Chapman-Enskog analysis. The validation for the new developed three-dimensional multi-relaxation time lattice Boltzmann model is carried out through Laplace's law ad by achieving thermodynamic consistency. In addition, the relationship between the fluid-solid interaction potential parameter G_w and the contact angle is investigated for the new developed three-dimensional MRT lattice Boltzmann model. The immiscible two-phase flow in porous media is carried out by a two dimensional MRT lattice Boltzmann model. The porous media structures with different geometrical properties are artificially generated by a Boolean model based on a random distribution of overlapping ellipses/circles. Furthermore, the impact of geometrical properties on the immiscible two-phase flows in porous media is investigated in the pore scale. The lattice Boltzmann model results provide significant information

on the interface between the two immiscible phases in complex systems, it is easy to apply for complex domains with bounce back boundary wall condition and be able to handle multi-phase and multi-component flows without tracing the interfaces between different phases.

Keywords: Multiphase flow, Lattice Boltzmann, High-density-ratio, Droplet impact, Porous media

Contents

List of Figures

List of Tables

Acknowledgement

This work couldn't have been accomplished without the guidance of my supervisors, help from friends, and the support from my family.

I would never be able to fully express my gratitude to Prof. S. Gu and Dr. K. Papadikis, for their guidance, encouragement, financial support. Dr. K. Papadikis is a great problem solver. He supported many good suggestions on my research.

I would like to thank the department of civil engineering at Xi'an Jiaotong-University and the department of Engineering at University of Liverpool for financial, academic and providing me with first class computational resources for the implementation of the current project.

I would also like to thank my friends Mr. Kiron Kumar, Mr. Lei Sun, Mr. Zhenhuan Li, Miss Yina Liu and Miss Lu Zong. They provide me very important encouragement during my graduate study.

Last but not least, I would like to express my profound gratitude from my deepest heart to Miss Jin Zheng, my parents for their love and support through the years of my PhD life.

Nomenclature

Latin letters

Symbol	Description
A	area
a	attraction parameter
B_0	Bond number
b	repulsion parameter
C	contour length
c	ratio of lattice spacing and time step
c_s	lattice sound speed
Ca	capillary number
$D^\star$	dimensionless spread factor
$D^\star_{max}$	maximum dimensionless spread factor
D_0	diameter of the spherical drop prior to impact
D_{max}	maximum diameter of the contact area of the drop on the substrate
$D^\star_{max}$	maximum spreading factor
$\boldsymbol{F}_\alpha$	forcing term
$\boldsymbol{e}_\alpha$	particle velocity in the αth direction
$\boldsymbol{F}_{adhesion}$	fluid-solid adhesion force
$\boldsymbol{F}_{body}$	body force
$\boldsymbol{F}_{cohesion}$	fluid-fluid cohesion force
$\boldsymbol{F}_{total}$	total force on each particle
f_α	particle distribution function along the αth direction
f^{eq}_α	equilibrium distribution function
$G(\boldsymbol{x}, \boldsymbol{x}')$	Green's function
Ga	Galilei number
$h^\star$	dimensionless film thickness
$\boldsymbol{I}$	identity matrix
j_x	component of the moment in x direction
j_y	component of the moment in y direction
j_z	component of the moment in z direction
k	relative permeability

L	contour length to square area ratio
M	viscosity ratio between nonwetting phase and wetting phase
$\boldsymbol{M}$	transformation matrix
$\boldsymbol{m}$	moment space of the density distribution function
$\boldsymbol{m}^{eq}$	moment space of the equilibrium density distribution function
nw	non-wetting phase
Oh	Ohnesorge number
p	pressure
P_c	critical pressure
∇p_i	pressure gradient of fluid i
q	intensity of the germs
r	radius of thee droplet
Re	Reynolds number
$\mathbb{R}^d$	random set of d dimension
S	forcing term in multi-relaxation-time lattice Boltzmann model
S_i	phase saturation of phase i
$\bar{\boldsymbol{S}}$	forcing term in the moment space
$t^\star$	dimensionless evolution time for droplet spreading on surface
δt	time step
T	temperature
T_c	critical temperature
U_0	drop impaction speed
$\boldsymbol{u}^{eq}$	equilibrium value of the velocity
$\boldsymbol{v}$	velocity
$\boldsymbol{v}'$	modified velocity in new forcing term
$\boldsymbol{v}_i$	superficial velocity of fluid i
$V_\nu(Z)$	morphological measures of the individual grains
w	wetting phase
w_α	weighting factor
We	Weber number
$\boldsymbol{x}'$	neighbor site
Z_i	random object

Greek letters

Symbol	Description
ϵ	constant in modified velocity
θ	contact angle
θ_{eq}	equilibrium contact angle

κ	intrinsic permeability of the porous media
$\kappa_{r,i}$	relative permeability of phase i
$\mathbf{\Lambda}$	diagonal matrix of multi-relaxation time lattice Boltzmann model
μ_i	dynamic viscosity of fluid i
μ_L	liquid viscosity
ν	kinetic viscosity
Ξ_i	compact convex set
ρ_L	liquid density
τ	single relaxation time
σ	surface tension of the interface between liquid and gas
ϕ	phase fraction
χ	Euler characteristic
$\bar{\chi}$	mean value of the Euler characteristic
$\bar{\chi}_0$	mean Euler characteristic, neglecting the cavities inside solid clusters
ψ	effective mass
$\mathbf{\Omega}$	begingroup collision matrix
ω	acentric factor

Abbreviations

BGK	Bhatnagar-Gross-Krook
CF-VOF	color function volume-of-fluid
C-LS	conservative level set
D2Q9	two dimension with nine speed directions
D3Q15	three dimension with fifteen speed directions
D3Q19	three dimension with nineteen speed directions
D3Q27	three dimension with twenty seven speed directions
DPD	dissipative particle dynamics
EDM	exact difference method
EOS	equation of state
FCT	flux-corrected transport
LBM	lattice Boltzmann Method
LGA	lattice gas automata
MD	Molecular Dynamics
MRT	lattice-Boltzmann model
PEM	Proton exchange membrane
P-R	Peng-Robinson
SRT	Single relaxation time
STOMP	Subsurface transport over multiple phases
TCAT	thermodynamically constrined averaging theory
VOF	Volume of fluid

Chapter 1

Introduction

A brief introduction on the system of multiphase flow and the development of the lattice Boltzmann model are included into this chapter. Then, the thesis subject and elements of novelty are explained. Finally, the outline of the thesis describes the main contents of each chapter.

1.1 Multiphase flows

In fluid mechanics, the term multi-phase flow is used to refer to any fluid flow consisting of more than one phase or component. Multi-phase flows do not only occur in the natural environment such as rainy or snowy winds, tornadoes, typhoons, air and water pollution etc., but also in a variety of conventional and nuclear power plants, combustion engines, flows inside the human body, oil and gas production and transport, chemical industry etc. Multi-phase flow regimes can be grouped into four categories: gas-liquid or liquid-liquid flows; gas-solid flows; liquid-solid flows; and three-phase flows.

1.1.1 Droplet impingement on surfaces

The droplet impingement on surfaces is an every day occurrence. Interactions between drops and surfaces are a key element of a wide variety of phenomena encountered in nature and engineering applications, such as rain drops falling on the ground, ink-jet printing, spay cooling of hot surfaces (turbine blades, lasers, semiconductor chips), quenching of aluminum alloys and steel, internal combustion engines (intake ducts of gasoline engines or piston bowls in direct-injection diesel engines), spray painting and coating, plasma spraying, and crop spraying. Microfabrication of structured materials, solder bumps on printed circuit boards, and electric circuits in microelectronics produced by precision solder-drop dispensing, as well as liquid atomization and cleaning, catalytic processing in fixed bed reactors and more recently in microfabrication and microchannels [1]. Due to the various applications of droplet impingement on surfaces in micro/nano-fluidic systems and its occurrence in a wide range of nature and engineering, behavior of droplet impact on solid surface has been studied for more than a

century and remains both fundamentally and practically of interest.

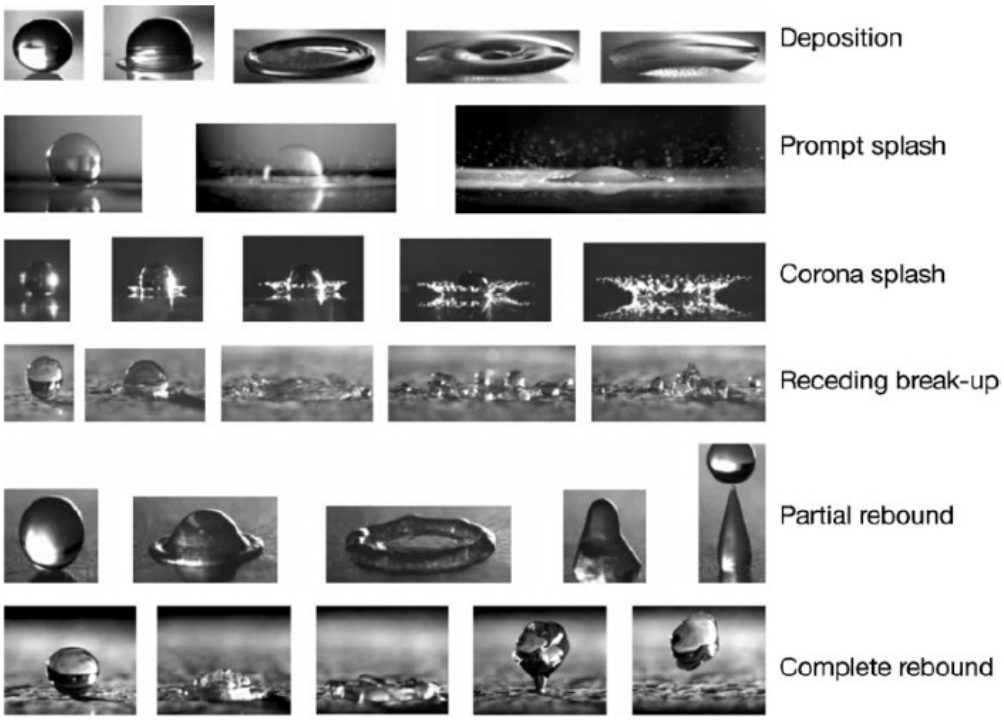

Figure 1.1: Six different outcomes of drop impact on a dry surface [2].

The time evolution of the spreading phase after impact can be divided into three main phases. In the first phase, an internal shock wave propagates at the very beginning of the impact. Then, a spreading lamella is generated in the second phase. During the last phase, the drop deforms in a pancake shape. The impingement outcomes are dependent on several material properties and dynamic parameters [2]. Several outcomes may occur as a result of droplet impact on a rigid dry surface, it may be broadly classified as deposition, splashing and rebounding. Six possible outcomes were observed by recent experimental study as shown in Fig. 1.1, namely deposition, prompt splash, corona splash, receding break-up, partial rebound and complete rebound [2]. The splashing of droplet and secondary drops formation are obviously undesirable in applications such as ink-jet printing and spray coating, while splashing may be desirable in combustion chambers. Thus, a fundamental understanding of the dynamic behavour of droplet impact onto solid surfaces and predicting its subsequent outcome are very important to engineering applications.

1.1.2 Two-phase immiscible flows in porous media

Fluid flow in a porous medium is a common phenomenon in nature, and in many fields of science and engineering. The understanding of immiscible two-phase flows in porous media is of critical importance in industrial operations such as, enhanced oil recovery, geologic CO_2 sequestration, groundwater supply and remediation, proton exchange membrane (PEM) fuel cells, catalytic processing in fixed bed reactors etc. The importance of improving the understanding of such industrial processes arises from the high amount of energy consumed by them. For example, a typical problem that should be faced in oil recovery is the amount of unrecovered oil left in oil reservoirs by traditional recovery techniques. A detailed understanding of the coupling of transport phenomena and chemical reaction in porous media is important for the process in catalytic reactors. However, in many cases the porous structure of the medium and the fluid interactions are very complex. Due to the complexity of such systems, flow in such porous media is usually investigated on a macroscopic scale, such as Darcy's law. The correlations between material characteristics, such as porosity and specific surface area and flow properties were firstly discovered by Darcy [3]. Permeability is given by the coefficient of linear response of the fluid to a non-zero pressure gradient in terms of the flux induced. Then, conventional macro-scale multi-phase flow models in porous media rely heavily on extensions of Darcy's law, where each phase moves through its own channel which is bounded only by the solid walls. The viscous coupling between the two phases is ignored in this kind of approach. Under the assumptions described above the relative permeability is taken to be only a function of the phase saturation S_i [4]. The existence of the viscous coupling effect, which represents the momentum transfer between the two phases, makes this simple extension of Darcy's law highly questionable. Several theoretical, experimental and numerical studies have revealed that two-phase transport in porous media depends strongly on the interfacial morphology and fluid dynamics near the interface. Hence the relative permeability for every phase does not only depend on S_i, but it is also a function of the pore geometry properties, capillary number Ca, wetting angle, viscosity ratio $M = \mu_{nw}/\mu_w$ and flow process (imbibition or drainage). In addtion, several experimental and numerical methods investigate the flow in porous media on micro-scale, commonly focus on the effective parameters constitutive relationships. Different numerical approaches have been used to solve multiphase flow in porous media at the pore scale, involving pore-network models, Lattice-Boltzmann models, Lagrangian mesh-free methods and grid-based computational fluid dynamics with fluid-fluid interface tracking and velocity-dependent contact angles. Microscopic models provide not only an insight into the pore-scale dynamics, but also the effective parameters for macroscopic models. Thus, a proper understanding of the immiscible two-phase flows on the micro-scale can help improving the prediction of flow behavior on the macro-scale and it extremely important for applied fields.

1.2 Numerical techniques for multiphase flows

Currently, numerical solutions to the fluid flow problem can be divided into three scales including macroscale, mesoscale and microscale. In macroscale solution, the governing equations are identified into an finite control volume. Then, the domain is discretized into volume, grids, or elements depending on the method of solution. The velocity, pressure and temperature of every point in space are stored in every node or averaged over a finite volume. The continuum approach is more suitable to treat the macroscopic phenomenon, while such an approach has difficulties to incorporate the microscopic interactions, which are crucial in many microfluidic circumstances [5]. In microscopic scale, the medium can be considered to be made of atoms or molecules which collide with each other. The micro-scale calculations for such systems are based on the Molecular Dynamics (MD) simulations. The fluid behaviours (trajectory and velocity) are decided by the evolution of individual molecules interaction with each other through intermolecular potentials. Temperature and pressure are related to the kinetic energy of the particles (mass and velocity) and frequency of particles bombardment on the boundaries [6]. Molecular Dynamics simulations can handle microscopic molecular structures and interactions without introducing extra ingredients. However, the huge computation demand limits its applications to a relatively large system. For example, the work is limited to simulation on the 3 5 nm and 5 μs in the microsecond simulations of spontaneous methane hydrate nucleation and growth [7]. In the molecular dynamics simulations on flattening process with high temperature and high speed droplet, 200 h is required for a simulation in a period of 60 ps in a $40nm \times 40nm \times 2nm$ domain with Pentium IV 3 GHz CPU and 1GB memory [8]. Sometimes, it is not important to know the behavior of each molecule or atom, it is necessary to know the function that can represent the behavior of many particles. Therefore, there exist several mesoscopic methods between the macroscopic and microscopic approaches, such as the dissipative particle dynamics (DPD) [9] and the lattice Boltzmann method (LBM). DPD is a mesh-free particle-based method for fluids and other soft matters and can be considered as a coarse-grained version of MD. The LBM utilizes the probability distribution function to find a particle at a certain time and at a certain location. Therefore, the method avoids tracking a separate molecule, but a whole ensemble of molecules, resulting in the probability distribution function.

1.3 Lattice Boltzmann model

The lattice Boltzmann Method (LBM), as one of the mesoscopic methods, is the bridge between micro-scale and macro-scale. The lattice Boltzmann method is a kinetic theory-based numerical technique for solving transport problems. Unlike particle-based methods such as Molecular Dynamics or Direct Simulation Monte Carlo, LBM does not

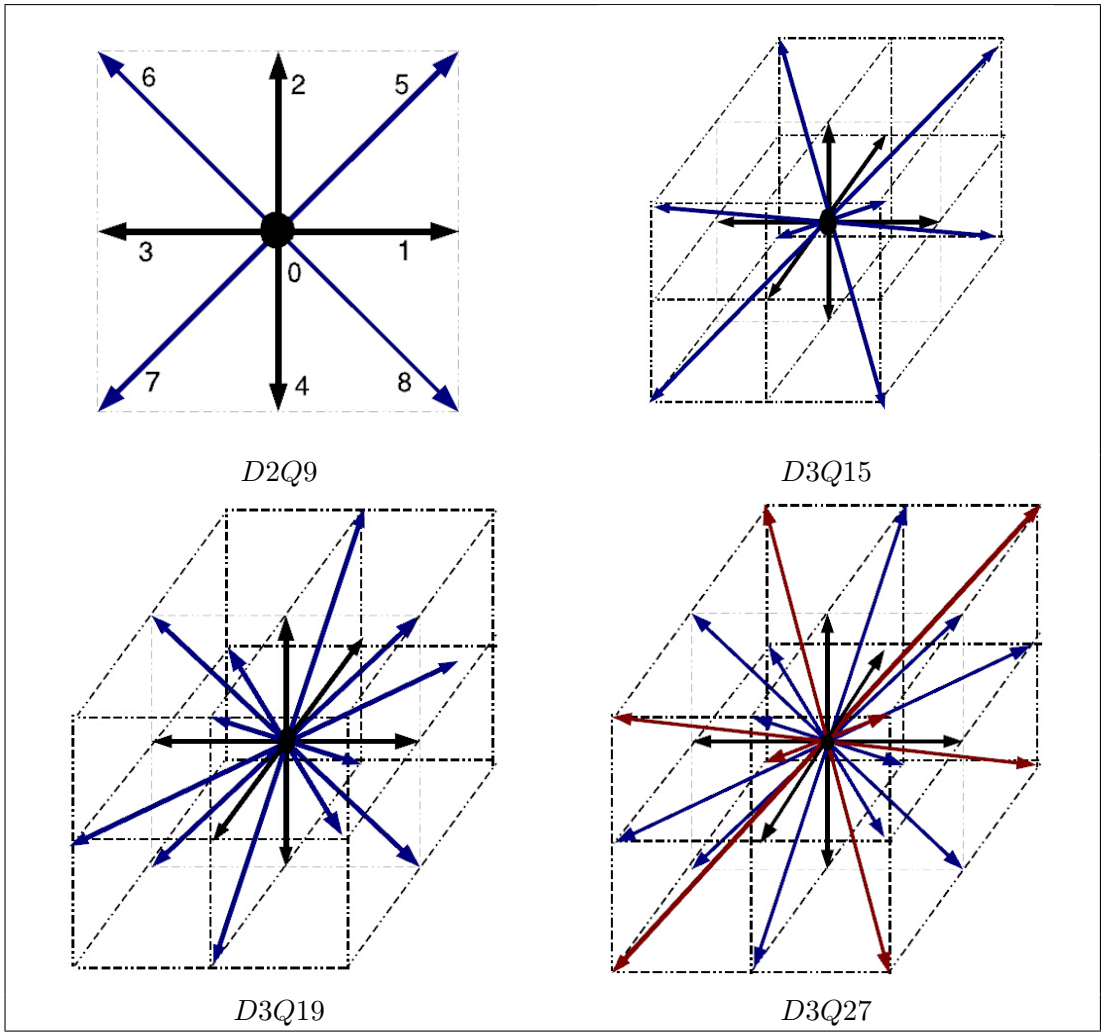

Figure 1.2: Different lattice models for two- and three-dimensional simulations [8].

consider each particle behaviour alone but behavior of a collection of particles as a unit and the property of the collection of particles is represented by a distribution function. Lattice Boltzmann model consists of two steps. The first one is a local step describing the distribution of particle density due to the collisions at each grid node. The second step, so called streaming step, is responsible for streaming of particles from the current lattice nodes to the nearest nodes. A lattice model is uniquely identified by the number of dimensions D and by the number of speeds Q. Currently, the most employed model for two dimensional simulations is the D2Q9, while for three dimensional ones, models with D3Q15, D3Q19 and D3Q27 [10] are available as shown in Fig. 1.2. There are many native advantages for the lattice Boltzmann model. It is easy to apply for complex domains (flows in porous media), easy to handle complex flows such as multi-phase and multi-component flows without needing to trace the interfaces between different phases. In addition, it can be adapted to parallel processesing computing.

The use of lattice Boltzmann method has been growing continuously in the last 30 years. Historically, LBM originated based on the lattice gas automata (LGA), which can be seen as a simplified, fictitious version of Molecular Dynamics model [11]. In these methods the fluid is considered by particles that move on a regular lattice which often must be chosen in a special way. Lattice gas automata suffers from several native defects including the lack of Galilean invariance, presence of statistical noise and exponential complexity for three-dimensional lattices [12]. In order to overcome the deficiencies of lattice-gas methods and improve the situation, several lattice-Boltzmann models were formulated. The statistical noise of LGA can be removed by replacing the Boolean particle number with density distribution function. The first LBM is named as nonlinear lattice-Boltzmann model [13] in which a mean-value representation of particles eliminated the problem of statistical noise. Then, a linearized enhanced-collision method was developed to overcome the complexity of the lattice-gas collision operator used also in the lattice-Boltzmann models [14]. Furthermore, the inclusion of rest particles and Maxwellian velocity distribution achieved the Galilean invariant macroscopic behaviour [15]. The appearance of the lattice Bhatnagar-Gross-Krook (BGK) model make the LBM reach maturity and be widely used in industrial and academic works. In the lattice BGK, the collision operator is based on the single-relaxation-time approximation to the local equilibrium distribution [16]. In addition, the numerical stability of LBM, especially in the high-Reynolds number simulations was increased by the multi-relaxation time lattice-Boltzmann model (MRT).

1.4 Thesis subject

The subject of the current thesis is to numerically study the dynamics of droplet impingement onto the solid phase and understanding the spreading process, as well as the immiscible two-phase flows in porous media. The numerical investigation will be performed by using a high density ratio multi-phase lattice Boltzmann model which is capable of simulating multi-phase flows in complex systems. The lattice Boltzmann model is able to capture interfacial information without tracking or constructing the vapour-liquid interface. The Boolean model is applied to generate the artificial porous media. The MATLAB language has been used as the computational platform for the LB code development.

The main task of the current thesis is to get new significant insight on the physical phenomena that govern the process of droplet impact onto solid surfaces, as well as the fluid flow in porous media by using advanced lattice-Boltzmann methods in combination with numerical reconstructions of porous media. The ambition is to understand in particular the dynamic behaviour of droplet impingement onto solid surfaces and to identify the effects of the non-dimensional parameters (i.e. Re, We, Oh) on the various stages of the process. In addition, the different flow mechanisms that corre-

spond to different flow regimes for two phases flows in porous media is investigated. Finally, the impact of the geometrical properties of the porous media on the wetting and non-wetting phase relative permeabilities is analyzed.

1.5 Elements of novelty

Several theoretical, experimental and numerical studies have been presented in the literature to understand the process of droplet impingement onto solid phase. As a modern method, lattice Boltzmann method (LBM) has attracted considerable attention in simulating the droplet impingement on solid surfaces. Most of the LBM studies on the droplet impingement onto solid surfaces are limited to low density ratio between two phases and instability with a relaxation time τ less than 1. In current thesis, a 3-dimensional lattice Boltzmann model is applied on the study of the impaction of a liquid droplet on a dry flat surface for a liquid-gas system with large density ratio. The simulations support the information about the influence of Reynolds number, Weber number, Ohnesorge number and the target-to-drop size ratio on the impingement process. Then, the impaction of liquid droplet on a curved surface for the liquid-gas system with large density ratio and low kinematic viscosity of the fluid is simulated by a two-dimensional multi-relaxation-time interaction-potential-based lattice Boltzmann model based on the improved forcing scheme. In addition, an improved force scheme is proposed for the three-dimensional MRT pseudopotential Lattice Boltzmann model which is based on the improved force scheme for the Single relaxation time (SRT) pseudopotential lattice Boltzmann model and the Chapman-Enskog analysis.
Experimental works and computational approaches have also revealed that two-phase transport in porous media depends strongly on the interfacial morphology and fluid dynamics near the interface. The previous numerical works on the relative permeability of multi-phase flow in porous media are focus on the relationship between relative permeability and capillary number, wetting angle, viscosity ratio. However, to the best of our knowledge, there are no systematic LB numerical studies presented in the literature that address the relationship between the geometrical properties and the relative permeabilities for immiscible two-phase flows in pore-scale porous media. In the current work, a two-dimensional high density ratio MRT lattice Boltzmann model as a robust numerical method is used to study the immiscible two-phase flow in porous media. The various flow mechanisms with different flow regimes and the dependence of relative permeability for two phases on the geometrical properties of porous media are reported. The porous media structures with different geometrical properties are artificially generated by a Boolean model based on a random distribution of overlapping ellipses/circles.

1.6 Progress of research

The research started with the reviewing of the literature on numerical modeling works on the multi-phase flow in porous media, as well as the different lattice Boltzmann models for multi-phase flows. It was found that lattice Boltzmann model is a robust numerical model in simulating multiphase flow in complex porous systems caused by its native advantages. Generally, the porous media is generated by packing union set of grains with different shapes. Our simulation work began from studying the process of droplet impingement onto flat surface and single spherical grain.

The following step was the code development after the basic idea of the project was formed. Firstly, the code was developed for a 3-dimensional lattice Boltzmann model based on the original Shan-Chen model and the improvements in the single-component multiphase flow model reported by Yuan and Schaefer [17]. The impaction of a liquid droplet on a dry flat surface and a curved surface for a liquid-gas system with large density ratio was studied. In order to overcome the limitations of instability with a relaxation time τ less tan 1, another MATLAB code was developed on the base of a two-dimensional multi-relaxation-time interaction-potential-based lattice Botlzmann model to study specifically the dynamic behavior of liquid droplet on a curved surface for the liquid-gas system with large density ratio and low kinematic viscosity of the liquid phase. Then, a three-dimensional multi-relaxation time lattice Boltzmann model with an improved forcing scheme which can tolerate high density ratios and low viscosity is proposed to extend the application of the multiphase lattice Boltzmann model. At last, the developed code was applied to study the immiscible two-phase flow in porous media, such as the flow mechanisms with different flow regimes, the impact of the geometrical properties (volume fraction, solid phase contour length, solid phase connectivity) of the porous media on the relative permeability. Due to the limitation of computational capacity, the study on multiphase flow in porous media was conducted in two dimensions.

1.7 Outline of the thesis

The thesis is organized in six main chapters.

The first chapter provides a brief introduction on the background and the history of development of lattice Boltzmann model, as well as multiphase systems involving the processes of droplet impingement on surface and two-phase immiscible flows in porous media. The main research subject is illustrated, the different processes and physical phenomena occurring in droplet impingement onto solid surfaces and immiscible two-phase flows in porous media are explained. The elements of novelty and the significance of the current research are also described. The chapter finishes with the discussion on the progress of the research during the PhD time and the description of the outline of

the current thesis.

In the second chapter, the various computational models in the range of scientific community for multiphase flows are reviewed. Specifically, the lattice Boltzmann modeling for multiphase flow is reviewed in this chapter. The review continues with the description of the previously published research work on the droplet impingement onto solid surfaces, involving the experimental and numerical studies. The existing theoretical, experimental and numerical studies on the interfacial coupling effect in the two-phase flow in porous media are reviewed at the end of the second chapter.

The third chapter provides the detailed information of the lattice Boltzmann model which was used as a numerical method in the current work. It starts with the description of the Shan-Chen multiphase model with Peng-Robinson equation of state, the method of incorporation of the fluid-fluid cohesion force, fluid-solid adhesion force as well as the body force into the pseudo-potential model. The chapter continues with the description of the 2-dimensional multi-relaxation time pseudopotential model which can tolerate high density ratios and low viscosity. The forcing schemes for the single relaxation time and multi relaxation time models are also provided in this section. Finally, an improved force scheme is proposed for the three-dimensional MRT pseudopotential lattice Boltzmann model.

The main content of the fourth chapter is the investigation of the liquid droplet impact process on solid surface by using the SRT Shan-Chen multiphase model and the MRT pseudopotential LBM with improved force scheme. The dynamic behaviours of the spreading process of the liquid droplet on the flat surface and the impaction of the liquid droplet on a curved surface are reported, followed by their dependence on the Reynolds number, Weber number, Galilei number and surface characteristics.

The fifth chapter gives an insight on the flow mechanisms of the immiscible two-phase flows in artificial porous media, as well as the effect of volume fraction, solid phase contour length and connectivity on the wetting and non-wetting phase relative permeabilities. The pore size distribution for the artificial porous structures with various Minkowski functionals is computed by a independent code developed in MATLAB. The problem of how each different single Minkowski functional affects the relative permeabilities for both phases at various saturations of the non-wetting phase is addressed.

The sixth chapter of the thesis presents a general discussion and draws important conclusion from this research. Also recommendations for the future work are given at the end of the thesis.

The six main chapters of the thesis are followed by three appendices.

Appendix A provides the derivation process of the three dimensional macroscopic equations recovered from the improved forcing scheme.

Appendix B presents the flow chart and code for the generation of artificial porous media with specific Minkowski functionals.

Appendix C presents the flow chart and code to explain the measure of pore size distribution in artificial porous media.

Chapter 2

Literature review

This chapter provides the review of the previous studies in the fields of numerical modelling for multiphase flows with a special focus on lattice Boltzmann models. Also, previous investigations including the theoretical, experimental and numerical studies on the droplet impingement on solid surfaces and immiscible two-phase flow in porous media are presented.

2.1 Continuum models for multiphase flows

Multiphase flows occur in many natural and industrial processes. However, the simulation of multiphase flows is a challenging task in the realm of computational fluid dynamics due to the inherent complexity of the phenomena involved. The phases are separated by an interface in gas-liquid and immiscible liquid-liquid flow. It is impossible to simulate the macroscopic two-fluid flows in chemical engineering with full 3D time-dependent interface resolving numerical modeling over sufficiently long time. So, the detail of the interface are not resolved when simulation methods are used for such problems. The Euler-Euler approach [18, 19] and Euler-Lagrange [20] method are widely used methods for computation of macroscopic two-phase flows. In the Euler-Euler approach, a set of momentum and continuity equations is solved for each phase. Coupling is achieved through the pressure and interphase exchange coefficients. The Euler-Lagrange method is based on the point particle approach where the flow around individual disperse elements of presumed shape is not resolved by the grid. The interfacial transfer of momentum, heat and mass between the two immiscible phases are relied on physical models derived from theoretical or experimental results for both two methods.

In micro-scale, the importance of details of interface such as breakup or coalescence appears and the physical models obtained for isolated fluid particles cannot be used. For this reason, the Euler-Euler and Euler-Lagrange method do not play a significant role for computation of two-fluid flows in micro-scale. In order to capture the information of the interface between two immiscible phases, immiscible multiphase flows are

simulated by solving the macroscopic Navier-Stokes equations coupled with an appropriate technique to track the interface between different phases. Interface tracking can be commonly classified into two categories: sharp interface methods [21,22] and diffuse interface methods [23,24]. In the sharp interface method, different fluids are separated by the sharp interface and fluid properties such as density and viscosity at the interface are discontinuous, while the interface has a non-zero width and fluid properties vary smoothly across the interface in the finite thickness method.

The sharp interface methods can be divided into two main groups depending on the type of the mesh. The first group named as moving-mesh methods, such methods are often based on the arbitrary Lagrangian-Eulerian formulation, where the interface is resolved by moving mesh [25–28]. In order to maintain good mesh quality thereby capture the changing curvature and obtain computational efficiency, the local mesh adaptations involving mesh coarsening and mesh refining need to be performed for both the interior and the interface elements. However, complex algorithms are required to handle the topological deformation of interface such as coalescence, break up and pinch-off [29]. In the second group of methods such as volume of fluid [30], level set [31,32] and front tracking [33] in which the fixed grid is used for solving the Navier-Stokes equations and the interface is represented and located by different data structures of functions. These methods can be divided into two classes. In front-capturing methods including the interface reconstruction Volume of fluid (VOF) method and level-set method, the interface is implicitly embedded in a scalar field function defined on a fixed Eulerian mesh, such as a Cartesian grid, while the interface is explicitly represented by Lagrangian particles and its dynamics is tracked by the motion of these particles in the second category that is front-tracking method.

Three methods are classified into methods with diffuse interface method. It should be noted that the finite thickness arises from numerical reasons in the colour function VOF method and the conservative level set method, whereas the finite thickness stems from physical modeling in the phase-field method. The color function volume-of-fluid (CF-VOF) method rely on a colour function which can be considered as an approximation for the volume fraction function. Compared with the interface reconstruction VOF method, the process of complex interface reconstruction is avoided. The color function is solved by difference schemes. Hirt and Nichols [34] and Rudman [35] proposed the scheme which is based on the multidimensional flux-corrected transport (FCT) algorithm of Zalesak [36]. Bonometti and Magnaudet [37] also adopted the FCT scheme to solve the colour-function equation in non-conservative form by three successive one-dimensional steps. Another CF-VOF method is the high resolution interface capturing scheme, which uses a nonlinear blend of upwind and downwind cell-face values. The conservative level set (C-LS) method is developed by Olsson and Kreiss [38], combines elements from the CF-VOF and level set method. A modification of the reinitialization

step was formulated in the follow-up study [39]. Because of the advantage in capturing interfaces implicitly, the diffuse interface method has gained considerable attention in recent years. In this method, the sharp interfaces is replaced by thin but nonzero thickness transition regions in which the interfacial forces are smoothly distributed [40]. The basic idea of diffuse interface method is to introduce an order parameter that varies continuously over thin interfacial layers and is mostly uniform in the bulk phases. The temporal evolution of the order parameter is governed by the Cahn-Hilliard equation.

2.2 Lattice Boltzmann modelling for multiphase flows

In recent years, the lattice-Boltzmann method (LBM) has attracted much attention as an alternative way of simulating multiphase fluid flow problems [41]. Unlike conventional computational fluid dynamics methods, which are based on the discretization of macroscopic governing equations, the lattice Boltzmann model method is based on microscopic models and mesoscopic kinetic equations in which the collective behavior of the particle distribution function is used to simulate the continuum mechanics of the system [17]. Also, for multiphase flows, the interface between different phases is automatically maintained, hence its reconstruction or tracking is avoided [42].
There are several models developed for multicomponent flows during the last twenty years. They are the Rothman and Keller's colour method [43, 44], Shan and Chen's potential method [45], Swift et al.'s free energy method [46], He et al.'s phase field method [47] and field mediator LB model which was proposed by Santos et al. [48].
The first multiphase LB model is the colour-gradient model proposed by Gunstensen et al. [44] based on a lattice gas method [43]. In this model, the different phases or components were labeled by different colours and the interparticle interactions are expressed by a local colour gradient associated with the density difference. The original RK model was modified by Grunau et al. [49] to allow the simulation of variable density and viscosity between two phases. However, the density ratio is restricted to around one and the perturbation step can cause an anisotropic interfacial tension that induces high spurious velocities near an interface [41]. Then, some improvements have been made to model the interfacial tension and reduce the spurious velocities at the interface based on the original RK colour model proposed by Gunstensen et al. [44]. The concept of a continuum surface force was used by Lishchuk et al. [50] to model the interfacial tension. It has been reported that the spurious currents can be greatly reduced and the isotropy of the interface can be improved. However, only equal density is considered for both fluids in this model. Latva-Kokko and Rothman [51] found that the non-physical behavior such as anisotropy and high spurious velocities at the interface are caused by the original recoloring step performed at the interface of the fluids. A new recoloring operators was proposed by [51] to reduce the non-physical behavior near the interface. Reis and Phillips [52] developed a two-dimensional nine-velocity LB model

for immiscible binary fluids with variable viscosities and density ratios. The perturbation operator was modified so that the model complies with the capillary stress tensor within the macroscopic limit. Liu et al. [53] further extend the two-dimensional nine-velocity LB model to three-dimensional. Leclaire et al. [54] combined the recoloring operator of Latva-Kokko and Rothman [51] with the model of Reis and Phillips [52], the maximal stable density ratios were increased for some basic test cases following this modification. In addition, it was found that the multiple relaxation time (MRT) collision operator can greatly improves the overall stability of the RK model for high density and viscosity ratios [55].

Shan and Chen [45] proposed another type of multiphase LB model named as the pseudopotential model in which an artificial interparticle potential was employed to describe fluid interactions. It is well known that the original formulation of the Shan-Chen model is limited to stability for low liquid to gas phase density ratios, and over a small range of viscosities. Shan [56] realized that the discretization of the forcing term had insufficient isotropy, thus increasing the order of the finite difference calculation which resulted in a decrease in spurious velocities near the interface. On the basis of this method, Sbragaglia et al. [57] developed an extended pseudopotential method which permits to tune the equation of state and surface tension independently of each other. The spurious velocity contributions of this extended model are shown to vanish in the limit of high grid refinement and high order isotropy. Yuan and Schaefer [17] expressed that the equation of state (EOS) plays an important role in achieving high-density ratios. The form of the effective number density was changed in order to reproduce a more realistic equation of state which result in the attainable density ratio from tens to thousands. Guo et al. [58] analysed the effects of the discrete lattice on the inclusion of the force term and proposed a scheme which resolve the effect. Furthermore, Kupershtokh [59] introduced the exact difference method (EDM). Li et al. [60] proposed an improved pseudopotential model which can achieve thermodynamic consistency and treat high density ratio multiphase flows. In order to overcome the restriction of numerical instabilities at low viscosities, the models which simulate high-density ratio flows are extended to lower viscosities by employing multiple-relaxation-times [61–63].

Swift et al. [46] proposed the third type of multiphase LB model with the idea of free energy. In this model, the interface behavior such as Cahn-Hilliard or Ginzbourg-Landau were introduced by means of a free energy. The main feature of this model is the direct inclusion of a nonideal pressure tensor and an external chemical potential instead of the introduction of the additional collision operator. However, the shortcoming of the original model is the lack of Galilean invariance that was restored in the later developed free-energy models [64, 65]. To overcome this difficulty of the numerical instabilities due to the high density ratio between two phases, Inamuro et al. [66] proposed a model, based on the free energy method for multiphase flows with large

density ratio. However, Inamuro et al. [66] involves the solution of a Poisson equation, which decreased the simplicity of the usual LBM. Yan and Zu [67] reported a new numerical scheme for the lattice Boltzmann method which combines the existing models of Inamuro et al. [66] and Briant et al. [68] for calculating the liquid droplet behavior on a partially wetted surface typical for gas-liquid systems with large density ratio. He et al. [47] developed a new multiphase LB model with the extension and improvement of their former kinetic-theory-based model [69]. Two distribution functions were employed, one of which calculates the velocity and pressure fields and another evaluates the index function to track the interfaces between different fluids. As pressure is smooth in the whole flow field, the high variation of particle distribution function is avoided. Based on the LB model of He et al. [47], Lee and Lin [70] developed a stabilized scheme for the discrete Boltzmann equation for multiphase flows with large density ratio. A stable discretization scheme and a second-order mixed difference scheme were proposed to calculated the forcing terms so that a large density ratio can be reached. The LBE method [70] was applied to microscale drop impact on dry surfaces. Recently, the lattice Boltzmann method [71] for immiscible multiphase flows with large density ratio is extended to high Reynolds number flows using a multiple-relaxation-time(MRT) collision operator. Zheng et al. [72, 73] found that the interface capturing equation in all of the above-mentioned multiphase models cannot completely recover the convective Cahn-Hilliard equation. To solve this problem, the interface is naturally captured by minimizing the free energy functional [72] which can recover the Cahn-Hilliard equation exactly. Combing this lattice Boltzmann equation for tracing the interface and a free-energy lattice Boltzmann equation for solving the velocity field, a lattice Boltzmann model for multiphase flows was developed by Zheng et al. [73]. However, Fakhari and Rahimian [74] found that the LB model of [73] is not capable of dealing with two-phase flows with different densities and is mostly suitable for a density-matched binary fluid. Since the particle distribution function is directly used to measure the mean density, the effect of local density variation cannot be properly considered in the momentum equation when the multiphase flow with density contrast is solved. Fakhari and Rahimian proposed a multi-relaxation-time LB model which is able to simulate multiphase flows with moderate density ratios and being consistent with the Cahn-Hilliard equation by combining the lattice Boltzmann equation of Zheng et al. [72] for interface capturing with the lattice Boltzmann equation of He et al. [47] for the velocity and pressure fields. To remove the drawback of the original LB model proposed by Zheng et al. [73], a transformation which is similar to the one used in the Lee-Lin model [71] is introduced in the original Zheng et al.'s model to change the particle distribution function for the local density and momentum into that for the mean density and momentum [75]. Recently, a new lattice Boltzmann model [76] is proposed based on the phase-field theory to simulate incompressible binary fluids with density

and viscosity contrasts. The model utilized two lattice Boltzmann equations which one for the interface capturing and the another for resolving hydrodynamic properties. The lattice Boltzmann equation for interface capturing is based on the basic idea of Zheng et al. [72],the performance is improved by introducing several modifications.New equilibrium particle distribution functions are proposed for hydrodynamic properties, this lattice Boltzmann equation for hydrodynamic properties is capable for recover the divergence-free incompressible Navier-Stokes equations avoiding spurious interfacial forces. Then, a phase-field-based multiple-relaxation-time lattice Boltzmann model is proposed by Liang et al. [77]. Different from the previous work [76], a time-derivative term is incorporated in the interfacial evolution equation which is able to recover the the Cahn-Hilliard equation exactly. In addition, a modified pressure distribution function was introduced that resulted in the correct incompressible hydrodynamic equations and simultaneously the pressure and velocity can be obtained explicitly.
The last multiphase flow LB model is named field mediator LB model, proposed by Santos et al. [48]. The collision term was split into mutual and cross, long-range forces were simulated by using field mediators. They have the advantage of being able to incorporate binary diffusivity and therefore can be adapted to simulate miscible fluids.

2.3 Droplet impingement on solid surfaces

Rein [78] and Yarin [1] presented comprehensive reviews on the experimental and theoretical studies of the droplet impact dynamics onto the solid surface. Systematic studies have been carried out by Rioboo et al [79]. Six possible outcomes of drop impact on a dry surface were revealed, namely deposition, prompt splash, corona splash, receding break-up, partial rebound and complete rebound. To systematically study the dynamics of a spreading droplet, three major non-dimensional parameters are usually employed, specifically the Weber number (We), Reynolds number (Re) and the Ohnesorge number (Oh) which is also directly related to We and Re. They are defined as

$$We = \frac{\rho_L D_0 U_0^2}{\sigma}, \tag{2.1}$$

$$Re = \frac{\rho_L D_0 U_0}{\mu_L}, \tag{2.2}$$

$$Oh = \frac{\mu_L}{\sqrt{D_0 \sigma \rho_L}} = \frac{\sqrt{We}}{Re}, \tag{2.3}$$

where U_0 is the drop impaction speed, D_0 is the diameter of the spherical drop prior to impact, μ_L is the liquid viscosity, σ is surface tension of the interface between liquid and gas, and the ρ_L is liquid density. The spread factor, which is an effect of the impact

process, is defined as the ratio of the total diameter of the spreading droplet (not the lamella diameter) and the initial droplet diameter:

$$D^{\star} = \frac{D}{D_0}. \tag{2.4}$$

Experimental and analytical investigations have been performed to study the time evolution of the spread factor and to determine the correlation between the maximum spreading factor and the Weber, Reynolds and Ohnesorge numbers [80–85]. The maximum spreading factor is defined as $D^{\star}_{max} = D_{max}/D_0$, where D_{max} is the maximum diameter of the contact area of the drop on the substrate. Asai et al. [80] examined the spreading of a micron size droplet from an inkjet printhead impacting on moving paper and obtained a simple correlation formula to predict the maximum spreading ratio. Scheller and Bousfield [81] showed that the contact angle effect on the spreading film diameter is negligible for droplet Re >10, and that the maximum spread factor follows the correlation given by $D_{max} = 0.61(Re^2Oh)^{0.166}$. Roisman et al. [85] modeled the drop impaction process to predict the evolution of the drop diameter. The model accounts for the capillary force, viscosity and inertial effects, as well as the dynamic contact angle. Micron drop impaction on smooth solid substrates was investigated by Dong [86] over a wide range of impaction speeds, surface contact angles and drop diameters as shown in Fig. 2.1. The experimental results were compared with several existing equations for predicting maximum spreading. The prediction equation of Roisman et al. [85] agrees well with the experimental results for both low and high We impactions. The empirical equation of Scheller and Bousfield [81] also gave a good fit even though the effect of the equilibrium contact angle was neglected.

Previously published work [87–89] has shown that the impaction of droplets onto curved surfaces (e. g spheres), differs significantly from the impact of droplets on flat surface. Hung and Yao [87] have carried out experiments on the impaction of water droplets with diameters of 110, 350 and 680 μm on cylindrical wires. The effects of droplet velocity and wire sizes were studied parametrically to reveal the impaction characteristics. Hardalupas et al. [88] have conducted experiments on droplets of a water-ethanol-glycerol solution in the size and velocity ranges of $160 < D < 230$ μm and $6 < U < 13$ m/s respectively, impinging on the surface of a solid sphere with 0.8 - 1.3 mm diameter. The impinged droplet formed a crown which was influenced by surface roughness, droplet kinematic and liquid properties. Bakshi et al. [89] have reported experimental data and theoretical investigations on the impact of a droplet onto a spherical target over a range of Reynolds numbers and target-to-drop size ratios. The snapshots with increasing time are shown in Fig. 2.2. Three distinct temporal phases of the film dynamics were found, namely the initial drop deformation phase, the inertia dominated phase, and the viscosity dominated phase. The influence of the droplet

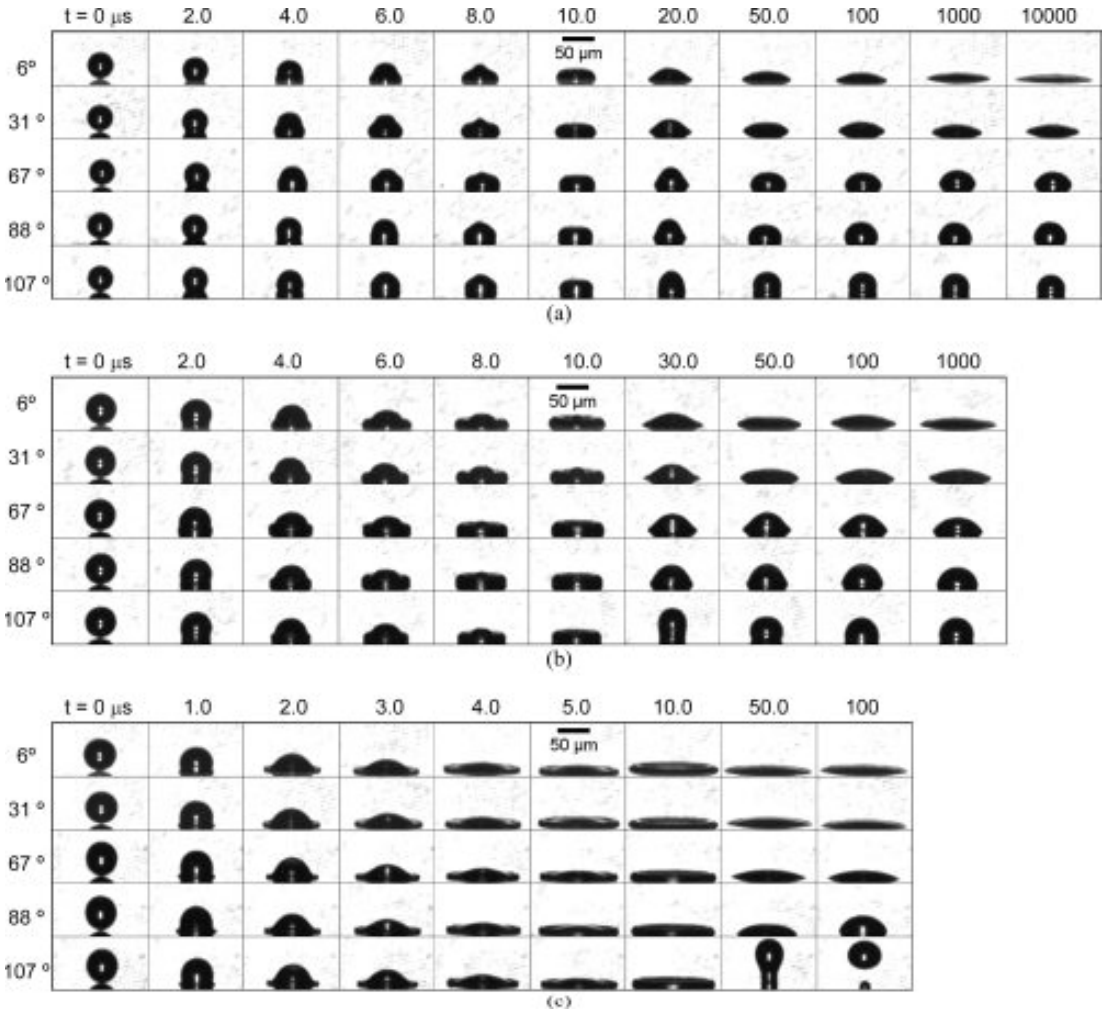

Figure 2.1: Sequence of images for drop impaction on five substrates:(a) $U_0 = 2.21m/s$, $D_0 = 40.9\mu m$; (b) $U_0 = 4.36m/s$,$D_0 = 48.8\mu m$; (c) $U_0 = 12.2m/s$, $D_0 = 50.5\mu m$ [84].

Reynolds number and the target-to-drop size ratio on the dynamics of the film flow on the surface of the target were conducted.

Recently, numerical investigations have drawn increasing attention in simulating the impingement process, because experiments alone are not adequate enough to define the governing physics [90]. Trapaga and Szekely [91] used a commercial code (FLOW-3D) that incorporates the "volume of fluid"(VOF) method to study the impact of molten particles in the thermal spray process. Bussmann et al. [92] studied the dynamics of droplet impact on flat and inclined surfaces with a 3D VOF method. Pasandideh-Fard et al. [93] developed a three-dimensional model which is an extension of finite-difference, fixed-grid Eulerian model to simulated the impact of a $2mm$ diameter water droplet landing with low velocity ($\sim 1m/s$) on tubes ranging in diameter from 0.5 to 6.35 mm. Liu et al. [94] developed a fixed-grid, sharp interface method to simulate the droplet impact and spreading on surfaces of arbitrary shape with a level-set method. Ge and

Figure 2.2: Impact of a droplet onto a spherical target [87].

Fan [95] studied the process of collision between an evaporative droplet and a high-temperature particle in a riser reactor with a three-dimensional level-set method.

As a modern method, lattice Boltzmann method (LBM) has attracted considerable

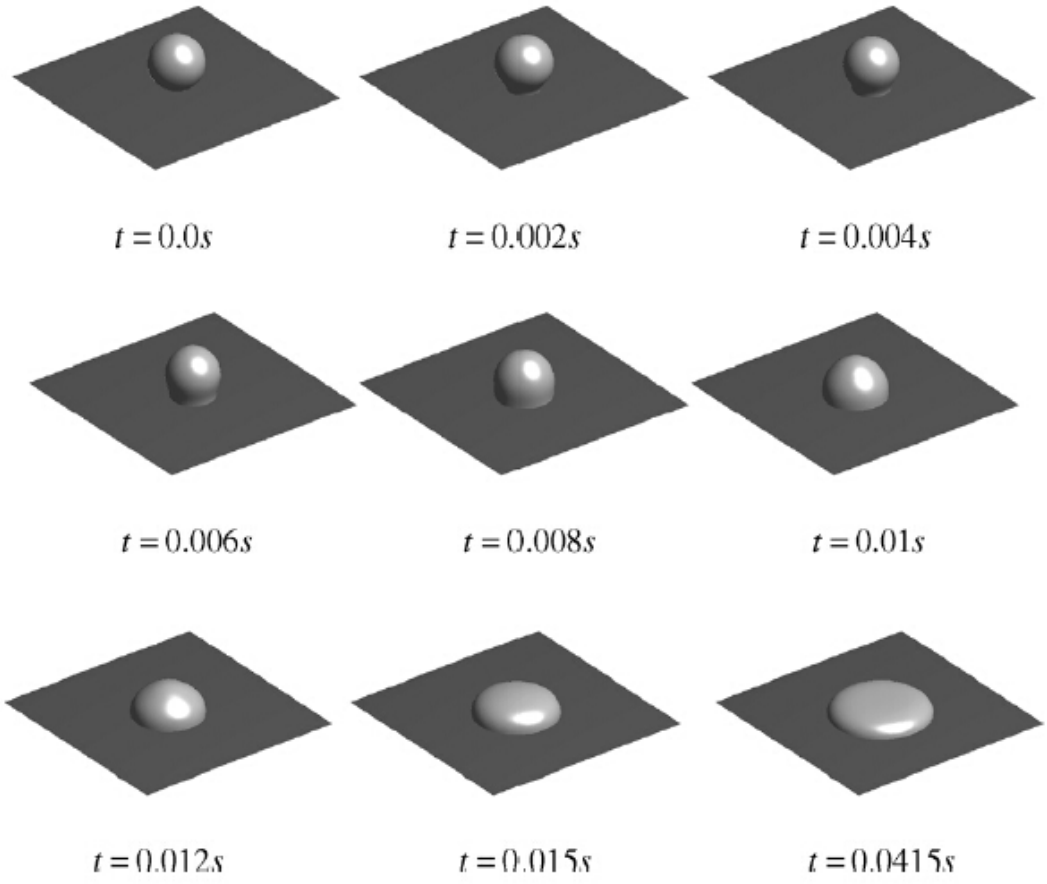

Figure 2.3: Snapshots of droplet spreading on a uniform hydrophilic surface with the density ratio is 775[65].

attention in simulating the droplet impingement on solid surfaces. Gupta and Kumar [96, 97] studied the droplet impingement on a flat solid surface at low density ratios. Yan and Zu [67] reported a new numerical scheme for the lattice Boltzmann method, which combines the existing model of Inamuro et al. [66] and Briant et al. [68] for calculating the liquid droplet behavior on partial wetted surfaces, typical for large density ratios gas-liquid systems. The snapshots of droplet spreading on a uniform hydrophilic surface with 45° contact angle are shown in Fig. 2.3. Moreover, Fakhar and Rahimian [74] found that the free-energy-based model [46] is not capable of dealing with two-phase flows with different densities and is mostly suitable for binary fluids for which the Boussinesq approximation holds. Until now, most of the studies focus on flat and inclined solid surfaces. Few studies focus on the simulation of a droplet impact on curved surfaces. Shen et al. [98] adopted the two-dimensional lattice Boltzmann pseudo-potential method to simulate the droplets impacting on curved solid surfaces. However, the gas-liquid density ratio is limited to unity.

2.4 Immiscible two-phase flow in porous media

In the past decades, several theoretical approaches have been developed to describe viscously coupled multiphase flow in porous medium systems. A volume averaging method was applied to Stokes equation to arrive at a modified theory which includes viscous coupling effects between two fluid phases [99–101]. Marle [102] and Kalaydjian [103, 104] employed an approach based on averaging and non-equilibrium thermodynamics to develop analogous transport equations describing the immiscible two-phase flow in isotropic media. A similar formulation named as generalized two-phase flow model was produced from these different theoretical approaches and their integrated form can be written as

$$\boldsymbol{v}_i = -\sum_{j=1}^{2} \frac{\kappa \kappa_{ij}}{\mu_j} \nabla p_j, \tag{2.5}$$

where i and j indicate wetting phase or non-wetting phase. The generalized relative permeability coefficients include two conventional coefficients, $k_{r,nn}$ and $k_{r,ww}$ and two off-diagonal coefficients, $k_{r,nw}$ and $k_{r,wn}$. Recently, the thermodynamically constrained averaging theory (TCAT) was proposed for modeling multiphase flows by Gray and Miller [105–107]. The TCAT approach is based on the work of Hassanizadeh and Gray [108], Bowen [109], Klaydjian [103] and the importance of fluid-fluid interfaces in multiphase systems has been distinguished and incorporated in model formulations.
Experimental research also attempted to quantify the interfacial coupling effect in the two-phase flow in porous media. Avraam and Payatakes [110–112] performed a series of experiments on a two-dimensional network of pore chambers and throats etched into

glass and explored the functional dependence of the relative permeability on the capillary number, wettability, viscosity ratio, and the ratio of injection flow rates. Four main flow regimes include large ganglion dynamics (LGD), small ganglion dynamics (SGD), drop traffic flow (DTF) and connected pathway flow (CPF) are identified(Fig. 2.4). It has been revealed that the steady-state water and oil relative permeabilities may differ substantially from the transient ones depending on the capillary number and wettability by recent experimental research [113]. The dimensionless parameters such as the capillary number and viscosity ratio can influence the capillary pressure and the relative permeability functions [114, 115]. Tsakiroglou et al. [114, 115], and Aggelopoulos and Tsakiroglou [116] presented the effect of pore space morphology on the transport properties and the capillary pressure-relative permeability relationship. It has been evident that non-random heterogeneities affect strongly the transient flow pattern and the shape of capillary pressure and relative permeability curves.

In addition to the theoretical study and experimental work, several computational

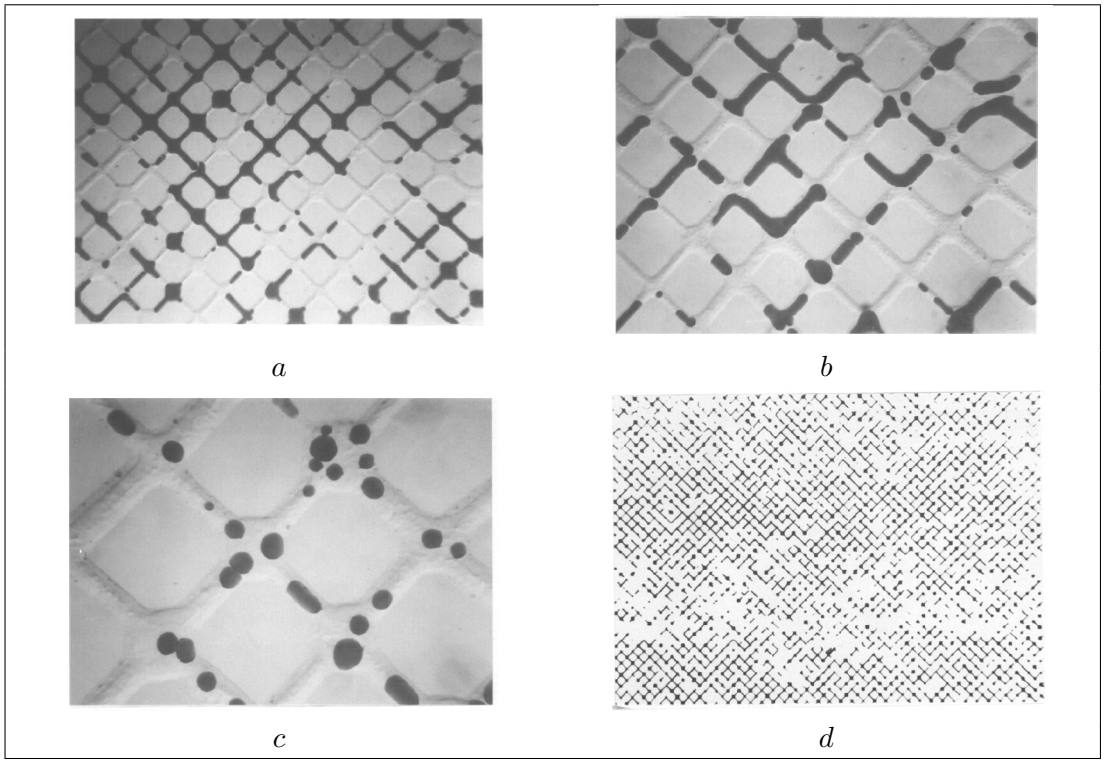

Figure 2.4: Snapshots from steady-state two-phase flow experiments corresponding to the main flow regimes (a) Large ganglion dynamics (LGD), (b) Small ganglion dynamics (SGD), (c) Drop traffic flow (DTF), (d) Connected pathway flow (CPF) [111].

approaches have been used for simulating multiphase flows in porous media. Ataie-Ashitiani et al. [117–119] adopted a numerical simulator named Subsurface transport over multiple phases (STOMP) and an implicit finite difference discretisation method to evaluate the influence of porous media heterogeneity on the relative permeabilities.

The STOMP simulator based on the standard finite volume spatial discretisation was used to investigate the effect of the variations in the nature, amount and distribution of micro-heterogeneities on the capillary pressure-saturation-relative permeability curves for dense non-aqueous phase liquids and water flow [120]. Further work revealed that there are significant effects on the flow direction and the orientation of samples with the high intensity of heterogeneity [121]. Another computational model which combines the grid-based computational fluid dynamics method with interface tracking/capturing and a contact angle model was reported for simulating multiphase flow in porous media [122–124]. In recent decades, network models have been used extensively to study a huge range of transport phenomena in porous media [125]. The predictive capabilities of network models have improved greatly with recent developments in constructing geologically realistic pore networks from microstructure images [126,127]. Joekar-Niasar et al. [128] adopted a quasi-static pore-network model to simulate the equilibrium states of drainage and imbibition processes without solving the pressure field. The relationships among interfacial area, capillary pressure, saturation and relative permeability were investigated. A new dynamic pore-network model was developed and has been applied on the research of two-phase flow in porous media [129–131].

In recent years, numerous investigations have shown that lattice Boltzmann models are capable of simulating multiphase flows in complex porous systems [5, 132]. Comparing with the network models, the advantage of the lattice Boltzmann model is that it can solve equations in an arbitrary pore space geometry and topology rather than in a simplification of the pore space geometry [129]. Several models have been developed for multiphase and multi-component flows during the last twenty years [43, 45–47]. Gunstensen and Rothman [133] investigated the flow of two immiscible fluids in two different three-dimensional microscopic models under a range of applied force and non-wetting fluid saturation by using the lattice Boltzmann model. The results implicated that the generalized two-phase flow model may be a good model for describing the fluid flow when the flow rate is high. A multi-relaxation time (MRT) approximation has also been adopted to evaluated viscous coupling effects in immiscible two-phase flow system [134]. Fig. 2.5 shows the snapshots of the non-wetting phase distribution with $Ca = 5 * 10^{-4}$. It was found that there is a strong correlation between the relative permeability and capillary number, wettability, the fluid viscosities, and interfacial area between the fluids. Yiotis et al. [135] applied the He-Shan-Doolen LB model to study the immiscible two-phase flow in porous media and reported that the relative permeability of the non-wetting phase may take values greater than unity due to the "lubricating" effect of the wetting films that cover the solid walls. The high-density-ratio gas-liquid flow relative permeabilities change with the wetting saturation S_w, capillary number Ca, and viscous ratio M in heterogeneous porous media has also been studied by using the LB model [136]. Dou and Zhou [137] applied a LB model to

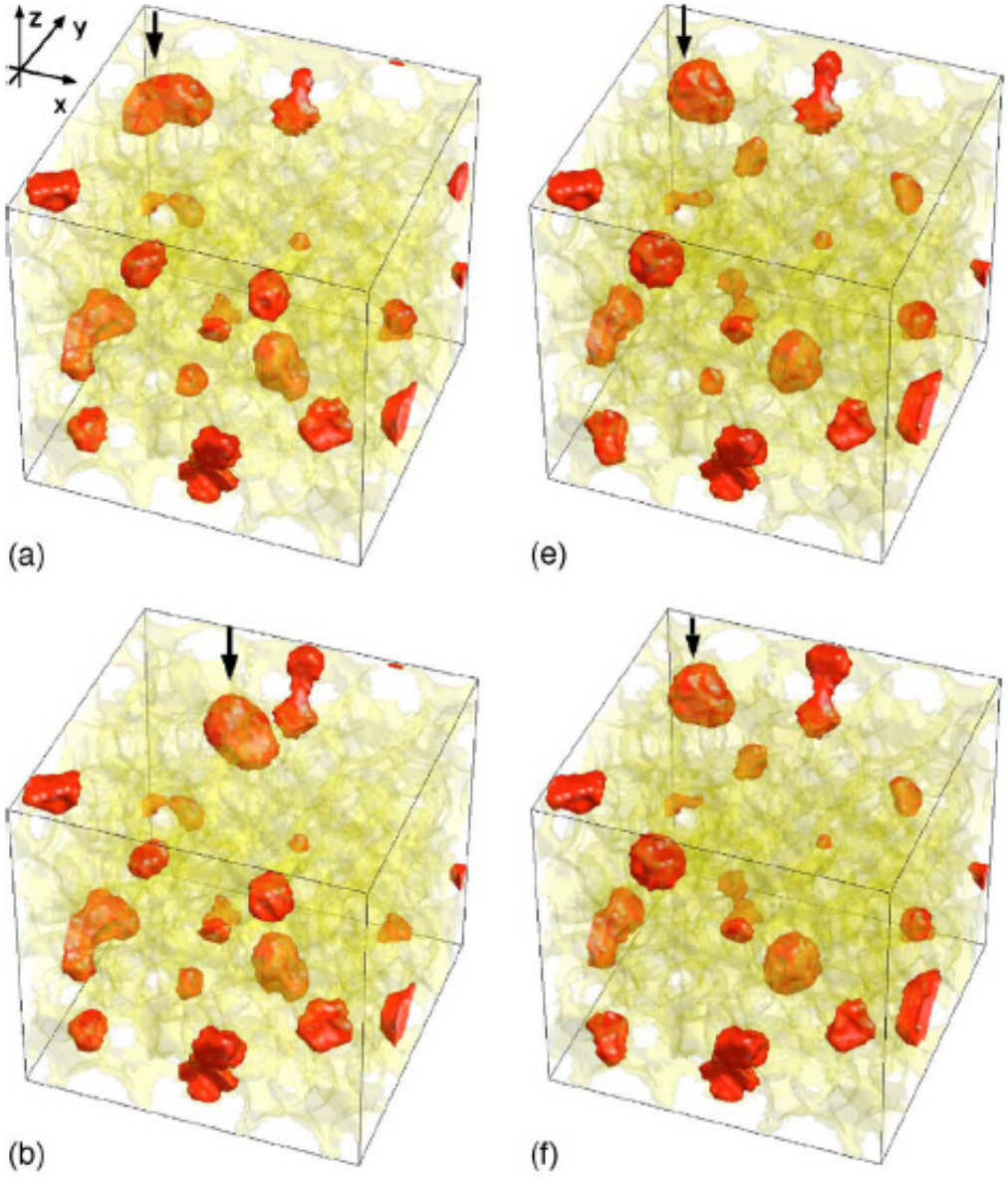

Figure 2.5: Snapshots of the nonwetting phase distribution under a higher capillary number with $Ca = 5 * 10^{-4}$ [132].

investigate the effects of capillary number and viscosity ratio on the non-uniqueness of the relationship between the relative permeabilities and saturation of phases for immiscible two-phase flow in the homogeneous and heterogeneous porous media. Yiotis et al. [138] studied the dynamics of non-wetting liquid blobs during the immiscible two-phase flow in stochastically reconstructed porous media by applying an immiscible LB model. These previously mentioned studies have revealed remarkable results for immiscible two-phase flows in porous media. However, to the best of the author's knowledge, there are no systematic LB numerical studies presented in the literature that address

the relationship between the geometrical properties and the relative permeabilities for immiscible two-phase flows in pore-scale porous media.

Chapter 3

Mathematical model

3.1 Shan-Chen multiphase model with Peng-Robinson equation of state

3.1.1 Pseudo-potential model

The particle distribution function is governed by the discretized Boltzmann equation with single relaxation time for the collision term [139]:

$$f_\alpha(\boldsymbol{x}+\boldsymbol{e}_\alpha\delta t, t+\delta t) = f_\alpha(\boldsymbol{x},t) - \frac{1}{\tau}[f_\alpha(\boldsymbol{x},t) - f_\alpha^{eq}(\boldsymbol{x},t)], \tag{3.1}$$

where f_α is the particle distribution function along the αth direction, f_α^{eq} is equilibrium distribution function, δt is the time step, $\boldsymbol{e}_\alpha$ is the particle velocity in the αth direction, τ is the single relaxation time. The viscosity in the LBM model is given by

$$\nu = (\tau - \frac{1}{2})c_s^2\delta t, \tag{3.2}$$

where $c_s = c/\sqrt{3}$ is the lattice sound speed, and $c = \delta x/\delta t$ is the ratio of lattice spacing δx and time step δt. The equilibrium distribution function $f_\alpha^{eq}(\boldsymbol{x},t)$ can be calculated from

$$f_\alpha^{eq} = \rho w_\alpha[1 + \frac{\boldsymbol{e}_\alpha\cdot\boldsymbol{u}^{eq}}{c_s^2} + \frac{(\boldsymbol{e}_\alpha\cdot\boldsymbol{u}^{eq})^2}{2c_s^4} - \frac{\boldsymbol{u}^{eq}\cdot\boldsymbol{u}^{eq}}{2c_s^2}], \tag{3.3}$$

where w_α is the weighting factor. In this paper, the D3Q19 model is adopted for the 3-dimensional simulations. The weighting factor and discrete velocity for D3Q19 are given by

$$\left[\ \boldsymbol{e}_0,\boldsymbol{e}_1,\boldsymbol{e}_2,\boldsymbol{e}_3,\boldsymbol{e}_4,\boldsymbol{e}_5,\boldsymbol{e}_6,\boldsymbol{e}_7,\boldsymbol{e}_8,\boldsymbol{e}_9,\boldsymbol{e}_{10},\boldsymbol{e}_{11},\boldsymbol{e}_{12},\boldsymbol{e}_{13},\boldsymbol{e}_{14},\boldsymbol{e}_{15},\boldsymbol{e}_{16},\boldsymbol{e}_{17},\boldsymbol{e}_{18}\ \right] =$$

$$\begin{bmatrix} 0 & 1 & -1 & 0 & 0 & 0 & 0 & 1 & 1 & -1 & -1 & 1 & -1 & 1 & -1 & 0 & 0 & 0 & 0 \\ 0 & 0 & 0 & 1 & -1 & 0 & 0 & 1 & -1 & 1 & -1 & 0 & 0 & 0 & 0 & 1 & 1 & -1 & -1 \\ 0 & 0 & 0 & 0 & 0 & 1 & -1 & 0 & 0 & 0 & 0 & 1 & 1 & -1 & -1 & 1 & -1 & 1 & -1 \end{bmatrix}, \tag{3.4}$$

$$w_\alpha = \begin{cases} 1/3, & \alpha = 0; \\ 1/18, & \alpha = 1, 2, \ldots, 6; \\ 1/36, & \alpha = 7, 8, \ldots, 18; \end{cases} \tag{3.5}$$

The local density and local momentum are given by

$$\rho(\boldsymbol{x}, t) = \sum_{\alpha=0}^{N} f_\alpha(\boldsymbol{x}, t), \tag{3.6}$$

and

$$\rho \boldsymbol{u}(\boldsymbol{x}, t) = \sum_{\alpha=0}^{N} \boldsymbol{e}_\alpha f_\alpha(\boldsymbol{x}, t). \tag{3.7}$$

The equilibrium value of the velocity $\boldsymbol{u}^{eq}$ used in eq. (3.3) is given by

$$\boldsymbol{u}^{eq} = \boldsymbol{u} + \frac{\tau \boldsymbol{F}_{total}}{\rho(\boldsymbol{x})}. \tag{3.8}$$

In eq. (3.8), $\boldsymbol{F}_{total} = \boldsymbol{F}_{cohesion} + \boldsymbol{F}_{adhesion} + \boldsymbol{F}_{body}$ is the total force on each particle, here including the fluid-fluid cohesion force $\boldsymbol{F}_{cohesion}$, the fluid-solid adhesion force $\boldsymbol{F}_{adhesion}$ and the body force $\boldsymbol{F}_{body}$.

3.1.2 Fluid-fluid cohesion

It is commonly accepted that the segregation of different phases is microscopically due to the long-range interaction force between the particles at site $\boldsymbol{x}$ and the particles at neighbor sites $\boldsymbol{x}'$ [45]. The interaction force is defined as

$$\boldsymbol{F}_{cohesion}(\boldsymbol{x}) = -\psi(\boldsymbol{x}) \sum_{\boldsymbol{x}'} G(\boldsymbol{x}, \boldsymbol{x}')\psi(\boldsymbol{x}')(\boldsymbol{x}' - \boldsymbol{x}), \tag{3.9}$$

where $G(\boldsymbol{x}, \boldsymbol{x}')$ is Green's function and satisfies $G(\boldsymbol{x}, \boldsymbol{x}') = G(\boldsymbol{x}', \boldsymbol{x})$. It reflects the intensity of the interparticle interactions and is given by

$$G(\boldsymbol{x}, \boldsymbol{x}') = \begin{cases} g, & |\boldsymbol{x} - \boldsymbol{x}'| = 1, \\ g/2, & |\boldsymbol{x} - \boldsymbol{x}'| = \sqrt{2}, \\ 0, & otherwise. \end{cases} \tag{3.10}$$

In eq. (3.9), $\psi(\boldsymbol{x})$ is the effective mass, which is a function of the local density and can be varied to reflect different fluid and fluid mixture behaviors, as represented by various equations. The equation of state (EOS) of the system is given by

$$p = c_s^2 \rho + \frac{c_0}{2} g[\psi(\rho)]^2. \tag{3.11}$$

and the effective mass can be defined as:

$$\psi(\rho) = \sqrt{\frac{2(p - c_s^2\rho)}{c_0 g}}, \tag{3.12}$$

where c_0=6.0 for the D3Q19, and p is the pressure. In Yuan and Schaefer's study [17], five different EOS were compared, and it was found that Peng-Robinson (PR) EOS provided the maximum density ratio while maintaining small spurious currents around the interface. Hence, the P-R EOS was adopted in our following multi-phase flow research, and can be expressed as:

$$p = \frac{\rho RT}{1 - b\rho} - \frac{a\alpha(T)\rho^2}{1 + 2b\rho - b^2\rho^2}, \tag{3.13}$$

where

$$\alpha(T) = [1 + (0.37464 + 1.5422\omega - 0.26992\omega^2)(1 - \sqrt{T/T_c})]^2. \tag{3.14}$$

The attraction parameter $a = 0.45724R^2T_c^2/p_c$, the repulsion parameter $b = 0.0778RT_c/p_c$, and ω is the acentric factor. T_c and P_c are the critical temperature and critical pressure respectively. The density ratio and interfacial surface tension are governed by the temperature T, and parameters a and b respectively. Substituting eq. (3.13) into eq. (3.12), we get

$$\psi(\rho) = \sqrt{\frac{2(\frac{\rho RT}{1-b\rho} - \frac{a\alpha(T)\rho^2}{1+2b\rho-b^2\rho^2} - c_s^2\rho)}{c_0 g}}. \tag{3.15}$$

Unlike in the original SC model, the value of the coefficient of interaction strength, g, becomes unimportant. Indeed, it is canceled out when eq. (3.12) is substituted into eq. (3.9). The only requirement for g is to ensure that the term inside the square root in eq. (3.12) is positive, (i.e $g = sgn(p - c_s^2\rho)$ has to be stored when eq. (3.12) is computed).

3.1.3 Fluid-solid adhesion and body force

At the fluid-solid interface, the interaction between the fluid and solid needs to be considered. Hence the force applied on a particle that comes in contact with the solid wall is

$$\boldsymbol{F}_{adhesion} = -\rho(\boldsymbol{x}) \sum_{x'} G_w(\boldsymbol{x}, \boldsymbol{x}')\rho_w(\boldsymbol{x}')(\boldsymbol{x}' - \boldsymbol{x}), \tag{3.16}$$

where $G_w(\boldsymbol{x}, \boldsymbol{x}')$ denotes the intensity of the fluid-solid interaction. For the D3Q19 model, it is defined as

$$G_w(\boldsymbol{x}, \boldsymbol{x}') = \begin{cases} G_w, & |\boldsymbol{x} - \boldsymbol{x}'| = 1, \\ G_w/2, & |\boldsymbol{x} - \boldsymbol{x}'| = \sqrt{2}, \\ 0, & otherwise. \end{cases} \tag{3.17}$$

Different contact angles can be obtained by adjusting G_w. The term $\rho_w(\boldsymbol{x}')$ in eq. (3.16) is the wall density, which equals one at the wall and zero in the fluid. In addition to interparticle and wall forces, the body force can be simply defined as

$$\boldsymbol{F}_{body}(\boldsymbol{x}) = \rho(\boldsymbol{x})\boldsymbol{g}. \tag{3.18}$$

3.2 Two-dimensional multi-relaxation time pseudopotential model

3.2.1 Incorporation of the force term

In the LBM model, the motion of a fluid is described by a set of discrete single-particle density distribution functions. According to the Guo et al. [58] forcing scheme, the particle distribution function with single relaxation time can be written as

$$f_\alpha(\boldsymbol{x} + \boldsymbol{e}_\alpha\delta t, t + \delta t) = f_\alpha(\boldsymbol{x}, t) - \frac{1}{\tau}[f_\alpha(\boldsymbol{x}, t) - f_\alpha^{eq}(\boldsymbol{x}, t)] + \boldsymbol{F}_\alpha, \tag{3.19}$$

where f_α is the particle distribution along the αth direction and f_α^{eq} is equilibrium distribution. δt is the time step, $\boldsymbol{e}_\alpha$ is the particle velocity in the αth direction, and τ is the single relaxation time. $\boldsymbol{F}_\alpha$ is the forcing term, in Guo et al. [58] forcing scheme is given by

$$\boldsymbol{F}_\alpha = (1 - \frac{1}{2\tau})w_\alpha[\frac{\boldsymbol{e}_\alpha - \boldsymbol{v}}{c_s^2} + \frac{(\boldsymbol{e}_\alpha \cdot \boldsymbol{v})}{c_s^4}\boldsymbol{e}_\alpha] \cdot \boldsymbol{F}. \tag{3.20}$$

Li et al. [60] proposed an improved version based on Guo et al. forcing scheme by using a modified velocity in the scheme, which leads to

$$\boldsymbol{F}_\alpha = (1 - \frac{1}{2\tau})w_\alpha[\frac{\boldsymbol{e}_\alpha - \boldsymbol{v}'}{c_s^2} + \frac{(\boldsymbol{e}_\alpha \cdot \boldsymbol{v}')}{c_s^4}\boldsymbol{e}_\alpha] \cdot \boldsymbol{F}. \tag{3.21}$$

The modified velocity $\boldsymbol{v}'$ is defined as $\boldsymbol{v}' = \boldsymbol{v} + \epsilon\boldsymbol{F}/((\tau - 0.5)\psi^2)$, where ψ is the effective mass and ϵ is a constant. $c_s = c/\sqrt{3}$ is the lattice sound speed, where $c = \delta x/\delta t$ is the ratio of lattice spacing δx and time step δt. The equilibrium distribution function $f_\alpha^{eq}(\boldsymbol{x}, t)$ in Eq. (3.19) can be calculated as

$$f_\alpha^{eq} = \rho w_\alpha[1 + \frac{\boldsymbol{e}_\alpha \cdot \boldsymbol{v}}{c_s^2} + \frac{(\boldsymbol{e}_\alpha \cdot \boldsymbol{v})^2}{2c_s^4} - \frac{\boldsymbol{v} \cdot \boldsymbol{v}}{2c_s^2}]. \tag{3.22}$$

where w_α is the weighting factor. In this paper, D2Q9 model will be adopted for 2D simulations. The discrete velocity and weighting factor for D2Q9 are given by

$$\left[\ \boldsymbol{e}_0, \boldsymbol{e}_1, \boldsymbol{e}_2, \boldsymbol{e}_3, \boldsymbol{e}_4, \boldsymbol{e}_5, \boldsymbol{e}_6, \boldsymbol{e}_7, \boldsymbol{e}_8\ \right] = \begin{bmatrix} 0 & 1 & 0 & -1 & 0 & 1 & -1 & -1 & 1 \\ 0 & 0 & 1 & 0 & -1 & 1 & 1 & -1 & -1 \end{bmatrix}. \tag{3.23}$$

$$w_\alpha = \begin{cases} 4/9, & \alpha = 0; \\ 1/9, & \alpha = 1,2,3,4; \\ 1/36, & \alpha = 5,6,7,8; \end{cases} \tag{3.24}$$

The corresponding macroscopic density and velocity are calculated by

$$\rho(\boldsymbol{x},t) = \sum_{\alpha=0}^{N} f_\alpha(\boldsymbol{x},t). \tag{3.25}$$

$$\rho\boldsymbol{v}(\boldsymbol{x},t) = \sum_{\alpha=0}^{N} \boldsymbol{e}_\alpha f_\alpha(\boldsymbol{x},t) + \frac{\boldsymbol{F}}{2}. \tag{3.26}$$

where N is the number of discrete particle velocities. $\boldsymbol{F} = \boldsymbol{F}_{cohesion} + \boldsymbol{F}_{adhesion} + \boldsymbol{F}_{body}$ is the total force on each particle, in this current study including fluid-fluid cohesion $\boldsymbol{F}_{cohesion}$, fluid-solid adhesion force $\boldsymbol{F}_{adhesion}$ and body force $\boldsymbol{F}_{body}$.

3.2.2 Multi-relaxation-time LBM model

In general the collision process involves multiple physical quantities that may relax on different time scales, and information for those time scales can be given using a collision matrix $\boldsymbol{\Omega}$ instead of a single time scale τ in Eq. (3.19). As a result, Eq. (3.19) is replaced by the following density distribution function:

$$f_\alpha(\boldsymbol{x}+\boldsymbol{e}_\alpha\delta t, t+\delta t) = f_\alpha(\boldsymbol{x},t) - \sum_\beta \boldsymbol{\Omega}_{\alpha\beta}[f_\beta(\boldsymbol{x},t) - f_\beta^{eq}(\boldsymbol{x},t)] + (S_\alpha(\boldsymbol{x},t) - 0.5\sum_\beta \boldsymbol{\Omega}_{\alpha\beta}S_\beta(\boldsymbol{x},t)). \tag{3.27}$$

where S is the forcing term in multi-relaxation-time LBM model which can be derived from Eq. (3.20) or Eq. (3.21). The collision step in the velocity space is difficult to perform. It is more convenient to perform the collision process in the momentum space. Hence, Eq. (3.27) can be transformed to the following form,

$$f_\alpha(\boldsymbol{x} + \boldsymbol{e}_\alpha\delta t, t+\delta t) = f_\alpha(\boldsymbol{x},t) - \boldsymbol{M}^{-1}\boldsymbol{\Lambda}[\boldsymbol{m}(\boldsymbol{x},t) - \boldsymbol{m}^{eq}(\boldsymbol{x},t)] + \boldsymbol{M}^{-1}(\boldsymbol{I} - \frac{\boldsymbol{\Lambda}}{2})\bar{\boldsymbol{S}}(\boldsymbol{x},t). \tag{3.28}$$

where $\boldsymbol{m}$ and $\boldsymbol{m}^{eq}$ are the moment space of the density distribution function f_α and its equilibrium distribution f_α^{eq} respectively. It can be obtained from $\boldsymbol{m} = \boldsymbol{M}\boldsymbol{f}$ and $\boldsymbol{m}^{eq} = \boldsymbol{M}\boldsymbol{f}^{eq}$ respectively. $\boldsymbol{M}$ is the transformation matrix, which for D2Q9 is

$$\boldsymbol{M} = \begin{bmatrix} 1 & 1 & 1 & 1 & 1 & 1 & 1 & 1 & 1 \\ -4 & -1 & -1 & -1 & -1 & 2 & 2 & 2 & 2 \\ 4 & -2 & -2 & -2 & -2 & 1 & 1 & 1 & 1 \\ 0 & 1 & 0 & -1 & 0 & 1 & -1 & -1 & 1 \\ 0 & -2 & 0 & 2 & 0 & 1 & -1 & -1 & 1 \\ 0 & 0 & 1 & 0 & -1 & 1 & 1 & -1 & -1 \\ 0 & 0 & -2 & 0 & 2 & 1 & 1 & -1 & -1 \\ 0 & 1 & -1 & 1 & -1 & 0 & 0 & 0 & 0 \\ 0 & 0 & 0 & 0 & 0 & 1 & -1 & 1 & -1 \end{bmatrix}. \tag{3.29}$$

The inverse of matrix $\boldsymbol{M}$ is

$$\boldsymbol{M}^{-1} = a \begin{bmatrix} 4 & -4 & 4 & 0 & 0 & 0 & 0 & 0 & 0 \\ 4 & -1 & -2 & 6 & -6 & 0 & 0 & 9 & 0 \\ 4 & -1 & -2 & 0 & 0 & 6 & -6 & -9 & 0 \\ 4 & -1 & -2 & -6 & 6 & 0 & 0 & 9 & 0 \\ 4 & -1 & -2 & 0 & 0 & -6 & 6 & -9 & 0 \\ 4 & 2 & 1 & 6 & 3 & 6 & 3 & 0 & 9 \\ 4 & 2 & 1 & -6 & -3 & 6 & 3 & 0 & -9 \\ 4 & 2 & 1 & -6 & -3 & -6 & -3 & 0 & 9 \\ 4 & 2 & 1 & 6 & 3 & -6 & -3 & 0 & -9 \end{bmatrix}, \tag{3.30}$$

where $a = 1/36$, $\boldsymbol{I}$ in Eq. (3.28) is the identity matrix and $\boldsymbol{\Lambda}$ is a diagonal matrix of multi-relaxation times which is given by

$$\boldsymbol{\Lambda} = diag(\tau_\rho^{-1}, \tau_e^{-1}, \tau_\zeta^{-1}, \tau_j^{-1}, \tau_q^{-1}, \tau_j^{-1}, \tau_q^{-1}, \tau_\nu^{-1}, \tau_\nu^{-1}). \tag{3.31}$$

The kinematic viscosity in the multi-relaxation-time lattice Boltzmann model is given by

$$\nu = (\tau_\nu - \frac{1}{2}) c_s^2 \delta t. \tag{3.32}$$

The $\bar{\boldsymbol{S}}$ in Eq. (3.28) is the forcing term in the moment space which can be calculated by $\bar{\boldsymbol{S}} = \boldsymbol{M}\boldsymbol{S}$. The force is incorporated via the following forcing scheme in the MRT LB method when the $\boldsymbol{S}$ is derived from Eq. (3.20) [140]:

$$\bar{\boldsymbol{S}} = \boldsymbol{M}\boldsymbol{S} = \begin{bmatrix} 0 \\ 6(v_x F_x + v_y F_y) \\ -6(v_x F_x + v_y F_y) \\ F_x \\ -F_x \\ F_y \\ -F_y \\ 2(v_x F_x - v_y F_y) \\ (v_x F_y + v_y F_x) \end{bmatrix}. \tag{3.33}$$

Li et al. [63] proposed an improved forcing scheme for MRT LB model based on the force term in Eq. (3.21). In current work, this improved forcing scheme is adopted.

$$\bar{\boldsymbol{S}} = \boldsymbol{M}\boldsymbol{S} = \begin{bmatrix} 0 \\ 6(v_x F_x + v_y F_y) + \frac{12\epsilon \boldsymbol{F}^2}{\Psi^2(\tau_e - 0.5)} \\ -6(v_x F_x + v_y F_y) - \frac{12\epsilon \boldsymbol{F}^2}{\Psi^2(\tau_\zeta - 0.5)} \\ F_x \\ -F_x \\ F_y \\ -F_y \\ 2(v_x F_x - v_y F_y) \\ (v_x F_y + v_y F_x) \end{bmatrix}. \tag{3.34}$$

3.3 New forcing scheme for the three-dimensional multi-relaxation time lattice-Boltzmann model

An improved force scheme is proposed for the three-dimensional MRT pseudopotential lattice Boltzmann model which is based on the improved force scheme for the single relaxation time (SRT) pseudopotential lattice Botlzmann model ([60]) and the Chapman-Enskog analysis ([141]). This three-dimensional multi-relaxation-time lattice Boltzmann model can handle multiphase flows at high density ratios and low viscosities. The proposed MRT multiphase model is evaluated by verifying Laplace's law and achieving thermodynamic consistency for a static droplet. Moreover, a relationship between the fluid-solid interaction potential parameter and the contact angle is investigated.

3.3.1 3D multi-relaxation-time LBM model for multi-phase flows

In the LBM model, the motion of a fluid is described by a set of discrete single-particle density distribution functions. According to the [58] forcing scheme, the lattice Boltzmann equation with single relaxation time can be written as

$$f_\alpha(\boldsymbol{x}+\boldsymbol{e}_\alpha\delta t, t+\delta t) = f_\alpha(\boldsymbol{x},t) - \frac{1}{\tau}[f_\alpha(\boldsymbol{x},t) - f_\alpha^{eq}(\boldsymbol{x},t)] + \boldsymbol{F}_\alpha, \tag{3.35}$$

where f_α is the particle distribution along the αth direction, f_α^{eq} is the equilibrium distribution, δt is the time step, $\boldsymbol{e}_\alpha$ is the particle velocity in the αth direction, τ is the single relaxation time and $\boldsymbol{F}_\alpha$ is the forcing term. Li et al. [60] proposed an improved version based on the Guo et al. [58] forcing scheme by using a modified velocity, which leads to

$$\boldsymbol{F}_\alpha = (1-\frac{1}{2\tau})w_\alpha[\frac{\boldsymbol{e}_\alpha - \boldsymbol{v}'}{c_s^2} + \frac{(\boldsymbol{e}_\alpha\cdot\boldsymbol{v}')}{c_s^4}\boldsymbol{e}_\alpha]\cdot\boldsymbol{F}. \tag{3.36}$$

The modified velocity $\boldsymbol{v}'$ is defined as $\boldsymbol{v}' = \boldsymbol{v} + \epsilon\boldsymbol{F}/((\tau-0.5)\psi^2)$, where ψ is the effective mass and ϵ is a constant. $\boldsymbol{F} = \boldsymbol{F}_{cohesion} + \boldsymbol{F}_{adhesion} + \boldsymbol{F}_{body}$ is the total force on each particle, including the fluid-fluid cohesion $\boldsymbol{F}_{cohesion}$, the fluid-solid adhesion force $\boldsymbol{F}_{adhesion}$ and the body force $\boldsymbol{F}_{body}$. The equilibrium distribution function $f_\alpha^{eq}(\boldsymbol{x},t)$ is expressed as [45]

$$f_\alpha^{eq} = \rho w_\alpha[1 + \frac{\boldsymbol{e}_\alpha\cdot\boldsymbol{v}}{c_s^2} + \frac{(\boldsymbol{e}_\alpha\cdot\boldsymbol{v})^2}{2c_s^4} - \frac{\boldsymbol{v}\cdot\boldsymbol{v}}{2c_s^2}], \tag{3.37}$$

where w_α is the weighting factor. In this study, the D3Q19 model is adopted for the 3D simulations. The discrete velocity and the weighting factor for the D3Q19 are given by Eq.3.4 and Eq.3.5

Generally, the collision process involves multiple physical quantities that may relax on different time scales, and information for those time scales can be given using a

collision matrix $\mathbf{\Omega}$ instead of a single time scale τ in Eq. (3.35). As a result, Eq. (3.35) is replaced by the following lattice Boltzmann equation [142]:

$$f_\alpha(\boldsymbol{x}+\boldsymbol{e}_\alpha\delta t, t+\delta t) = f_\alpha(\boldsymbol{x},t) - \sum_\beta \mathbf{\Omega}_{\alpha\beta}[f_\beta(\boldsymbol{x},t) - f_\beta^{eq}(\boldsymbol{x},t)] + (S_\alpha(\boldsymbol{x},t) - 0.5\sum_\beta \mathbf{\Omega}_{\alpha\beta}S_\beta(\boldsymbol{x},t)), \tag{3.38}$$

where S is the forcing term in the multi-relaxation-time LBM model. From Eq. (3.36)

$$S_\alpha = w_\alpha[\frac{\boldsymbol{e}_\alpha - \boldsymbol{v}'}{c_s^2} + \frac{(\boldsymbol{e}_\alpha \cdot \boldsymbol{v}')}{c_s^4}\boldsymbol{e}_\alpha] \cdot \boldsymbol{F}. \tag{3.39}$$

Eq. (3.38) can be mapped onto the moment space by multiplying throughout by a transformation matrix $\boldsymbol{M}$ [61]. Hence, Eq. (3.38) can be transformed into the following form,

$$f_\alpha(\boldsymbol{x}+\boldsymbol{e}_\alpha\delta t, t+\delta t) = f_\alpha(\boldsymbol{x},t) - \boldsymbol{M^{-1}}\mathbf{\Lambda}[\boldsymbol{m}(\boldsymbol{x},t) - \boldsymbol{m}^{eq}(\boldsymbol{x},t)] + \boldsymbol{M^{-1}}(\boldsymbol{I} - \frac{\mathbf{\Lambda}}{2})\bar{\boldsymbol{S}}(\boldsymbol{x},t), \tag{3.40}$$

where $\boldsymbol{m}$ and $\boldsymbol{m}^{eq}$ are the moment space of the density distribution function f_α and its equilibrium distribution f_α^{eq}. It can be derived from $\boldsymbol{m} = \boldsymbol{M}\boldsymbol{f}$ and $\boldsymbol{m}^{eq} = \boldsymbol{M}\boldsymbol{f}^{eq}$, respectively, where $\boldsymbol{M}$ is the transformation matrix. The matrix $\boldsymbol{M}$ for the D3Q19 is

$$\boldsymbol{M} = \begin{bmatrix}
1 & 1 & 1 & 1 & 1 & 1 & 1 & 1 & 1 & 1 & 1 & 1 & 1 & 1 & 1 & 1 & 1 & 1 & 1 \\
-30 & -11 & -11 & -11 & -11 & -11 & -11 & 8 & 8 & 8 & 8 & 8 & 8 & 8 & 8 & 8 & 8 & 8 & 8 \\
12 & -4 & -4 & -4 & -4 & -4 & -4 & 1 & 1 & 1 & 1 & 1 & 1 & 1 & 1 & 1 & 1 & 1 & 1 \\
0 & 1 & 0 & 0 & -1 & 0 & 0 & 1 & 1 & 0 & -1 & -1 & 0 & 1 & 1 & 0 & -1 & -1 & 0 \\
0 & -4 & 0 & 0 & 4 & 0 & 0 & 1 & 1 & 0 & -1 & -1 & 0 & 1 & 1 & 0 & -1 & -1 & 0 \\
0 & 0 & 1 & 0 & 0 & -1 & 0 & 1 & 0 & 1 & -1 & 0 & -1 & -1 & 0 & 1 & 1 & 0 & -1 \\
0 & 0 & -4 & 0 & 0 & 4 & 0 & 1 & 0 & 1 & -1 & 0 & -1 & -1 & 0 & 1 & 1 & 0 & -1 \\
0 & 0 & 0 & 1 & 0 & 0 & -1 & 0 & 1 & 1 & 0 & -1 & -1 & 0 & -1 & -1 & 0 & 1 & 1 \\
0 & 0 & 0 & -4 & 0 & 0 & 4 & 0 & 1 & 1 & 0 & -1 & -1 & 0 & -1 & -1 & 0 & 1 & 1 \\
0 & 2 & -1 & -1 & 2 & -1 & -1 & 1 & 1 & -2 & 1 & 1 & -2 & 1 & 1 & -2 & 1 & 1 & -2 \\
0 & -4 & 2 & 2 & -4 & 2 & 2 & 1 & 1 & -2 & 1 & 1 & -2 & 1 & 1 & -2 & 1 & 1 & -2 \\
0 & 0 & 1 & -1 & 0 & 1 & -1 & 1 & -1 & 0 & 1 & -1 & 0 & 1 & -1 & 0 & 1 & -1 & 0 \\
0 & 0 & -2 & 2 & 0 & -2 & 2 & 1 & -1 & 0 & 1 & -1 & 0 & 1 & -1 & 0 & 1 & -1 & 0 \\
0 & 0 & 0 & 0 & 0 & 0 & 0 & 1 & 0 & 0 & 1 & 0 & 0 & -1 & 0 & 0 & -1 & 0 & 0 \\
0 & 0 & 0 & 0 & 0 & 0 & 0 & 0 & 0 & 1 & 0 & 0 & 1 & 0 & 0 & -1 & 0 & 0 & -1 \\
0 & 0 & 0 & 0 & 0 & 0 & 0 & 0 & 1 & 0 & 0 & 1 & 0 & 0 & -1 & 0 & 0 & -1 & 0 \\
0 & 0 & 0 & 0 & 0 & 0 & 0 & 1 & -1 & 0 & -1 & 1 & 0 & 1 & -1 & 0 & -1 & 1 & 0 \\
0 & 0 & 0 & 0 & 0 & 0 & 0 & -1 & 0 & 1 & 1 & 0 & -1 & 1 & 0 & 1 & -1 & 0 & -1 \\
0 & 0 & 0 & 0 & 0 & 0 & 0 & 0 & 1 & -1 & 0 & -1 & 1 & 0 & -1 & 1 & 0 & 1 & -1
\end{bmatrix}. \tag{3.41}$$

The $\boldsymbol{M}^{-1}$ is the inverse of matrix $\boldsymbol{M}$. The equilibrium distribution functions $\boldsymbol{m}^{eq}$ in the moment space are related to those in velocity space by

$$\boldsymbol{m}^{eq} = \boldsymbol{M}\boldsymbol{f}^{eq} = \begin{bmatrix} \rho \\ -11\rho + 19\frac{{j_x}^2+{j_y}^2+{j_z}^2}{\rho} \\ 3\rho - \frac{11}{2}\frac{{j_x}^2+{j_y}^2+{j_z}^2}{\rho} \\ j_x \\ -\frac{2}{3}j_x \\ j_y \\ -\frac{2}{3}j_y \\ j_z \\ -\frac{2}{3}j_z \\ \frac{2{j_x}^2-({j_y}^2+{j_z}^2)}{\rho} \\ -\frac{1}{2}\frac{2{j_x}^2-({j_y}^2+{j_z}^2)}{\rho} \\ \frac{{j_y}^2-{j_z}^2}{\rho} \\ -\frac{1}{2}\frac{{j_y}^2-{j_z}^2}{\rho} \\ \frac{j_x j_y}{\rho} \\ \frac{j_y j_z}{\rho} \\ \frac{j_x j_z}{\rho} \\ 0 \\ 0 \\ 0 \end{bmatrix}, \tag{3.42}$$

where j_x, j_y and j_z are the components of the momentum, j_x=ρu_x, j_y=ρu_y and j_z=ρu_z. $\boldsymbol{I}$ in Eq. (3.40) is the identity matrix and $\boldsymbol{\Lambda}$ is a diagonal matrix which is given by

$$\boldsymbol{\Lambda} = diag(s_1, s_2, s_3, s_4, s_5, s_6, s_7, s_8, s_9, s_{10}, s_{11}, s_{12}, s_{13}, s_{14}, s_{15}, s_{16}, s_{17}, s_{18}, s_{19}). \tag{3.43}$$

The bulk viscosity and kinematic viscosity in the multi-relaxation-time lattice Boltzmann model are given by

$$\xi = \frac{2}{9}(\frac{1}{s_2} - \frac{1}{2}), \tag{3.44}$$

and

$$\nu = \frac{1}{3}(\frac{1}{s_\beta} - \frac{1}{2}), \beta = 10, 12, 14, 15, 16. \tag{3.45}$$

Li et al. [60] showed that the numerical stability of the Shan-Chen and EDM schemes is related to an additional term in their recovered macroscopic equations. Based on the theoretical analysis, a SRT improved forcing scheme which is more stable than Shan-Chen, Guo and EDM schemes was presented. The two dimensional macroscopic equations recovered from the improved forcing scheme were shown in their study [60]. Similar to the two dimensional macroscopic equations, the macroscopic equations for the three dimensional case are given by

$$\partial_t \rho + \partial_x(\rho v_x) + \partial_y(\rho v_y) + \partial_z(\rho v_z) = 0, \tag{3.46}$$

$$\partial_t(\rho v_x) + \partial_x(\rho v_x v_x) + \partial_y(\rho v_x v_y) + \partial_z(\rho v_x v_z) = -\partial_x(\rho c_s^2) + F_x + \partial_x(2\nu[\partial_x(\rho v_x) - \frac{1}{3}\nabla\cdot(\rho\boldsymbol{v})] + \xi\nabla\cdot(\rho\boldsymbol{v})) + \partial_y(\nu(\partial_x(\rho v_y) + \partial_y(\rho v_x))) + \partial_z(\nu(\partial_x(\rho v_z) + \partial_z(\rho v_x))) - 2G^2c^4\epsilon\partial_x(|\nabla\Psi|^2) + O(\partial^5), \tag{3.47}$$

$$\partial_t(\rho v_y) + \partial_x(\rho v_x v_y) + \partial_y(\rho v_y v_y) + \partial_z(\rho v_y v_z) = -\partial_y(\rho c_s^2) + F_y + \partial_x(\nu(\partial_x(\rho v_y) + \partial_y(\rho v_x))) + \partial_y(2\nu[\partial_y(\rho v_y) - \frac{1}{3}\nabla\cdot(\rho\boldsymbol{v})] + \xi\nabla\cdot(\rho\boldsymbol{v})) + \partial_z(\nu(\partial_y(\rho v_z) + \partial_z(\rho v_y))) - 2G^2c^4\epsilon\partial_y(|\nabla\Psi|^2) + O(\partial^5), \tag{3.48}$$

$$\partial_t(\rho v_z) + \partial_x(\rho v_x v_z) + \partial_y(\rho v_y v_z) + \partial_z(\rho v_z v_z) = -\partial_z(\rho c_s^2) + F_z + \partial_x(\nu(\partial_x(\rho v_z) + \partial_z(\rho v_x))) + \partial_y(\nu(\partial_y(\rho v_z) + \partial_z(\rho v_y))) + \partial_z(2\nu[\partial_z(\rho v_z - \frac{1}{3}\nabla\cdot(\rho\boldsymbol{v}))] + \xi\nabla\cdot(\rho\boldsymbol{v})) - 2G^2c^4\epsilon\partial_z(|\nabla\Psi|^2) + O(\partial^5), \tag{3.49}$$

where G and c are constants equal to 1, ϵ is a constant which can be adjusted to fit the mechanical stability solution with the solution given by the Maxwell construction as well as to enhance the numerical stability [60].
The corresponding macroscopic density and velocity are calculated by

$$\rho(\boldsymbol{x},t) = \sum_{\alpha=0}^{N} f_\alpha(\boldsymbol{x},t), \tag{3.50}$$

and

$$\rho\boldsymbol{v}(\boldsymbol{x},t) = \sum_{\alpha=0}^{N} \boldsymbol{e}_\alpha f_\alpha(\boldsymbol{x},t) + \frac{\boldsymbol{F}}{2}, \tag{3.51}$$

where N is the number of discrete particle velocities. According to Eqs. (A.45), (A.46), (A.47), the pressure tensor is defined as

$$\nabla\cdot\boldsymbol{P}_{new} = \nabla\cdot\boldsymbol{P} + 2G^2c^4\epsilon\nabla\cdot(|\nabla\Psi|^2\boldsymbol{I}), \tag{3.52}$$

where

$$\nabla\cdot\boldsymbol{P} = \nabla\cdot(\rho c_s^2\boldsymbol{I}) - \boldsymbol{F}. \tag{3.53}$$

The term $\bar{\boldsymbol{S}}$ in Eq. (3.40) is the forcing term in the moment space. In the current work, a MRT force scheme which is able to recover the 3-dimensional macroscopic Eqs (A.45), (A.46), (A.47) is proposed. According to the Chapman-Enskog analysis [141], the 3D MRT force scheme is given by

$$\bar{\boldsymbol{S}} = \begin{bmatrix} 0 \\ 38(v_xF_x + v_yF_y + v_zF_z) + \frac{114\epsilon \boldsymbol{F}^2}{\psi^2(1/s_2 - 0.5)} \\ -11(v_xF_x + v_yF_y + v_zF_z) \\ F_x \\ -\frac{2}{3}F_x \\ F_y \\ -\frac{2}{3}F_y \\ F_z \\ -\frac{2}{3}F_z \\ 2(2v_xF_x - v_yF_y - v_zF_z) \\ -2v_xF_x + v_yF_y + v_zF_z \\ 2(v_yF_y - v_zF_z) \\ -v_yF_y + v_zF_z \\ v_yF_x + v_xF_y \\ v_zF_y + v_yF_z \\ v_zF_x + v_xF_z \\ 0 \\ 0 \\ 0 \end{bmatrix}. \tag{3.54}$$

where $\boldsymbol{F}^2 = (F_x^2 + F_y^2 + F_z^2)$ and $\psi(\boldsymbol{x})$ is the effective mass, which is a function of the local density and can be varied to reflect different fluid and fluid mixture behaviors, as represented by various equations. The equation of state (EOS) of the system is given by

$$p = c_s^2\rho + \frac{c_0}{2}g[\psi(\rho)]^2, \tag{3.55}$$

and then the effective mass can be defined as:

$$\psi(\rho) = \sqrt{\frac{2(p - c_s^2\rho)}{c_0 g}}, \tag{3.56}$$

where c_0=6.0 for the D3Q19, and p is the pressure. In Yuan and Schaefer's study [17], five different EOS were compared, and it was found that the Peng-Robinson (P-R) EOS provided the maximum density ratio while maintaining small spurious currents around the interface. Hence, the P-R EOS was adopted in our multiphase flow research, which is expressed as:

$$p = \frac{\rho RT}{1 - b\rho} - \frac{a\alpha(T)\rho^2}{1 + 2b\rho - b^2\rho^2}, \tag{3.57}$$

where

$$\alpha(T) = [1 + (0.37464 + 1.5422\omega - 0.26992\omega^2)(1 - \sqrt{T/T_c})]^2. \tag{3.58}$$

The terms $a = 0.45724R^2T_c^2/p_c$ and $b = 0.0778RT_c/p_c$, where a is the attraction parameter, b is the volumetric or repulsion parameter, and ω is the acentric factor. T_c and P_c are the critical temperature and critical pressure, respectively. The density ratio

and surface tension of the liquid is governed by the temperature T, and parameters a and b respectively. Substituting Eq. (3.57) into Eq. (3.56), we get

$$\psi(\rho) = \sqrt{\frac{2(\frac{\rho RT}{1-b\rho} - \frac{a\alpha(T)\rho^2}{1+2b\rho-b^2\rho^2} - c_s^2\rho)}{c_0 g}}. \tag{3.59}$$

Unlike in the original SC model, the value of the coefficient of the interaction strength g becomes unimportant, because g is canceled out when calculating the interaction force and pressure [17]. The requirement for g is to ensure that the term inside the square root in Eq. (3.56) is positive, (i.e $g = sgn(p - c_s^2\rho)$ has to be stored when computing Eq. (3.56)).

3.3.2 Evaluation of surface tension

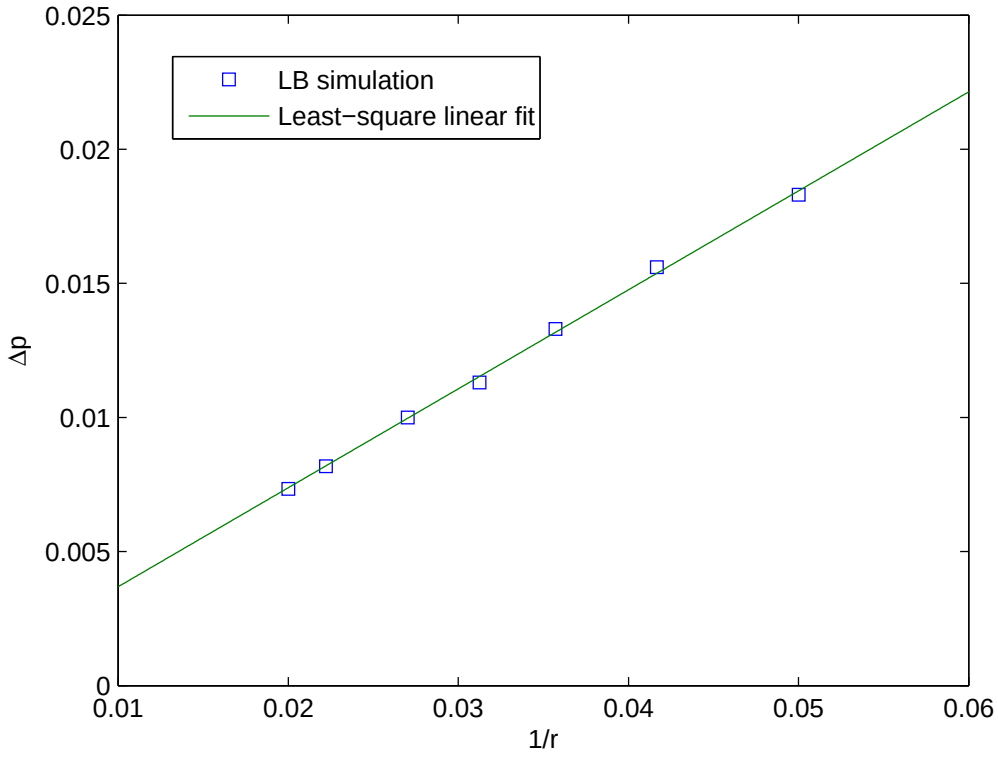

Figure 3.1: Evaluation of Laplace's law, the slope is 0.3690; the intercept is 0.000002136; and the coefficient of determination is 0.9999.

The satisfaction of Laplace law is an important benchmark test. The Laplace law for three dimensional states is

$$\Delta p = p_{in} - p_{out} = \frac{2\sigma}{r}, \tag{3.60}$$

where p_{in} and p_{out} are the pressures inside and outside the droplet, respectively. Δp, σ, r are the pressure difference, surface tension coefficient and the radius of the droplet. Stationary droplets with different radii are generated inside the domain with 120×120×120 lattice points and periodic boundary conditions to test if the results from simulations follow Laplace's law. The parameters are fixed at R=1, a=1/49, b=2/21, ω=0.344, T=0.61T_c, s_β=1/0.6 and ϵ=0.3. The final droplet radius and pressure difference inside and outside of the droplet are measured after 18000 time steps. The steady-state pressure inside(p_{in}) and outside the droplet(p_{out}) is measured on nodes located away from the interface since pressure values vary near it. The pressure jump is plotted as a function of the curvature in Fig. 3.1. The droplet radius, pressure difference and calculated surface tension are all in lattice units. The square marker in Fig. 3.1 indicates the results of the LB simulations whereas the solid line is the least-square linear fit. The slope equals to 0.3592 which corresponds to a surface tension of 0.1845; the intercept is 0.000002136; and the coefficient of determination is 0.9999. It is can be seen that all points fit a straight line. The pressure difference between the inside and outside of the droplet is proportional to the curvature. The agreement between the Laplace law and the numerical simulation indicates that the 3D MRT LBM model with the improved force scheme can handle the high density ratio multi-phase flow accurately. However, as it occurs in other pseudopotential lattice Boltzmann models, the surface tension in the current model cannot not be predicted in advance and can not be tuned independently.

3.3.3 Evaluation of thermodynamic consistency

A series of numerical simulations of stationary droplets are conducted to validate the proposed new 3D MRT lattice Boltzmann model. The problem of stationary droplets with different values of T, can be used to compare the numerical coexistence curve with the coexistence curve given by the Maxwell construction.

In order to verify the thermodynamic consistency, a stationary droplet with a radius of r=25 is initially placed at the center of the domain with 100×100×100 lattice points. Periodic boundary condition are applied on both sides of the domain. The parameters are fixed at R=1, a=1/49, b=2/21, ω=0.344, s_β=1/0.6 and ϵ=0.3. The coexistence curves are shown in Fig. 3.2. It can be seen that the simulation results are in good agreement with the results from the Maxwell construction. In addition to that, it can be seen that the proposed MRT lattice Boltzmann model with the improved force scheme works well at T/T_c=0.6, which corresponds to $\rho_l/\rho_g = 863$. This is a clear demonstration that the proposed 3D MRT lattice Boltzmann model is capable of handling large density ratio multiphase flows and achieve thermodynamic consistency. According to numerical experimentation with the single-relaxation-time model, the largest achievable density ratio is approximately 150 for the case of s_β=1/0.6. In contrast to that,

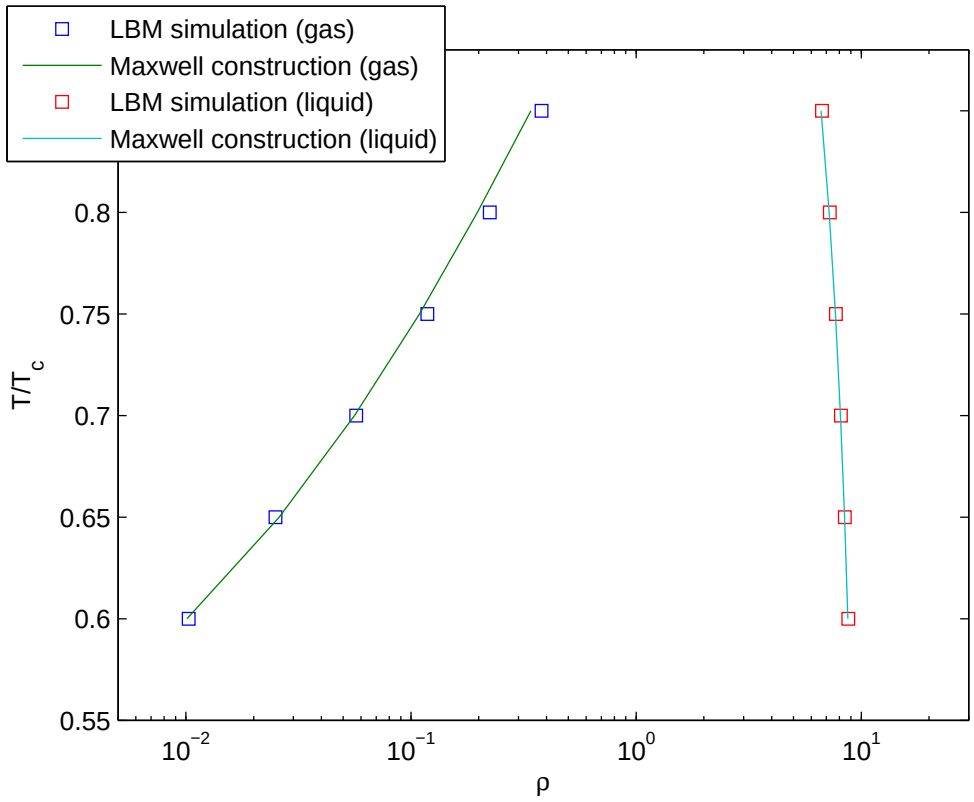

Figure 3.2: Comparison of the numerical coexistence curves predicted by the improved 3D MRT lattice Boltzmann model with the coexistence curves given by the Maxwell construction.

the 3D MRT model works well at $T/T_c \geq 0.57$, which corresponds to $\rho_l/\rho_g \leq 1700$.

3.3.4 Evaluation of the contact angle

Different static contact angles can be achieved by adjusting the fluid-solid interaction G_w.In this simulation, no body force is applied, and a stationary droplet with a radius of r=20 is initially placed at the bottom surface. The domain size is 100×100×100 lattice nodes, and the parameters are fixed at R=1, a=1/49, b=2/21, ω=0.344, s_β=1/0.6 and ϵ=0.3. Periodic boundary conditions are applied on all sides except for the upper and bottom sides. The half-bounce back wall boundary condition is applied on these two sides. The fluid-solid interaction G_w ranges between -2.8 to -1.6. A static droplet is obtained after 8000 time steps. The wet length between the droplet, the wall b_0 and the droplet height a_0 can be measured from the static droplet. The values of the radius r and the contact angle θ are calculated by

$$r = \frac{a_0}{2} + \frac{b_0^2}{8a_0}. \tag{3.61}$$

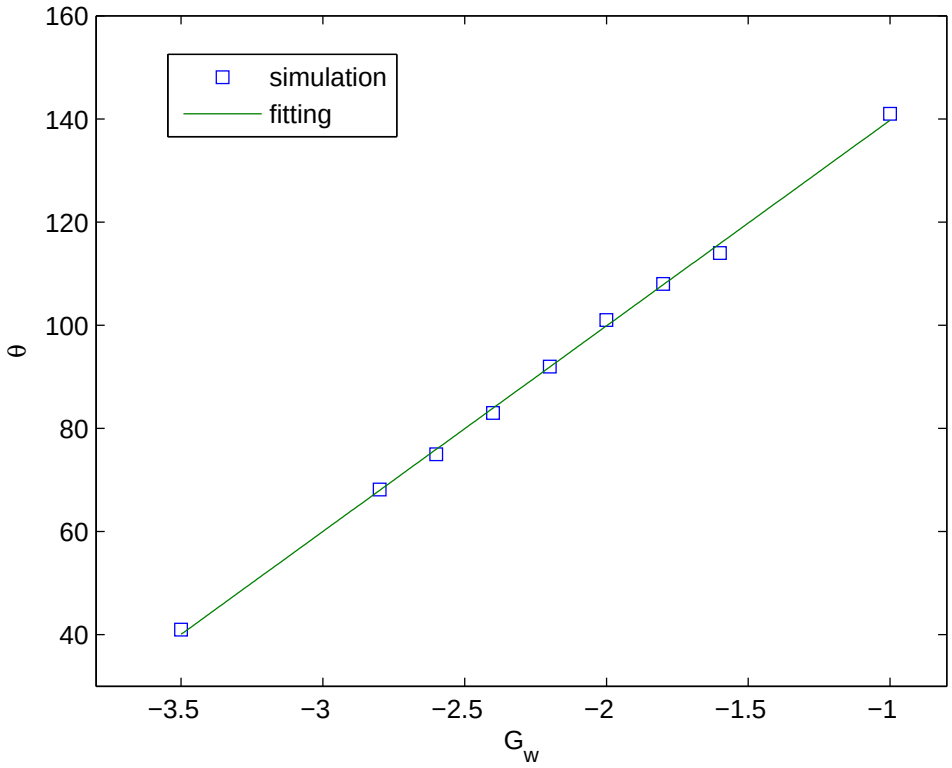

Figure 3.3: The relationship between G_w and contact angle θ.

and

$$\theta = arctan(\frac{b_0}{2(r - a_0)}). \tag{3.62}$$

The value of G_w is varied to obtain steady droplets with different contact angles. The relationship between G_w and the contact angle θ is shown in Fig. 3.3. It can be seen that the contact angles approximate to a linear function of G_w.

3.3.5 Conclusions

A three-dimensional multi-relaxation time (MRT) lattice Boltzmann model with an improved forcing scheme is reported for the simulation of high liquid-to-gas density ratio multiphase flows, based on the improved force scheme for the single relaxation time (SRT) pseudopotential LBM [60] and the Chapman-Enskog analysis [141]. The 3D MRT lattice Boltzmann model is validated through Laplace's law and by achieving thermodynamic consistency. Additionally, the relationship between the fluid-solid interaction potential parameter G_w and the contact angle is investigated. It has been observed that the contact angle is a linear function of G_w.

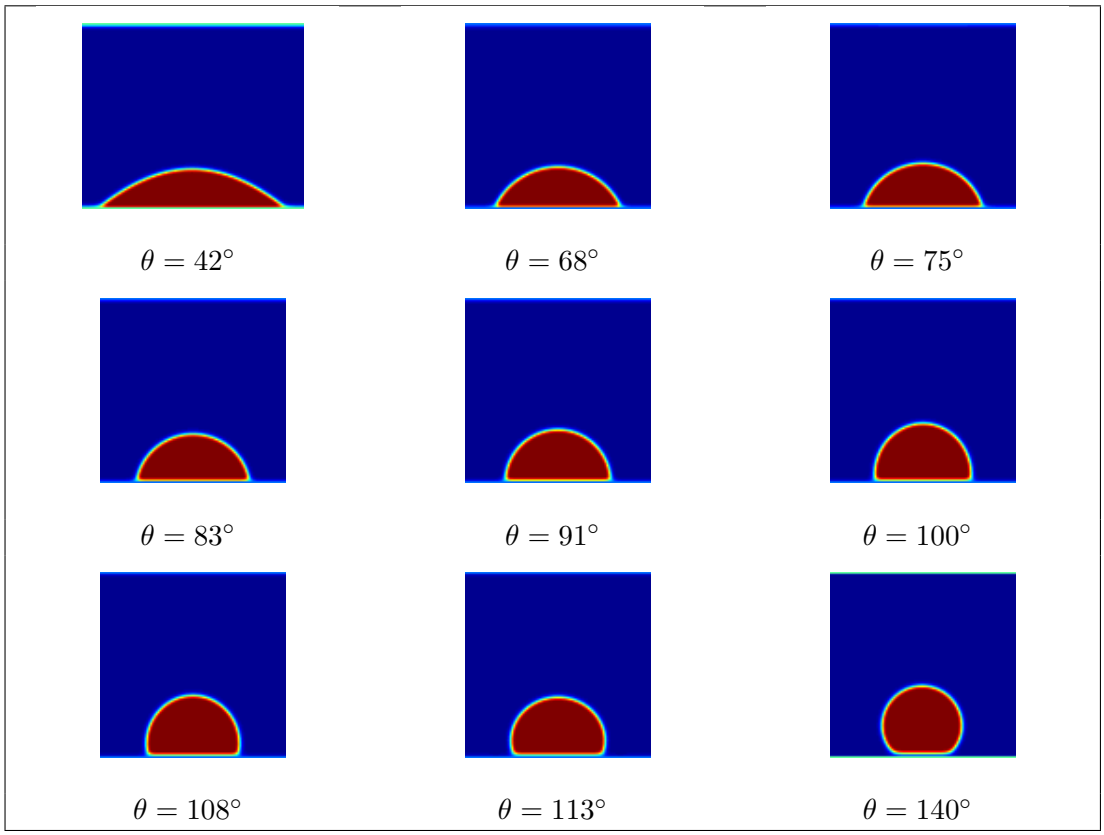

Figure 3.4: Computational cross-section snapshots with different contact angles.

Chapter 4

Droplet impingement on a solid surface

In chapter 4, lattice Boltzmann model is applied on the study of the impaction of a liquid droplet on a dry flat surface and a curved surface for a liquid-gas system with large density ratio. The influence of Reynolds number, Weber number, Ohnesorge number, Galilei number and surface characteristics on the impingement process is reported. The results are compared with experimental data reported in the literature.

4.1 Dynamics of droplet impingement on a flat surface

The improved three-dimensional MRT lattice Boltzmann model and the 3-dimensional lattice Boltzmann model based on the original Shan-Chen model [45] and the improvements in the single-component multiphase flow model reported by Yuan and Schaefer [17] is employed to study the impaction of a liquid droplet on a flat surface.

4.1.1 Initial and boundary conditions

The 3-dimensional computational domain used in the simulations is shown in Fig. 4.1. The domain size is 150*150*120 lattice nodes. Periodic boundary conditions are used on the sides of the domain. That means that the particles leaving the domain through a bounding face, will immediately re-enter the simulation region through the opposite face. No-slip wall boundary conditions are used on the top and bottom boundaries of the domain, while the half-way bounce-back scheme in LBM is applied on the wall boundary. The domain size for each case is varied according to the initial size of the droplet while the impact is assumed to be isothermal. By varying G_w, the wettability of the flat surface can be controlled. The liquid-gas density ratio is determined by T in eq. (3.13). In addition, the temperature T and other parameters (a,b) in eq. (3.13) control the interfacial surface tension between the two fluids. The acentric factor ω is set to be 0.344 in this simulation. Initially, the droplet is placed at the center of the computational domain and is equilibrated for 10000 lattice time steps to achieve the

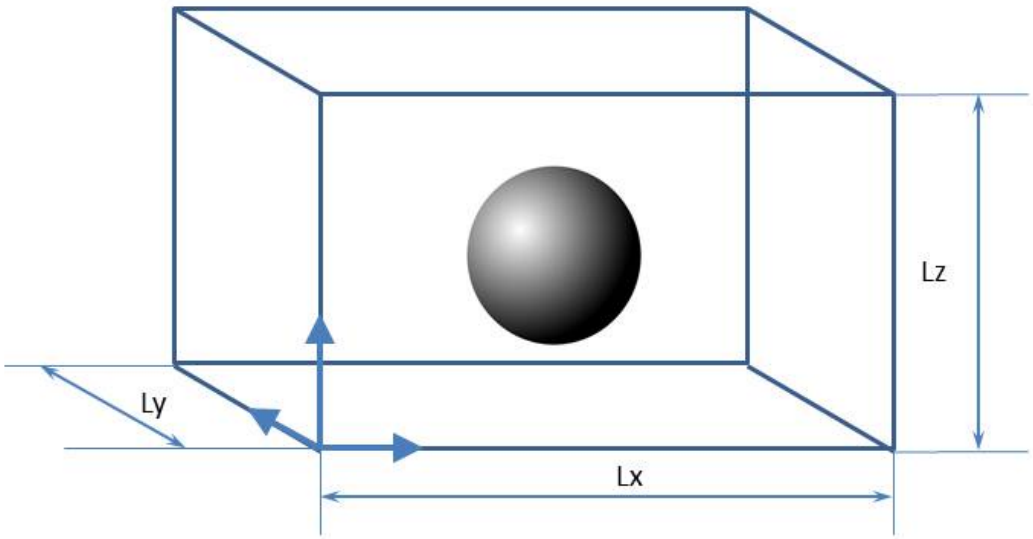

Figure 4.1: Computational domain for droplet impact on flat surface

correct pressure difference between inside and outside of droplet satisfying the Laplace law, after which it is allowed to move towards the flat surface with a uniform initial velocity $\boldsymbol{U_0}$. In order to obtain this initial velocity, an additional force is imposed at the first lattice time step, and then it is cut off. To systematically study the dynamics of a spreading droplet, three major non-dimensional parameters are usually employed, specifically the Weber number (We), Reynolds number (Re) and consequently Ohnesorge number (Oh) which have been defined in eq. 2.1∼2.3.

4.1.2 Spreading of the liquid droplet

The snapshots of the different stages of the impact of the liquid drop on the solid flat surface are presented in Fig. 4.9. The simulation parameters are We=52, Re=41, density ratio ρ_l/ρ_g=240, and equilibrium contact angle $\theta_{eq} = 96°$. The evolution time t is non-dimensionalized as $t^\star = tU_0/D_0$, where D_0 is the initial drop diameter and t is the time steps elapsed after the drop comes in contact with the flat surface. Immediately after the impact, the shape of the drop resembles a truncated sphere ($t^\star = 0.2125$). As the droplet impact progresses, a lamella is formed due to the inertial force ($t^\star = 0.4625$). The lamella continues to expand radially while its thickness decreases ($t^\star = 1.8375$). The lamella begins to retract due to gas-liquid interfacial surface tension ($t^\star = 3.3375$ and $t^\star = 6.3375$) after reaching its maximum spread. An equilibrium shape is reached after a couple of oscillations involving spread and recoil ($t^\star = 22.0875$). The time evolution of the spread factor, which is divided into four phases is shown in Fig. 4.3. The four phases include: the kinematic phase, the spreading phase, the relaxation phase

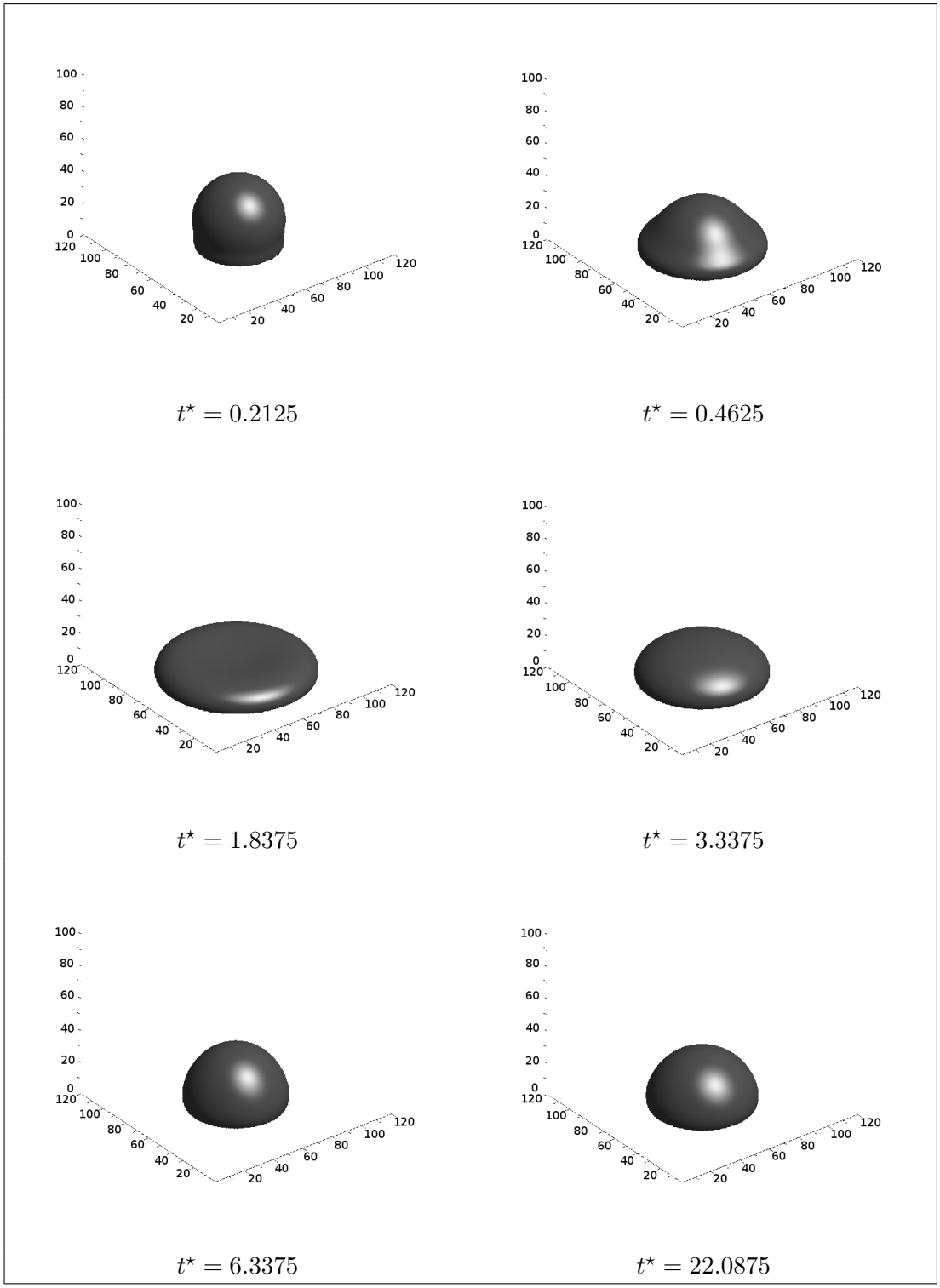

Figure 4.2: Computational snapshots of the droplet impact on a flat surface; $We = 52$, $Re = 41$, density ratio=240, contact angle=96°.

and the equilibrium phase [79].

It has been previously investigated through numerical analysis [96] and experimental

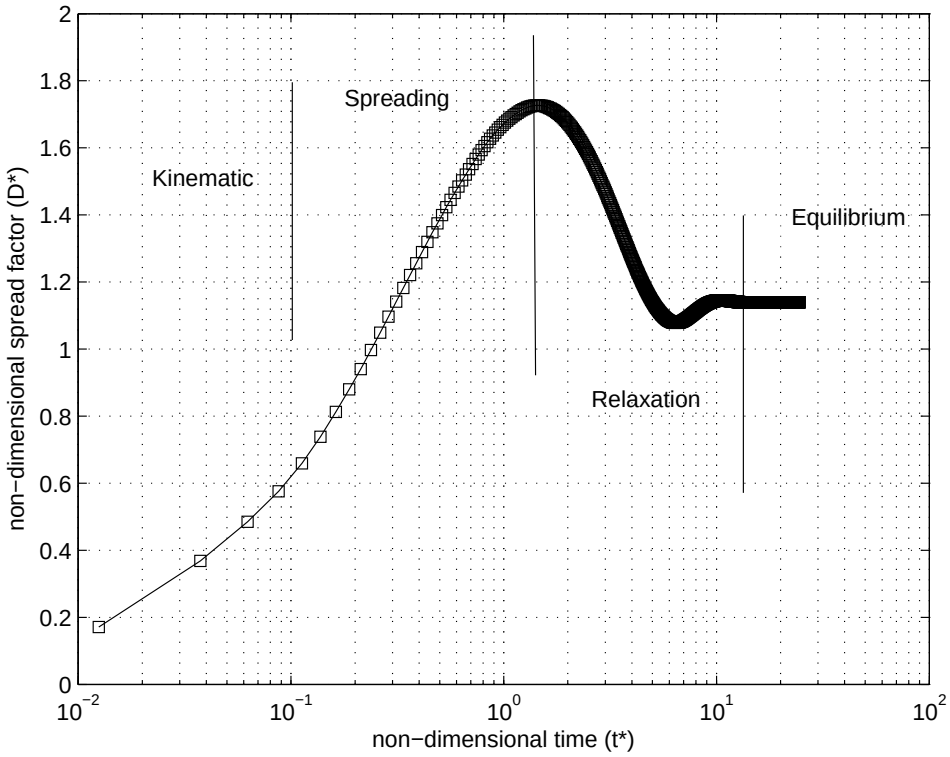

Figure 4.3: Time evolution of the spread factor from the current lattice Boltzmann model simulation.

Table 4.1: Simulation parameters.

Reynolds number	Weber number	Density ratio	Contact angle	a	b
27.72	10.86	240	90°	2/49	2/21
31.2	30.72	240	96°	0.5/49	3.5/21
41	52	240	96°	0.5/49	3.5/21
18.72	11.06	240	96°	0.5/49	3.5/21
54	104	114	104°	0.5/49	3.5/21
31.2	16	310	97°	1/49	2/21

work [79] that the spread factor is proportional to $\sqrt{t^\star}$ in the kinematic phase. The correlation factor is 2.8 from the experimental data by Rioboo et al. [79], while it equals to 1.35 in the work of Gupta and Kumar [96]. According to the theoretical analysis the correlation factor equals to 2. Fig. 4.4 shows the time evolution of the spread factor $D^\star$ in the kinematic phase ($t^\star << 1$) for six different We and Re cases using the current LBM model. The Weber number, Reynolds number, density ratio and wettability of the surface for these six cases are illustrated in table. 4.1. A fitting curve has been generated to yield $D^\star = 2\sqrt{t^\star}$ which is the same as the theoretical result. It can be

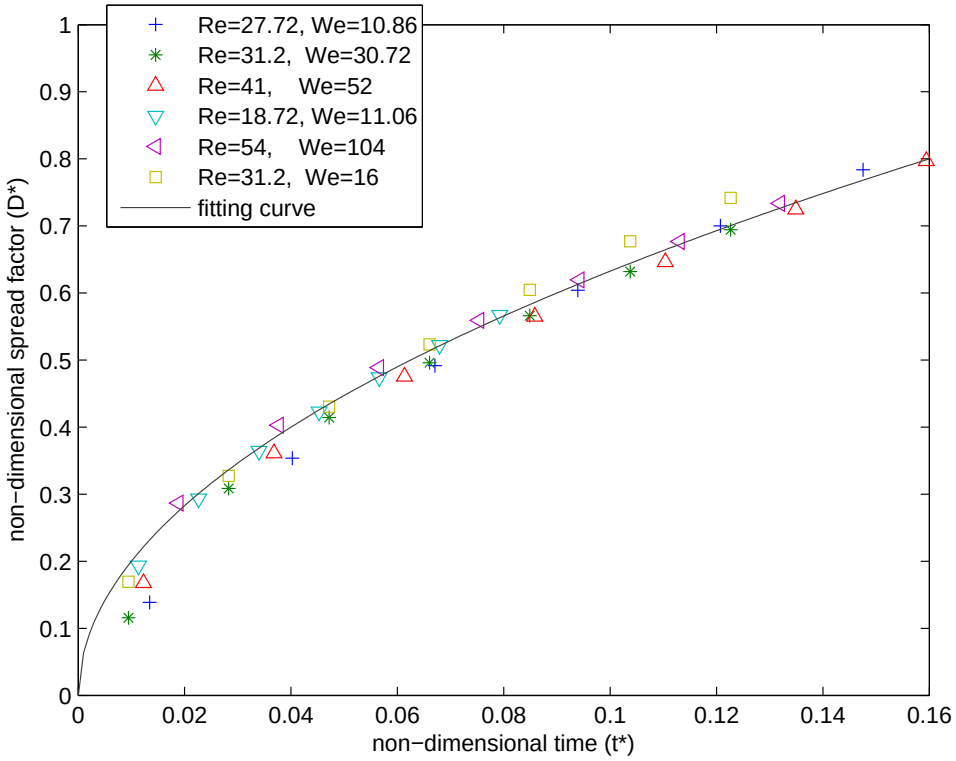

Figure 4.4: Time evolution of the spread factor in the kinematic phase from current LBM simulation for six cases

observed from Fig. 4.4 that all cases behave similarly during the kinematic phase. Therefore, the droplet spread factor in the kinematic phase is independent of the the physical properties of the fluids and the wettability of the surface, while it is only a function of the dimensionless time.

The maximum spread factor is obtained at the end of the spreading phase, which follows the kinematic phase. It depends on the capillary force, viscosity and inertial effects as well as the contact angle. Asai et al. [80] proposed a correlation for the maximum spread factor which is given by

$$D^{\star}_{max} = 1 + 0.48We^{0.5}exp[-1.48We^{0.22}Re^{-0.21}]. \tag{4.1}$$

Another maximum spread factor prediction equation was derived based on the energy conservation equation and the viscous dissipation based on the linear velocity profile [82]

$$\frac{3}{2}\frac{We}{Re}{D^{\star}_{max}}^{4} + (1 - cos\theta){D^{\star}_{max}}^{2} - (\frac{We}{3} + 4) = 0. \tag{4.2}$$

The maximum spread factor prediction equation from Pasandideh-Fard et al. [83] is also based on energy conservation equation, while the viscous dissipation was based on

the velocity profile of stagnation-point flow.

$$D^{\star}_{max} = \sqrt{(We + 12)/[3(1 - cos\theta) + 4We/\sqrt{Re}]}. \tag{4.3}$$

In order to cover a large range of We and Oh numbers, Mao et al. [84] proposed an empirical equation based on the energy conservation equation

$$[0.2Oh^{0.33}We^{0.665} + \frac{1}{4}(1 - cos\theta)]{D^{\star}_{max}}^{2} + \frac{2}{3}{D^{\star}_{max}}^{-1} = \frac{We}{12} + 1. \tag{4.4}$$

Scheller and Bousfield [81] generated a experimental equation to predict $D^{\star}_{max}$ given by

$$D^{\star}_{max} = 0.61(Re^2Oh)^{0.166}. \tag{4.5}$$

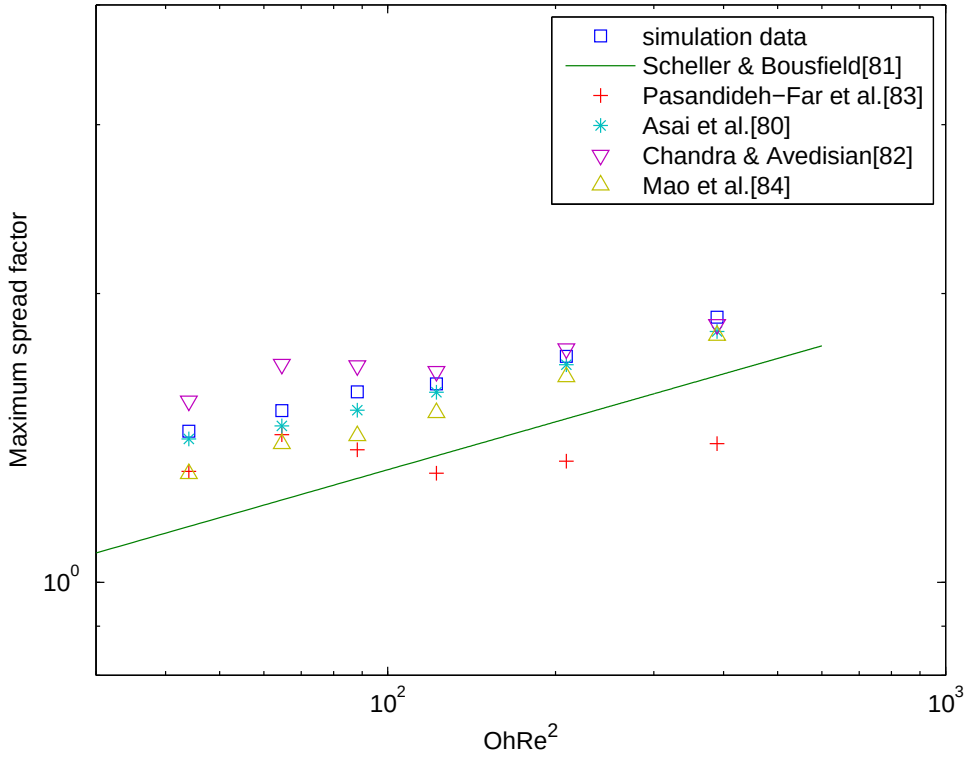

Figure 4.5: Comparison of the maximum spread factor predicted by the lattice Boltzmann model and various equations published in the literature.

Although the effect of the equilibrium contact angle was neglected, the empirical equation was in good agreement with Dong et al.'s [86] experiment. The maximum spread factor predicted from our simulation results is compared with previous studies [80–84] in Fig. 4.5. It can be observed that the simulation results are in good agreement with the predictions from the equations of Asai et al. [80] and Mao et al. [84]. A good correlation with the results of Chandra and Avedisians' [82] is also observed, especially at higher $OhRe^2$ numbers, while minor deviations are present at lower $OhRe^2$

numbers. Discrepancies can be seen between the numerical results and the predictions from Pasandideh-Fard et al. [83], while the correlation of Scheller and Bousfield significantly under predicts $D^{\star}_{max}$ especially for low $OhRe^2$ numbers. These discrepancies can mainly be attributed to the fact that Pasandideh-Fard et al's. [83] evaluation of dissipation is suitable for low Oh numbers, while Chandra and Avedisian' [82] dissipation evaluation becomes more suitable for high Oh numbers. This has also been pointed out in the work of Mao et al. [84].

Simulations were conducted for a range of Weber and Reynolds numbers in this

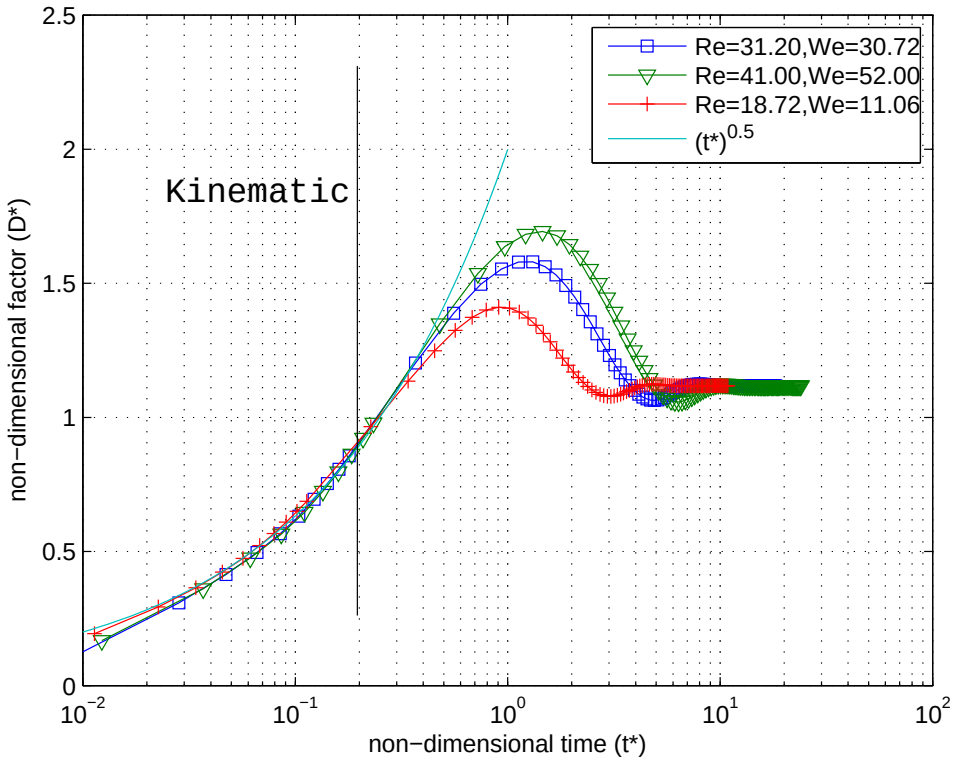

Figure 4.6: Time evolution of the spread factor for $Oh = 0.177$.

study, while keeping the density ratio between liquid and gas, the wettability of the surface and the Ohnesorge number (Oh) constant as 240, 96°, and 0.177, respectively. In Fig. 4.6, the time evolution of the droplet spreading process on a dry flat surface for Oh=0.177 is shown. It can be seen that in the kinematic phase, $D^{\star}$ is proportional to $\sqrt{t^{\star}}$ for all Reynolds numbers. The spreading phase depends on the Weber and Reynolds numbers, which control both the maximum diameter and the time to achieve it. Increasing the inertial force leads to an increase in the maximum spread factor. For the lowest Reynolds number of 18.72, the maximum spread factor is 1.43, while the maximum value is 1.72 when the Reynolds number is 41. Another observation from Fig. 4.6 is that longer times are needed for the droplets to reach the peak diameter

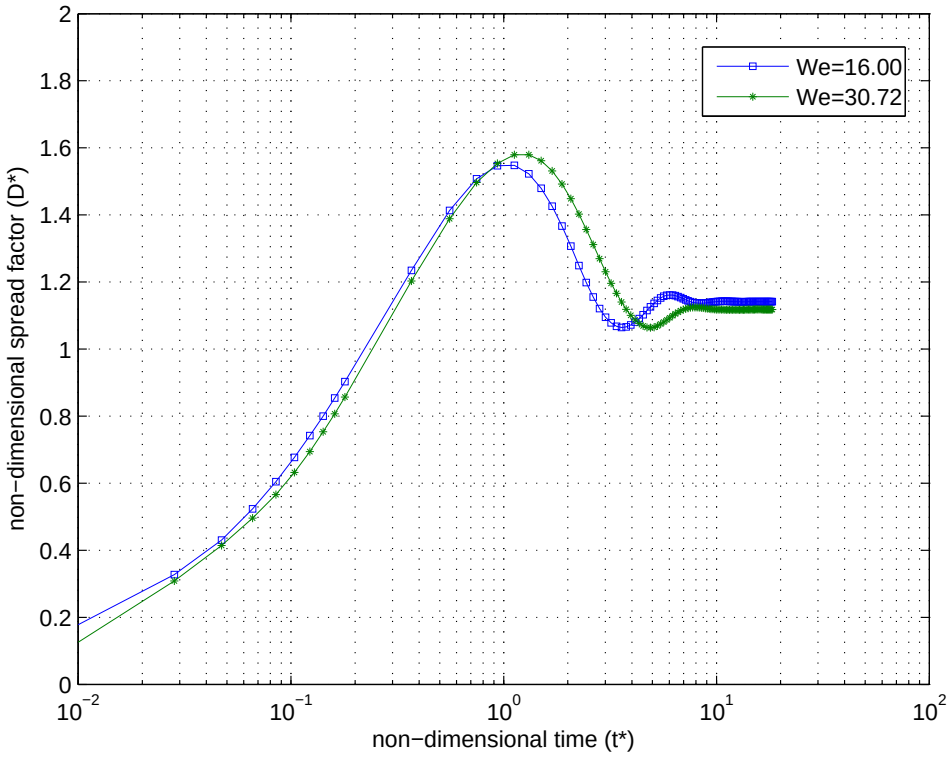

Figure 4.7: Time evolution of the spread factor for $Re = 31.2$ and $\theta_w = 96°$.

and the equilibrium shape as the Weber number and Reynolds number increase. The influence of the surface tension on the spreading process is estimated by varying the Weber number while keeping the Reynolds number and equilibrium contact angle at a constant value of 31.2 and 96°, respectively. From Fig. 4.7, the maximum spread factor is 1.61 at We=30.72 and the maximum value is 1.58 when We=16. Hence, the influence of surface tension on the maximum spread factor is weak and the maximum spread factor mainly depends on the Reynolds number. The effect of the wettability of the flat surface on the spread factor is plotted in Fig. 4.8. Three different surfaces have been used: hydrophilic, neutral, and hydrophobic with static contact angles of $\theta = 76°$, $\theta = 91°$, $\theta = 104°$, respectively. It can be seen that the influence of θ becomes significant during the relaxation phase. For $\theta = 104°$, secondary spreading and oscillation are observed, but not for the case where $\theta = 76°$. The recoil speed is slower for low θ, and as θ decreases, the equilibrium spread factor and maximum spread factor increase.

4.1.3 Spreading of the liquid droplet with new forcing scheme

The improved three-dimensional MRT lattice Boltzmann model is employed in the simulation of the impingement of a liquid droplet onto a flat surface for a range of

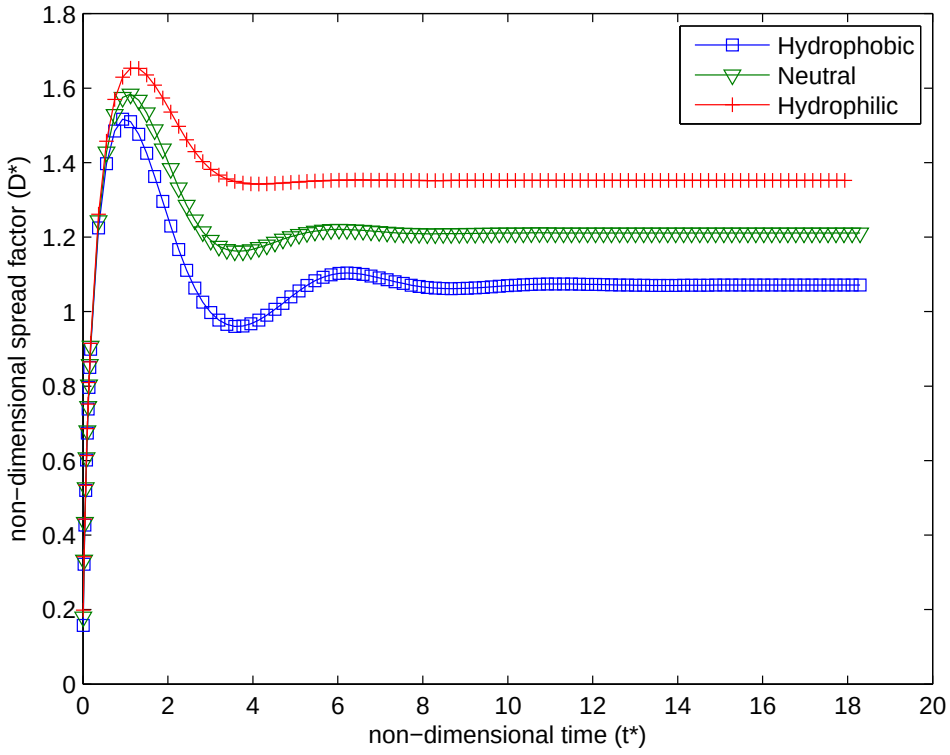

Figure 4.8: Influence of wettability on the spreading behavior. (Re = 31.2, We = 16, density ratio is 313.

Weber and Reynolds numbers. The snapshots of the stages of the liquid drop impact on the solid flat surface are presented in Fig. 4.9 for We=19.34, Re=92.4, density ratio ρ_l/ρ_g=412, and equilibrium contact angle $\theta_{eq} = 89°$. The evolution time t is non-dimensionalized as $t^\star = tU_0/D_0$, where D_0 is the initial drop diameter and t is the time elapsed after the drop comes in contact with the flat surface. Immediately after the impact, the shape of the drop resembles a truncated sphere ($t^\star$=0.167). As the liquid drop continues to move downwards, a lamella is formed ($t^\star$=0.573). The lamella continues to grow radially while its thickness decreases ($t^\star$=1.157) until the surface tension dominates the inertial force. The lamella begins to retract due to interfacial tension after reaching a maximum spread factor ($t^\star$=1.67, $t^\star$=2.028, $t^\star$=2.625). Then, an equilibrium shape is reached ($t^\star$=23.83) after a couple of oscillations involving spread and recoil ($t^\star$=4.295, $t^\star$=7.159). The time evolution of the spread factor which is divided into four phases is provided in Fig. 4.10. The spread factor is defined as the ratio of the spreading diameter on the surface and the initial droplet diameter, $D^\star = D/D_0$. The four phases include: the kinematic phase, the spreading phase, the relaxation phase and the equilibrium phase [79].

The maximum spread factor is reached at the end of the spreading phase which fol-

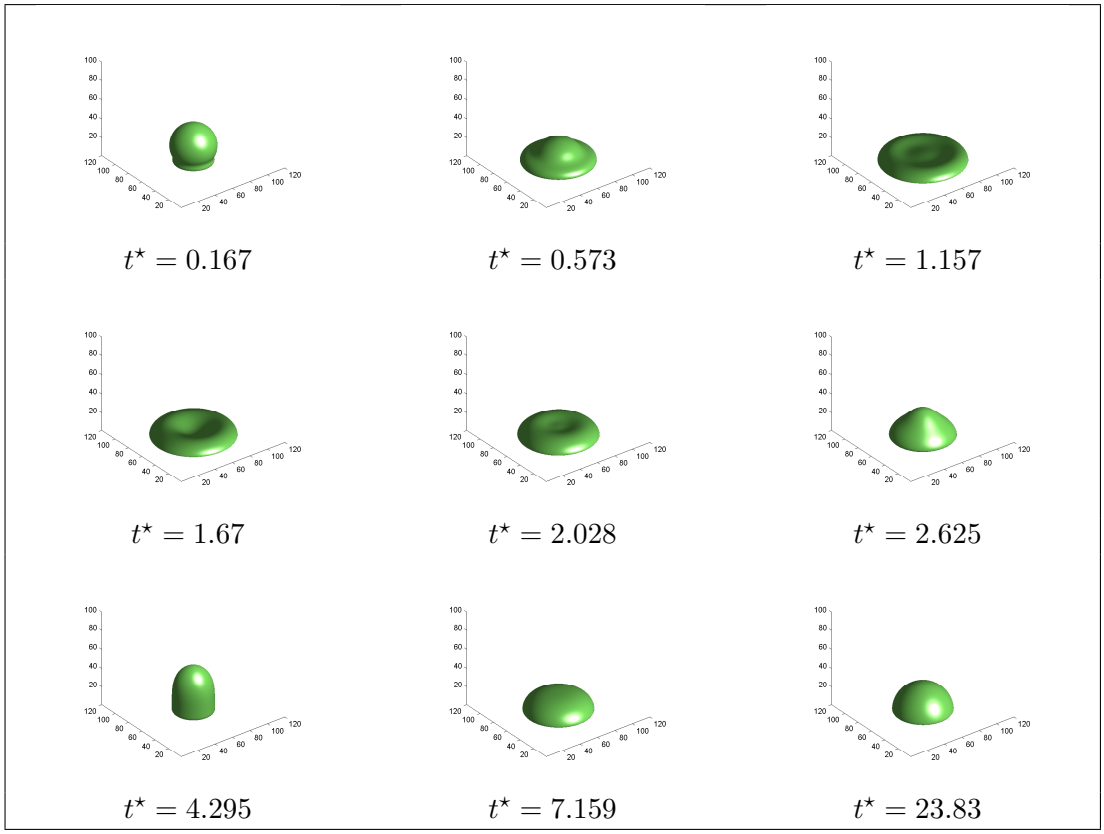

Figure 4.9: Computational snapshots of droplet impact on flat surface; We=19.34, Re=92.4, density ratio=412, contact angle=89°.

case	Reynolds number	Weber number	density ratio	contact angle
data1	27.72	10.86	412	89°
data2	31.2	16	412	96°
data3	92.4	19.34	412	89°
data4	168.75	26.90	716	89°
data5	229.95	36.49	716	89°
data6	18.72	11.06	412	96°

Table 4.2: Simulation parameters for new forcing scheme.

lows the kinematic phase. It is dependent on the capillary force, viscosity and inertial effects as well as the contact angle. [80] proposed a correlation which was given as $D^\star_{max} = 1 + 0.48We^{0.5}exp[-1.48We^{0.22}Re^{-0.21}]$. Another maximum spread factor prediction equation was produced as $D^\star_{max} = ((We + 12)/[3(1 - cos\theta) + 4We/\sqrt{Re}])^{0.5}$ based on the energy conservation equation in Pasandideh-Fard et al.'s study [83]. Scheller and Bousfield [81] derived an experimental equation to predict $D^\star_{max}$ given by $D^\star_{max} = 0.61(Re^2Oh)^{0.166}$. Although the effect of the equilibrium contact angle had been neglected, the empirical equation gives a good fit with Dong et al.'s [86] experiment. In order to validate the current 3D MRT LBM model, the maximum spread

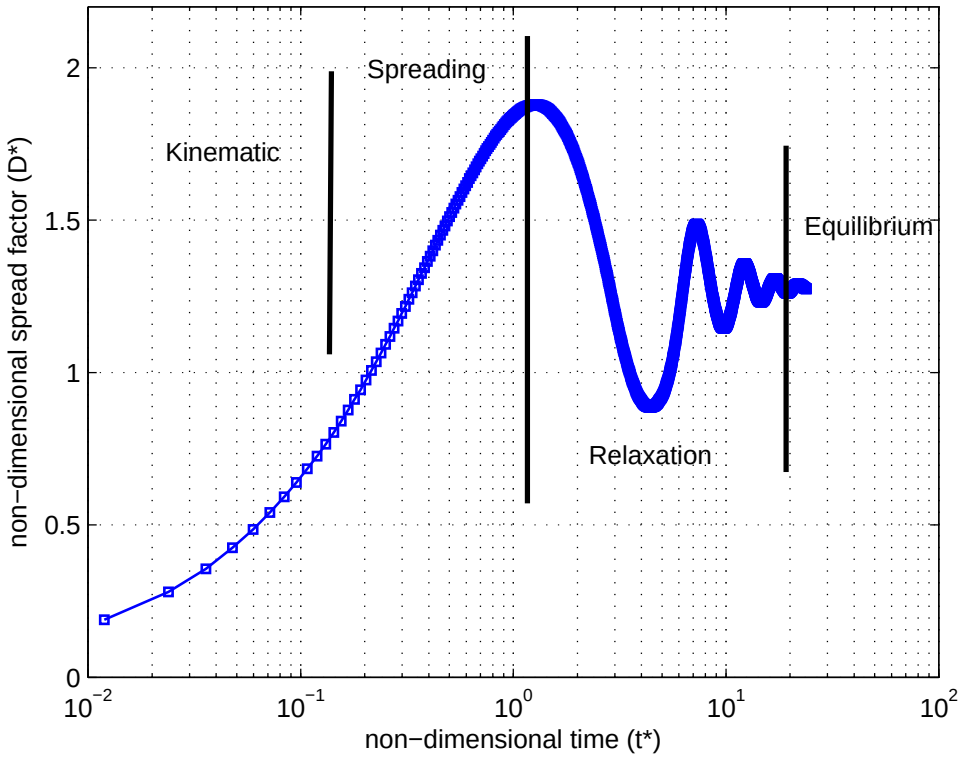

Figure 4.10: Time evolution of the spread factor from improved 3D MRT LBM simulation.

factor for randomly chosen We and Re cases from the current LBM model are compared with the predictions from previous studies published in the literature [80, 81, 83](Fig. 4.11). The Weber number, Reynolds number, density ratio and surface wettability for these six cases are given in table. 5.1. The simulation results are in good agreement with the predictions of the equations from [80], [83] and [81].

The effect of the wettability of the flat surface on the spread factor is shown in Fig. 4.12. Three different surfaces have been used: hydrophilic, neutral, and hydrophobic with static contact angles of $\theta = 76°$, $\theta = 89°$, $\theta = 106°$, respectively. It can be seen that the influence of the contact angle θ becomes significant during the relaxation phase. For $\theta = 106°$, the oscillation is more intense than for the case of $\theta = 76°$. Longer time is required to achieve the equilibrium state for the case of hydrophobic surface. As θ decreases, the equilibrium spread factor and maximum spread factor increase.

4.1.4 Conclusions

The liquid droplet impact on a flat surface has been simulated by a 3-dimensional lattice Boltzmann model which can tolerate high density ratios. It has been shown that there

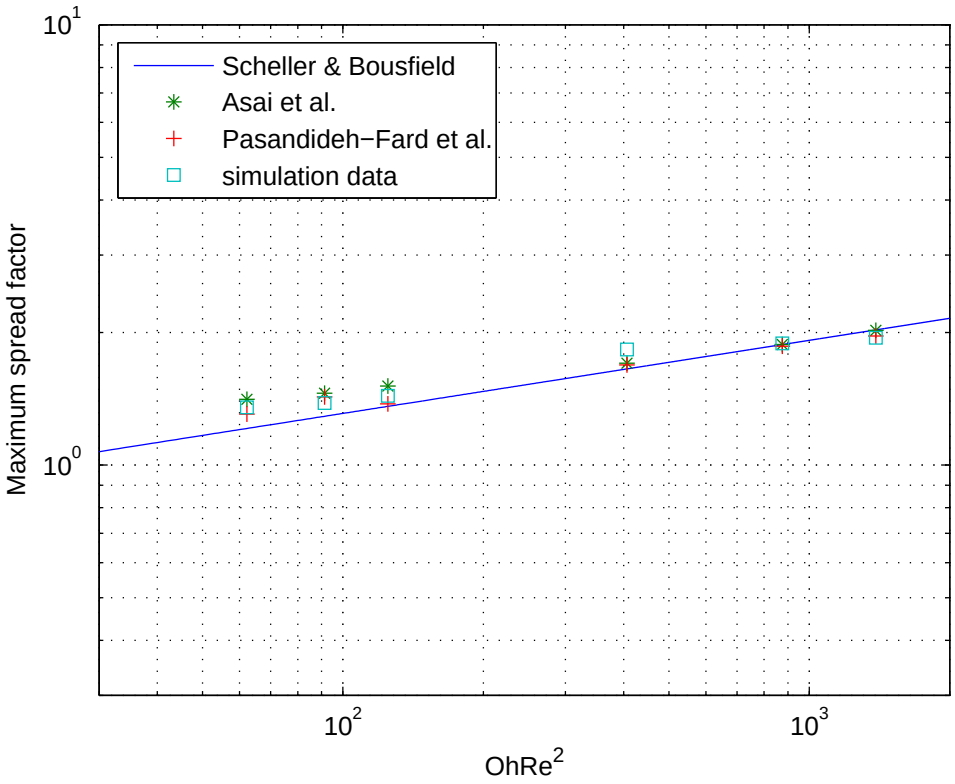

Figure 4.11: Maximum spread factor comparison with LBM simulation results and prediction equation.

are four phases during the droplet impact on flat surface which include: the kinematic phase, the spreading phase, the relaxation phase and the equilibrium phase. In the kinematic phase, the droplet spread factor does not depend on the physical properties of the fluids and surface wettability, and it is only a function of the non-dimensional time ($D^\star = 2\sqrt{t^\star}$). In the spreading phase, it is shown that increasing the inertia leads to an increase in the maximum spread factor.

For given Oh, it can be seen that inertia controls the maximum diameter as well as the time needed to reach the peak diameter in the spreading phase. Longer times are needed to reach the equilibrium shape for high Weber and Reynolds numbers. It is also found that the influence of surface tension on the maximum spread factor is weak, while the influence of the wettability of the surface becomes significant during the relaxation phase. The secondary spread and oscillation appear for higher θ, while they are absent for low θ under the same Reynolds and Weber numbers. As the contact angle decreases, the equilibrium spread factor and maximum spread factor increase, while the recoil speed becomes slower.

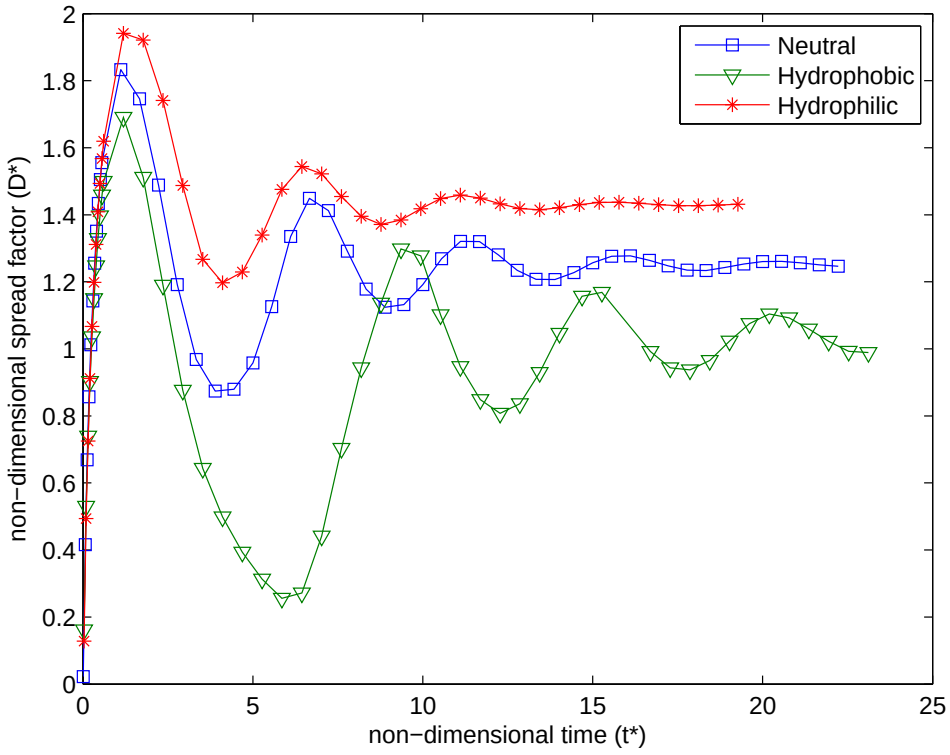

Figure 4.12: Wettability influence on the spreading behavior.(Re=92.4, We=19.34, density ratio is 412).

4.2 Dynamics of droplet impingement on a cylindrical surface

In order to overcome the limitations of low density ratio and instability with a relaxation time τ less than 1, a two-dimensional multi-relaxation-time interaction-potential-based lattice Boltzmann model based on the improved forcing scheme which was reported by Li et al. [60] and Peng-Robinson (P-R) equation of state [17] is proposed in this thesis. The impaction of liquid droplet on a cylindrical surface for the liquid-gas system with large density ratio and low kinematic viscosity of the fluid is simulated. The effect of the Reynolds number, Weber number, Galilei number and surface characteristics on the dynamic behavior of droplet and film flow dynamics on the target surface are investigated.

4.2.1 Initial and boundary condition

A two-dimensional computational domain for simulation of droplet impact onto the cylindrical surface from 90° with horizon is shown in Fig. 4.13. Non-slip wall boundary condition is used on the solid surface and periodic boundary condition is used on all

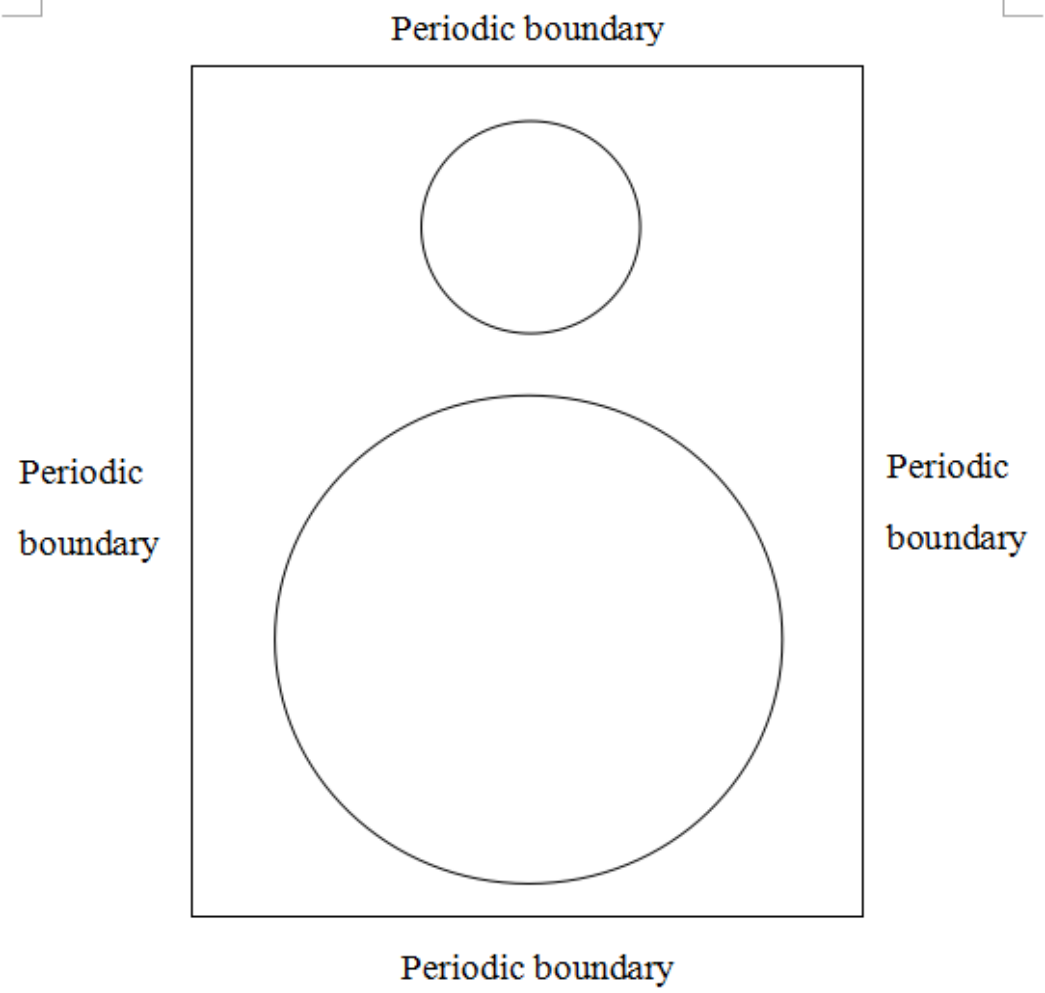

Figure 4.13: The initial and boundary conditions in domain.

sides of the domain. Initially, the droplet is located several nodes away from the tube and then directed towards the tube with initial velocity U_0 after 50000 lattice time steps.

4.2.2 Dynamics of the film flow on the cylindrical surface

Fig. 4.14 shows a sequence view of the impact of the droplet onto cylindrical surface with Re=113.1, We=12.51, Bond number B_0=1.2, density ratio ρ_l/ρ_g=580 and equilibrium contact angle $\theta = 60°$. The Bond number is defined as $B_0 = \rho_l g D_0/\sigma$. The evolution time t is non-dimensionalized as $t^\star = tU_0/D_0$, where D_0 is the initial drop diameter, U_0 is the initial velocity and t is the time steps elapsed after the drop contacts the surface. From this figure, the formation of the liquid lamella around the surface of

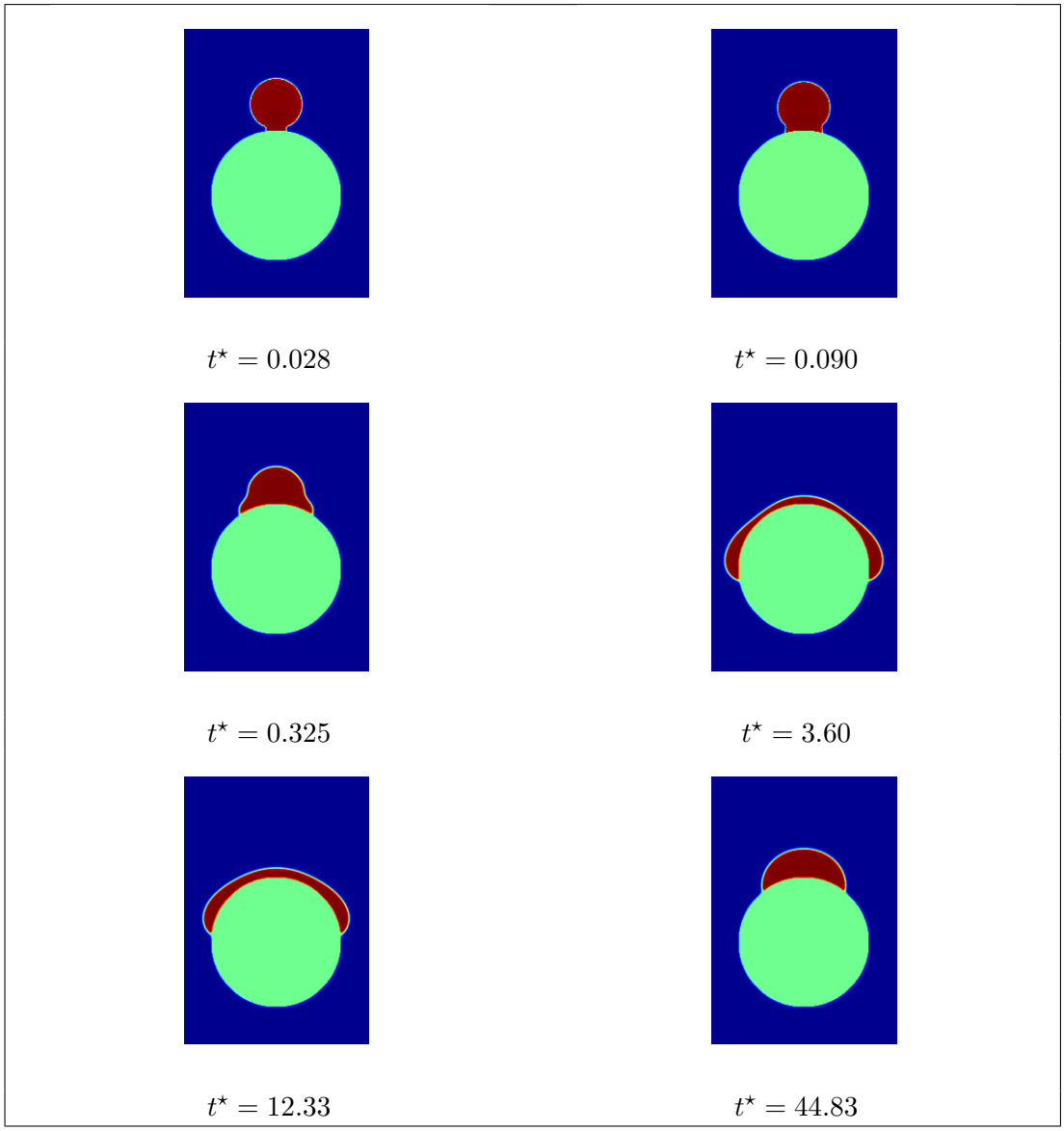

Figure 4.14: Computational snapshots of droplet impact on tube; We=12.51, Re=113.1, density ratio=580, contact angle=60°.

the target is clearly observed. At the beginning, the initial droplet deformation period is observed. The upper portion of the droplet remains spherical under the action of surface tension and moves with the impact velocity of the drop ($t^\star = 0.028$ and $t^\star = 0.090$). Then the liquid lamella appears around the surface of the tube with the liquid continuing to flow downwards and the thickness of film at the pole of tube decreasing gradually in this phase ($t^\star = 0.325$ and $t^\star = 3.60$). Finally, during phase 3, the lamella begins to retract governed by the surface tension and almost reaches a residual value ($t^\star = 12.33$ and $t^\star = 44.83$) after a couple of oscillations. The corresponding temporal variation of the film thickness at the cylindrical surface is shown in Fig. 4.15

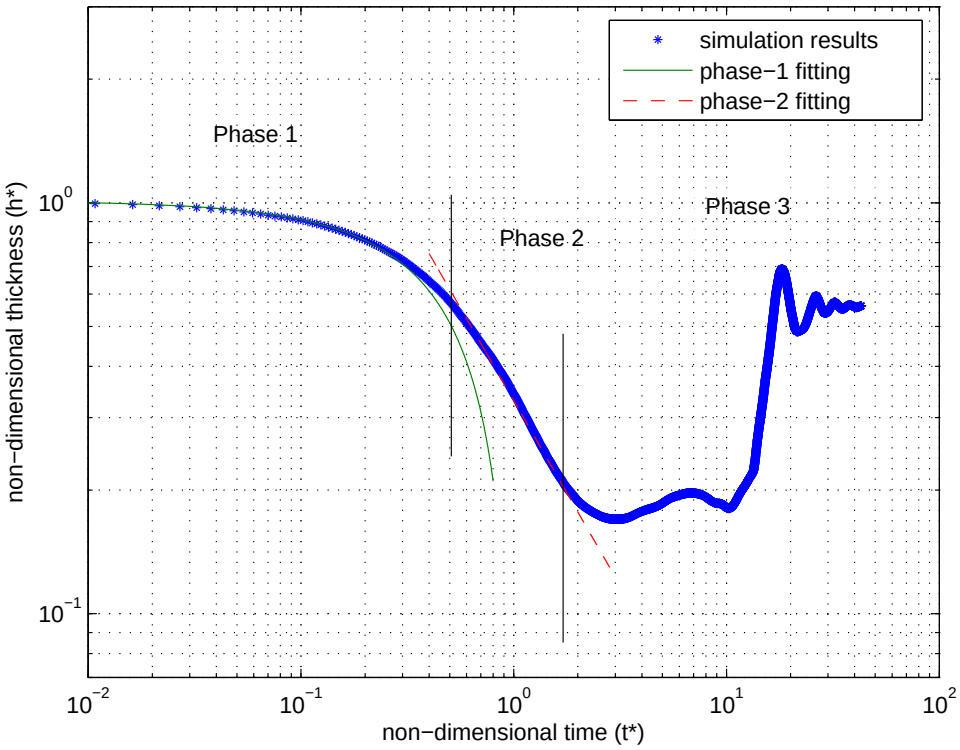

Figure 4.15: Time evolution of film thickness at the north pole of the tube; We=12.51, Re=113.1, density ratio=580, contact angle=60°.

with log-log axes. The film thickness is nondimensionalized with the initial impacting droplet diameter as $h^\star = h/D_0$. Three distinct temporal phases of the film dynamics can be clearly observed from this figure. The first phase is the droplet deformation period in which the free surface of the deforming drop is negligibly influenced by the presence of the target. Hence, the upper part of the droplet continues to move at the impacting velocity resulting in the non-dimensional film thickness and time satisfy the equation $h^\star = 1 - t^\star$. In the second phase, inertial forces dominate the viscous forces and surface tension, thus the temporal variation is given by the equation which yield $h^\star = 0.33/(t^\star)^{0.9}$. There are diffent dynamic behavior for the first and second phase reflecting from the different format for the equations describing the temporal viariation of film thickness in first phase and second phase. In phase 3, the film thickness increases under the action of surface tension and approaches a constant value due to the balance of surface tension, viscous forces and gravity.

Simulations are performed for different values of droplet Reynolds number with the same target-to-drop size ratio, wettability and kinematic viscosity to evaluate the effect of Reynolds number on the dynamics of the film flow on the cylindrical surface. Some new investigations are found comparing with the investigation from experimental

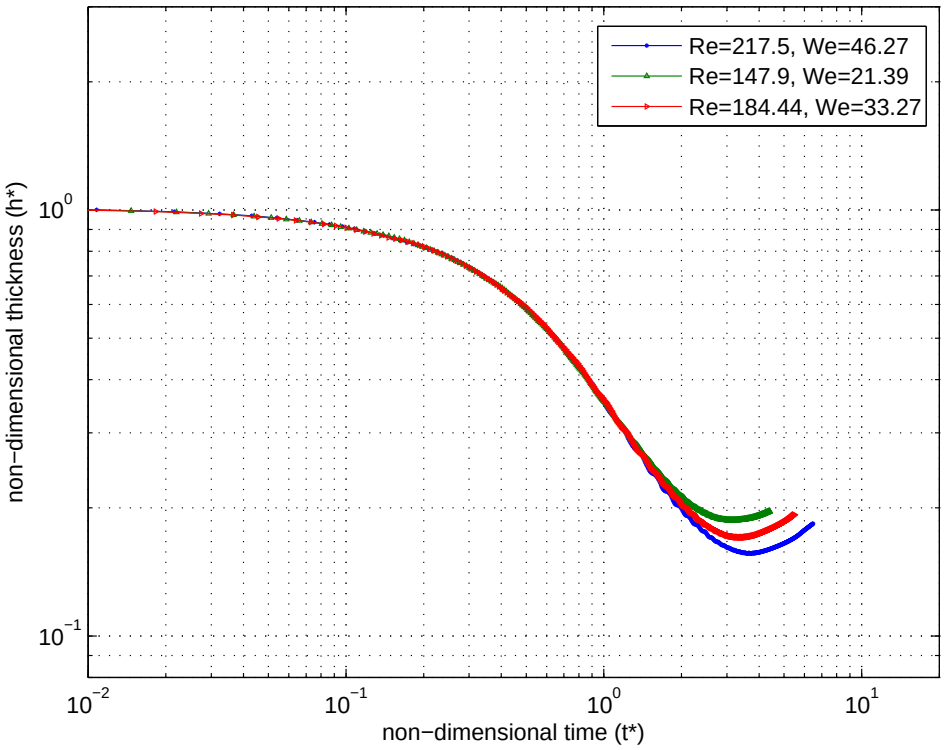

Figure 4.16: Temporal variation of film thickness at the north pole of the tube for different Reynolds number and Weber number with same kinematic viscosity; τ_ν=0.6, contact angle=60°.

research of Bakshi et al. [89]. In order to avoid the effect of gravity, the gravity force is not included into this case. The influence of gravity on film flow dynamics will be discussed in the next paragraph. In the experimental research of Bakshi et al. [89], it has been observed that the non-dimensional temporal variation of film thickness for different values of Reynolds number collapses onto a single curve in the first and second phases. However, the Reynolds number is varied by changing the impact velocity with same kinematic viscosity value in that study. The Weber number is also varied during this process and both of the change of the Reynolds and Weber number affect this process. A different behaviour might be observed when only the Reynolds number is varied, while the Weber number is invariable. In order to verify this assumption, a numerical investigation is conducted as follows. Firstly, the Reynolds number is varied by changing the impact velocity, while the kinematic viscosity is kept constant. The kinematic viscosity can be controlled by Eq. (3.32) and the τ_ν is given by 0.6 for different Reynolds number. The contact angle of surface is given as 60° which corresponds to $G_w = 2.9$. Fig. 4.16 shows the time evolution of the film thickness at the cylindrical surface for different Reynolds numbers. Fig. 4.16 shows that the non-dimensional

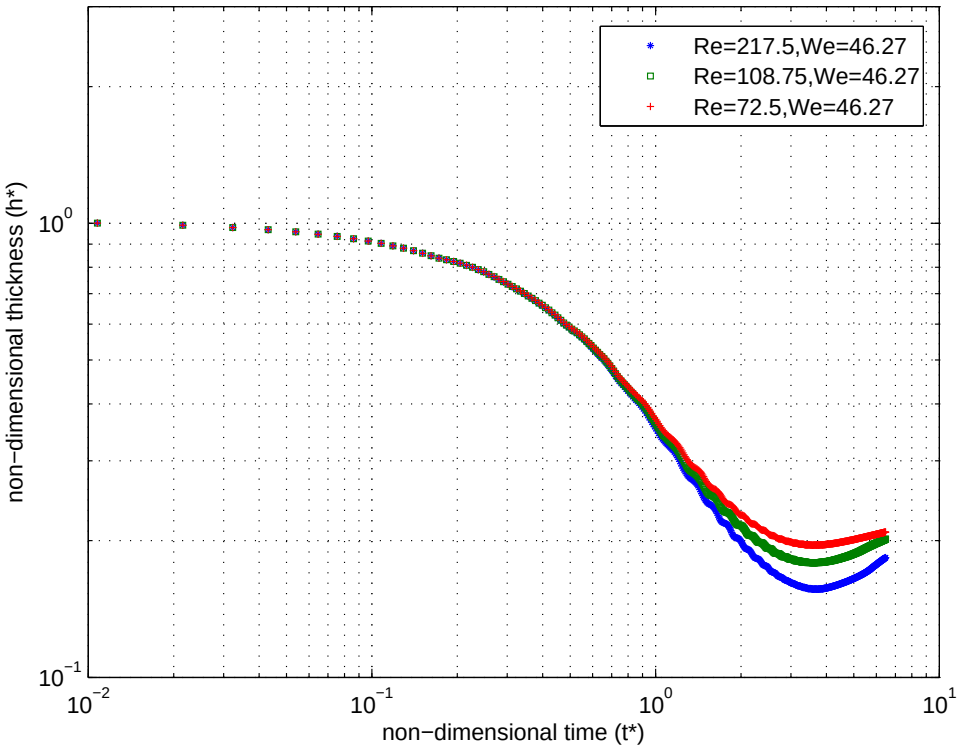

Figure 4.17: Temporal variation of film thickness at the north pole of the tube for different Reynolds number and Weber number with different kinematic viscosity; contact angle=60°.

temporal variation of film thickness for different values of Reynolds number collapses onto a single curve in the first and second phases, but the transition to the third phase occurs earlier for the low Reynolds number case. In addition, the film thickness in the third phase reduces with increasing Reynolds number. All of the above observations are in line with the experimental results by Bakshi et al. [89]. However, different phenomena can be observed for the case that different Reynolds numbers are obtained by changing the kinematic viscosity. The effect of different kinematic viscosity of fluids on the dynamics of film flow is investigated. Fig. 4.17 shows the time evolution of the film thickness at the cylindrical surface for different Reynolds numbers through adjusting the kinematic viscosity. It can be observed that the thickness in the third phase still decreases with increasing Reynolds number. However, it does not collapse onto a single curve in the second phase for the different Reynolds number cases. The rate of film thickness decrease becomes slower with increasing kinematic viscosity. This shows that the influence of the viscous force in the second phase can not be neglected for the low Reynolds number case. By comparing with the Reynolds number and Weber number used in Bakshi et al.'s [89] experimental work, the Reynolds number and Weber num-

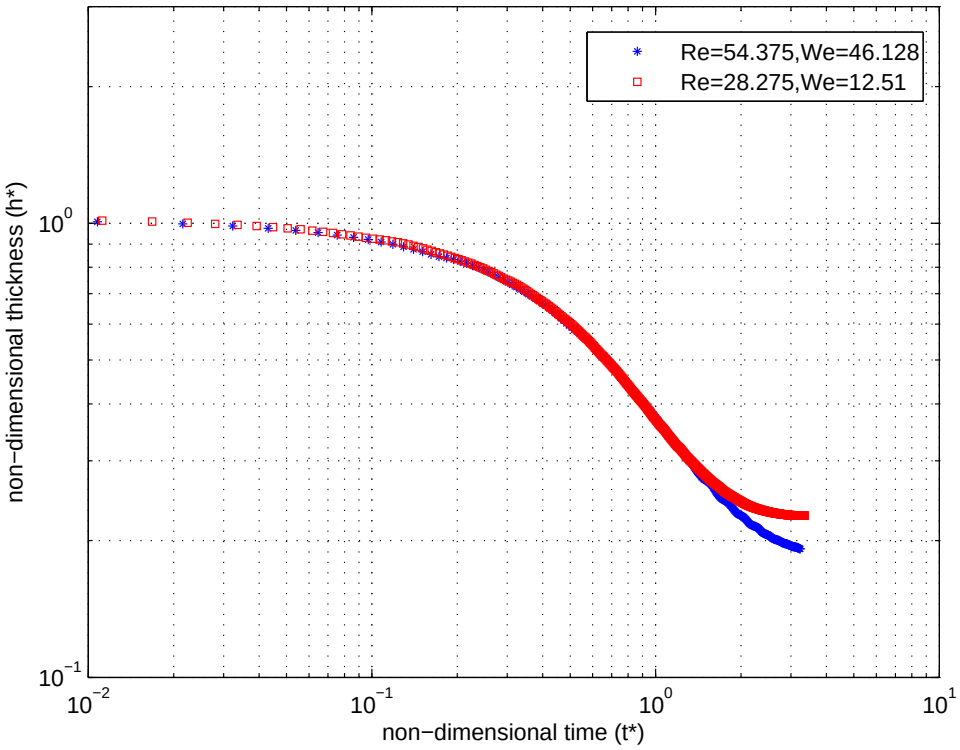

Figure 4.18: Temporal variation of film thickness at the north pole of the tube for different Reynolds number and Weber number with Ga=219.5, B_0=3.42, contact angle=60°.

ber in current numerical work is low. Thus, we call the Reynolds number and Weber number in the present work as low Reynolds number and low Weber number. Actually, even for the high Reynolds number case, the influence of the viscous force will appear at the latter part of the second phase with the inertial force decreasing.

In the experimental study of Bakshi et al. [89], the effect of Reynolds number and target-to-drop size ratio on the dynamics of film flow is investigated. In the current simulation study, the influence of gravity and surface tension is investigated as well. Four simulations divided into two groups with different Galiler number are conducted to evaluate the effect of gravity on the temporal variatio nof film thickness. The time evolution of the film thickness at the cylindrical surface with different Reynolds numbers at Galilei number 219.5 is shown in Fig. 4.18. The Galilei number is defined as $Ga = gD_0^3/\nu^2$. It is clear from Fig. 4.18 that the temporal variation of film thickness for different values of Reynolds number collapses onto a single curve in the first and second phases, which shows that the influence of gravity can be neglected in the first and second phases. However, decreasing the kinematic viscosity which corresponds to an increase in the Galilei number results in a different phenomenon. Fig. 4.19 shows the temporal variation of the film thickness for different Reynolds number at Galilei num-

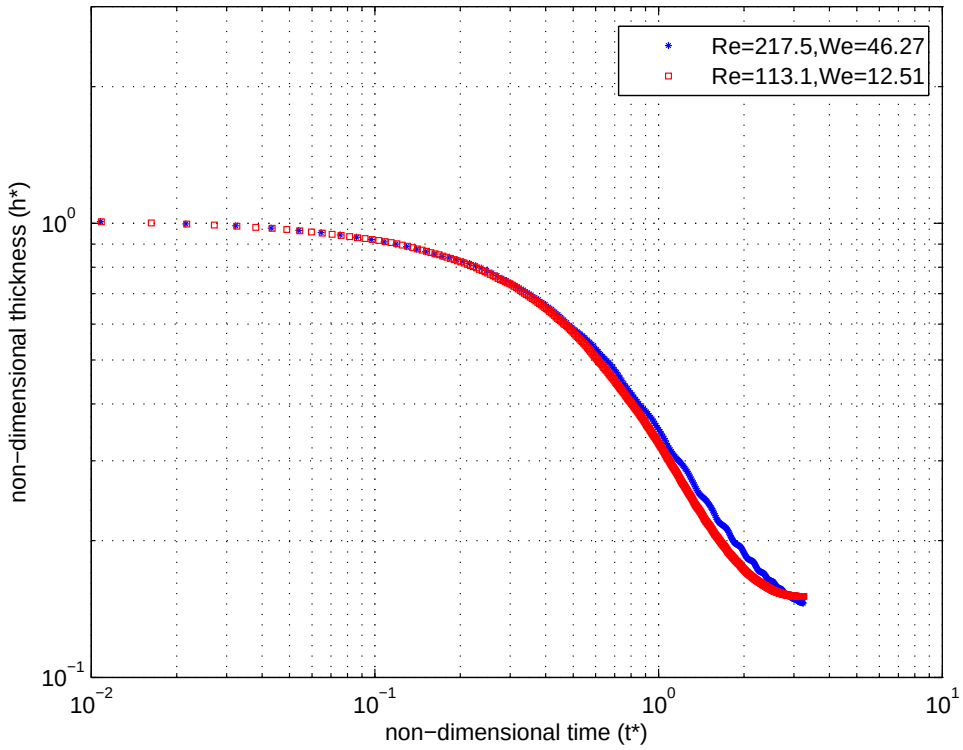

Figure 4.19: Temporal variation of film thickness at the north pole of the tube for different Reynolds number and Weber number with Ga=3512, B_0=3.42, contact angle=60°.

ber 3512. There are different observation comparing the simulation with Ga=219.5, the effect of gravity on the temporal variation of flim thickness can be evaluated from these two groups simulations. It can be seen that the influence of gravity on the second phase appears with increasing Galilei number, while the rate of film thinning becomes slower for the high Reynolds number case. This is because the influence of gravity is not considered into the non-dimensional time. From Fig. 4.20, it is clear that when evolution time t is non-dimensionalized as $t^{\star} = (tU_0 + 0.5gt^2)/D_0$, the non-dimensional temporal variation of film thickness for varied Reynolds number collapses onto a single curve again in the second phase. In order to evaluate the effects of the surface tension on the dynamics of the film flow process, simulations were conducted for different values of Weber number while the wettability of solid surface and Reynolds number were held constant as $\theta = 91°$ and 65.25. The gravity force is ignored in this case. In Fig. 4.21, the time evolution of the dynamics of film flow at the cylindrical surface with varied Weber number is shown. It can be seen that the effect of surface tension can be neglected in the first and second phases, and the rate of film thickness reduction is the same. However, the surface tension dominates the inertial force at the end of the second phase, the transition to the retraction phase occurs earlier for the low Weber

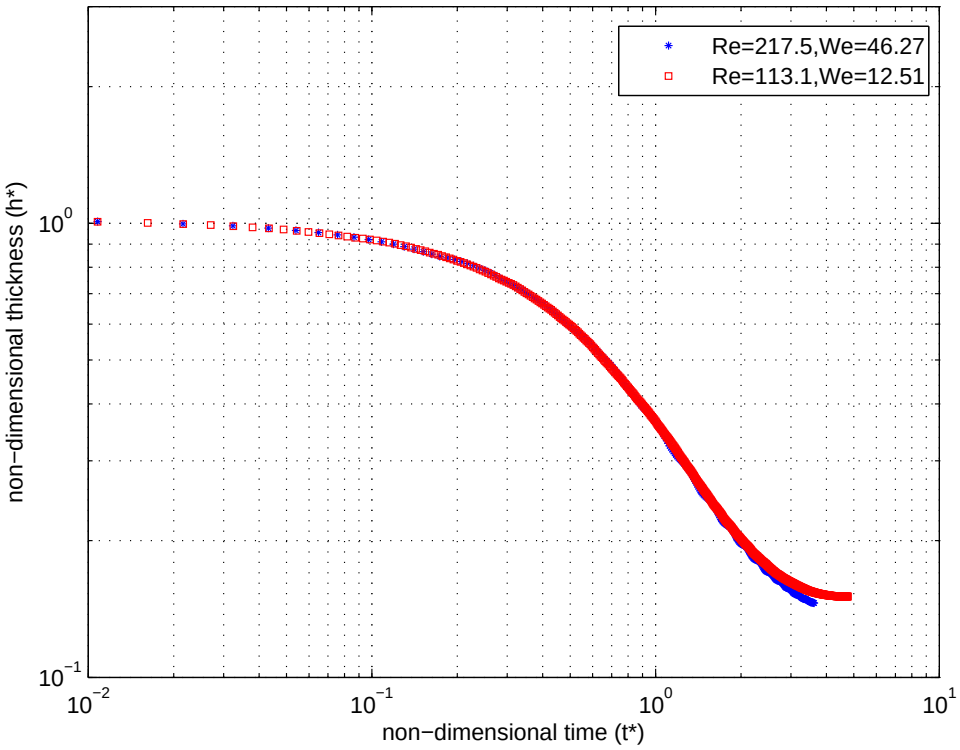

Figure 4.20: Temporal variation of film thickness at the north pole of the tube for different Reynolds number and Weber number with Ga=3512, B_0=3.42, contact angle=60° and $t^\star = (tU_0 + 0.5gt^2)/D_0$.

number case.

4.2.3 Conclusions

The liquid droplet impact on a curved target has been simulated by a two-dimensional multi-relaxation time (MRT) lattice Boltzmann model which can tolerate high density ratios and low viscosity. It is shown that three distinct temporal phases of the film dynamics can be clearly observed from the simulation results which is consistent with the experimental study of Bakshi et al. [89]. In the first phase, the non-dimensional film thickness follows the correlation given by $h^\star = 1 - t^\star$. The inertia dominates the viscous forces during the second phase, while the non-dimensional time and film thickness satisfy the relation $h^\star = 0.33/(t^\star)^{0.9}$. In the third phase, the film thickness increases under the action of the interfacial tension and almost reaches a constant value at last due to the balance of surface tension, viscous force and gravity. The non-dimensional time and film thickness curve for different values of Reynolds number collapses onto a single curve in the first and second phases which is in line with the experimental results [89] when the Reynolds number is controlled by the impact velocity. However, differen-

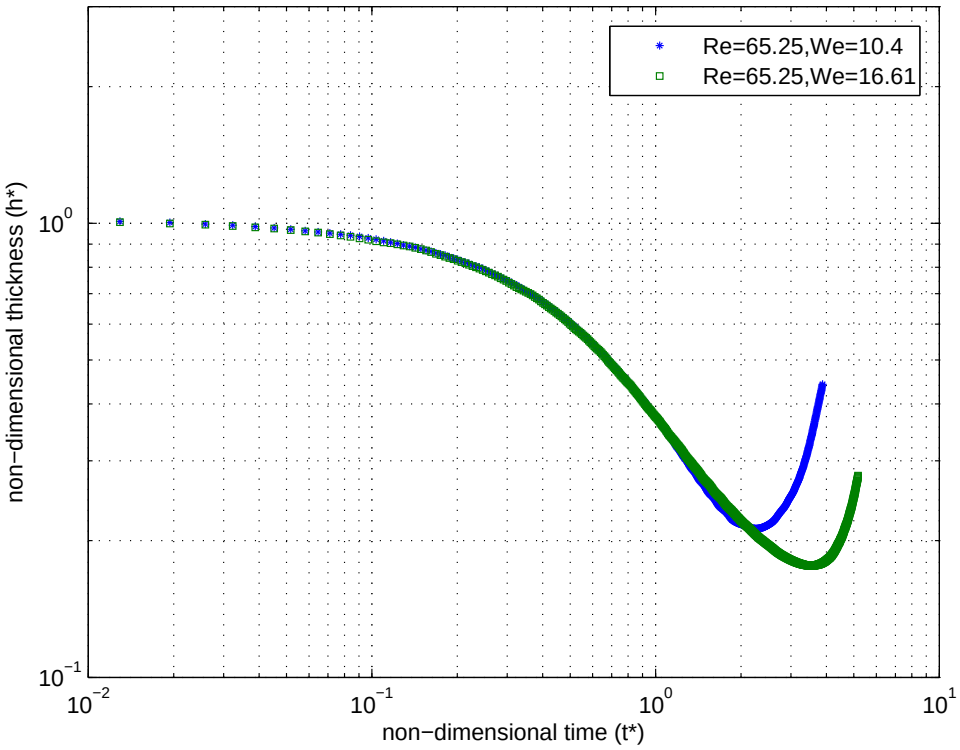

Figure 4.21: Temporal variation of film thickness at the north pole of the tube for different Weber number with contact angle=91° and Re=65.25.

t phenomena can be observed for the case that varied Reynolds number obtained by changing the kinematic viscosity. It can be seen that the non-dimensional time and film thickness curves for varied Reynolds number do not collapse onto a single curve in the second phase, and the rate of film thickness reduction becomes slower with increasing kinematic viscosity. Therefore, the influence of the viscous force in the second phase can not be neglected for the low Reynolds number case. The effects of gravity and surface tension on the dynamics of film flow are also investigated in the current paper. It is found that the influence of gravity on the second phase appears with increasing Galilei number, the rate of film thinning becomes slower for the high Reynolds number case when evolution time is non-dimensionalized as $t^\star = tU_0/D_0$, while the film thickness reduction rate will remain the same when $t^\star = (tU_0 + 0.5gt^2)/D_0$. From the simulation results, the effect of surface tension can be neglected at the first and second phases, while the surface tension dominates the inertial force at the end of the second phase, the transition to the retraction phase occurs earlier for low Weber numbers.

4.3 Dynamics of droplet impact on the cylinder from 45° with horizon

The dynamics of the film flow at the cylinder from 90° with horizon is investigated in section 4.2. However, the droplet impact onto the side of the cylinder is a more common phenomenon in industrial equipment. Especially in fixed bed and micro-channels, the contact line between liquid and solid surface and dynamic behavior of the droplet are important for the catalytic reaction process. In the following section, the dynamic behavior of the droplet impact onto a cylindrical surface with its center offset from the centerline of the tube is shown. The effects of the static contact angle, the Reynolds number, and the Weber number are investigated. Non-slip wall boundary conditions have been used on the sphere surface and periodic boundary conditions have been used on all sides of the domain.

4.3.1 Dynamic behavior of droplet impact onto the side of the tube

Fig. 4.22 shows the snapshots of impact of a liquid droplet landing on a cylinder, with Reynolds number of 78.3, Weber number of 23.99, Bond number of 0.515, density ratio ρ_l/ρ_g of 580 and contact angle of 107°. The droplet falls towards the cylinder after 50000 lattice time steps, with its center offset by 65 nodes from the centerline of the tube. The evolution time t is non-dimensionalized as $t^\star = tU_0/D_0$, where t is the number of time steps elapsed after the drop contacts the surface. Immediately after impact, the process is similar with the first phase of the droplet impact onto the cylinder, which is the initial drop deformation period ($t^\star$=0.078). Then the liquid droplet spreads out on the surface of the cylinder. Since the impact point of the droplet is off-set relative to the cylinder, the flow pattern is not symmetrical, and the majority of the liquid flows downwards rather than towards the upper part of the tube. The liquid lamella appears as the liquid flows in an upward manner towards the north pole of the cylinder ($t^\star$=0.62). The upward motion tendency of the liquid is captured at $t^\star$=0.853, where the droplet is pulled down by gravity. As a result of the inertial force and gravity, the bulk of the droplet continues to flow downwards, being stretched and growing longer and thinner ($t^\star$=1.55 and $t^\star$=3.1). However, with the bulk of the liquid flowing downwards, the impact and potential energy of the droplet are dissipated in overcoming the viscous flow effects and in spreading out its surface area. Hence, the downward stretching is stopped at about $t^\star$=4.19, after which the bulk droplet is pulled back onto the cylinder surface under the action of surface tension force ($t^\star$=5.897). As the downward liquid flow increases and concentrates at the bottom of the tube, the liquid droplet is stretched again under the action of the gravity and inertia ($t^\star$=8.53). At the same time, the liquid droplet continues to move upwards along the cylindrical surface after crossing the bottom of cylinder ($t^\star$=10.862). However, the

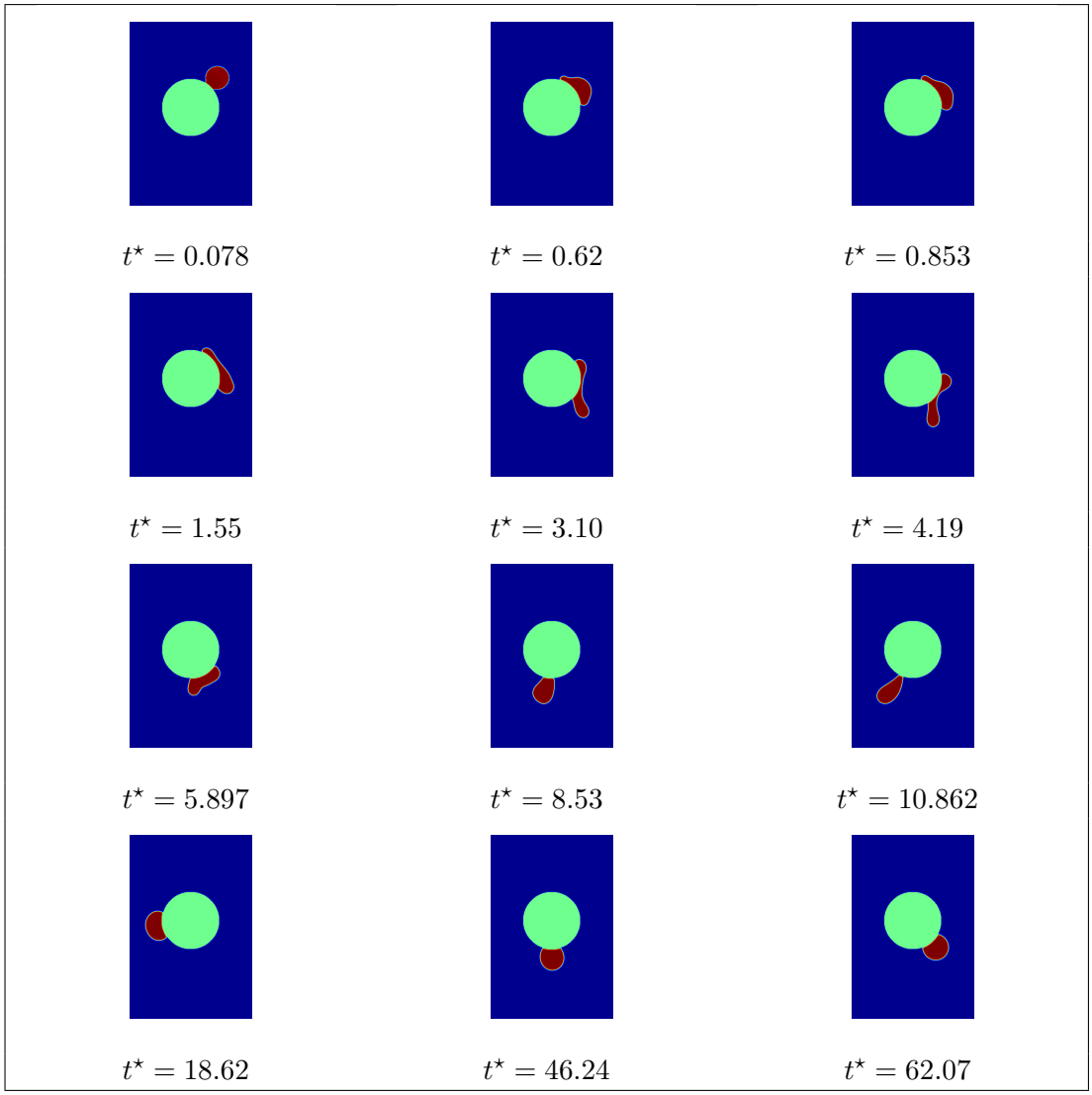

Figure 4.22: Computational snapshots of droplet impact on the side of tube; We=23.99, Re=78.3, density ratio=580, Bond number=0.515, contact angle=107°.

surface tension dominates the inertial and gravitational force and the upward kinetic energy is dissipated by viscous effects ($t^\star$=18.62). Finally, the droplet flows back to the bottom under the action of gravity and continues to resemble a pendular motion until an equilibrium state is reached ($t^\star$=46.24 and $t^\star$=62.07).

4.3.2 Effect of contact angle

In order to investigate the effect of the wettability on the dynamic behavior of droplet after impact onto the cylindrical surface, the droplet impacts on a hydrophilic wall (contact angle = 75°) and on a hydrophobic wall (contact angle = 107°) are simulated for the same Weber number and Reynolds number. Fig. 4.22 and Fig. 4.23 show the time evolution of droplet impact on hydrophobic and hydrophilic cylindrical surface

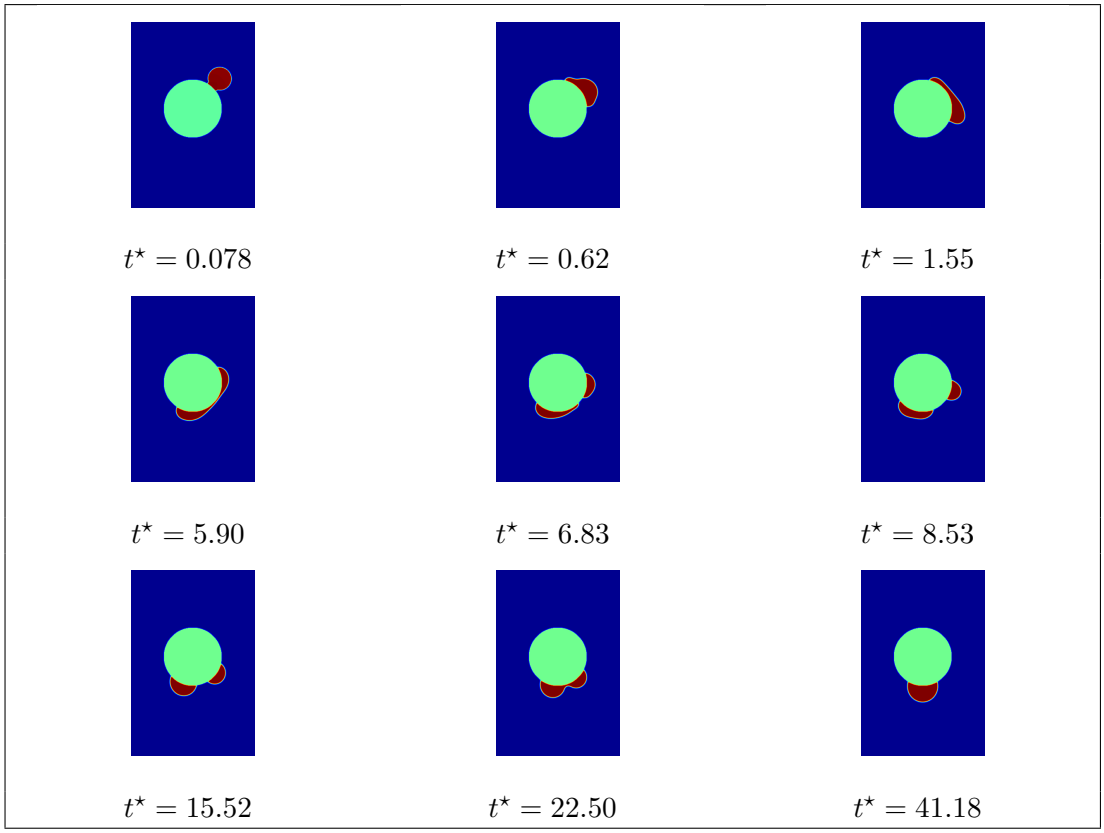

Figure 4.23: Computational snapshots of droplet impact on the side of tube; We=23.99, Re=78.3, density ratio=580, Bond number=0.515, contact angle=75°.

respectively with density ratio $\rho_l/\rho_g = 580$, $Re = 78.3$ and $We = 23.99$. From Fig. 4.23, it can be observed that the contact line between the liquid and the solid surface is longer for the hydrophilic case than for the hydrophobic one shown in Fig. 4.22. In the case of hydrophilic wall, the contact line between the solid surface and the liquid is increasing with the downward liquid flow and breaks up into two parts on the surface after reaching a maximum contact line. Then the two droplets begin to retract due to interfacial tension and move towards the bottom of the tube at the same time. At $t^\star$=22.5, the two droplets merge together, where an equilibrium shape is reached at $t^\star$=41.18. On the other hand, in the case of the hydrophobic wall (Fig. 4.22), there is a process that the bulk of the droplet is stretched and grows longer and thinner as it moves along the surface of the tube. After the maximum elongation has been reached, surface tension dominates the recovery process and the droplet is attached to the tube wall. However, in the case of the hydrophilic wall (Fig. 4.23), the stretching and oscillation behavior is not as obvious as that in Fig. 4.22 and the time to reach the equilibrium state is shorter than for a hydrophobic wall. This is because of the longer contact line in the hydrophilic wall case. Thus, a higher proportion of the initial impact energy is dissipated in overcoming the viscous effects and surface tension.

4.3.3 Effect of kinetic energy

In order to investigate the dependency of the kinetic energy on the dynamic process of droplet impact onto the cylinder, simulations were conducted with various Weber number and Reynolds numbers while the density ratio between liquid and gas, wettability of surface and Bond number were held constant. Fig. 4.24 shows the time

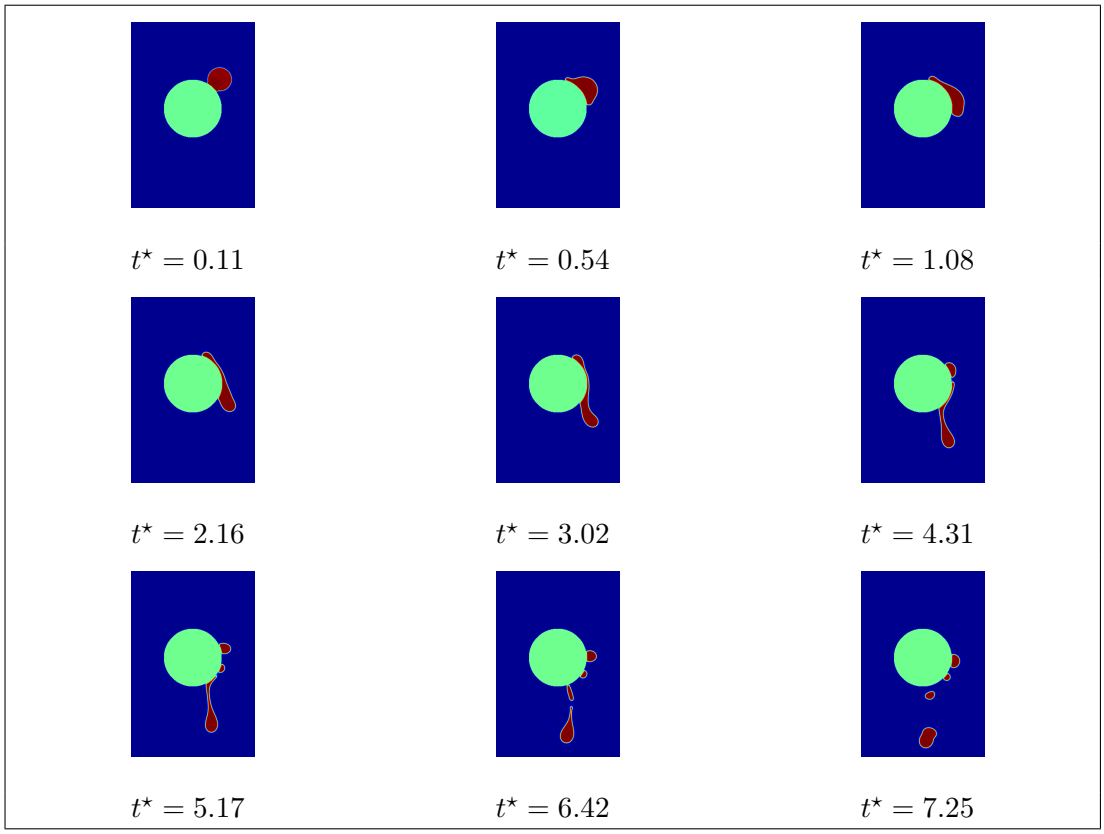

Figure 4.24: Computational snapshots of droplet impact on the side of tube; We=46.27, Re=108.75, density ratio=580, Bond number=0.515, contact angle=107°.

simulated images of the dynamic behavior of the liquid droplet impact onto cylindrical surface with Weber number 46.27 and Reynolds number 108.75. The values of contact angle and Bond number are the same as in Fig. 4.22. It can be seen from Fig. 4.24, that the liquid breaks up into three smaller drops on the surface with the film thinning and contact area increasing. The third part of the drop continues to flow downwards with higher velocity and results in a column of liquid being suspended from the tube ($t^\star$=5.17). The velocity of the lower portion of the droplet is larger than that in the upper portion, which causes the lower portion of the bulk of the liquid to be pinched off from the upper portion. Then the upper portion is subsequently detached from the tube due to inertia dominating surface tension ($t^\star$=6.42 and $t^\star$=7.25). Thus, as it is expected, higher Weber number flows will result in surface droplet breakup and droplet detachment from the tube, something that does not occur in lower Weber number flows

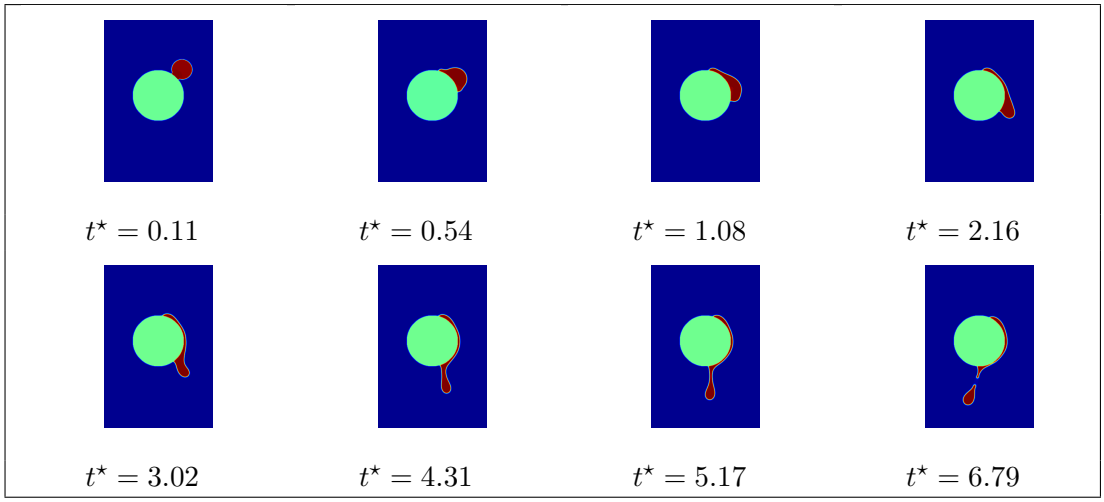

Figure 4.25: Computational snapshots of droplet impact on the side of tube; We=46.27, Re=108.75, density ratio=580, Bond number=0.515, contact angle=60°.

(Fig. 4.22). In addition, since the surface is non-wetting, the liquid has a reduced affinity for the solid surface, and in turn the surface interactions from the solid reduce the surface energy. This leads to the less initial kinetic energy of droplet be dissipated and a strong liquid elongation flow along the surface eventually leads to a breakup of the droplet on the surface. In order to validate the above conclusion, a case of hydrophilic surface wall (contact angle = 60°) which has the same Weber number and Reynolds number as in Fig. 4.24 is performed. From Fig. 4.25, it can be observed that the surface droplet breakup does not occur in hydrophilic surface due to the higher kinetic energy dissipation on surface energy. However, similar to the hydrophobic case shown in Fig. 4.24, the bulk of the droplet suspends below the tube and detachment occurs as the liquid elongation reaches a critical state at $t^\star$=6.79.

4.3.4 Conclusions

The investigation of dynamic behavior of droplet impact on the side of the cylinder is included in this study. At the same time, the effects of surface characteristics and impact velocity on the dynamic behavior are evaluated. From the simulation study, it can be concluded that the contact line between liquid and solid surface on hydrophilic wall is longer than for hydrophobic surface and higher kinetic energy will be dissipated on the hydrophilic wall. In addition, increasing the initial kinetic energy will result in a droplet breakup and in the case of high impact velocity, the use of a hydrophilic surface can assist in averting the surface droplet breakup during the impacting process. Moreover, the simulation of the dynamic process of droplet impact onto the side of cylinder supports the proof that the pseudo-potential LB model has the capability to capture

interfacial topological changes like snap-off, which is a very important phenomenon for the study of the two phase flows in porous media. In the multiphase flow in porous media, a combination of low Ca values with low saturation of non-wetting phase leads the appearance of large-ganlion dynamics regime. In the large-ganlion dynamics, in which the non-wetting phase is totally disconnected in the form of ganglia. The previous study on the dynamic behavior of non-wetting phase blob depending on the solid phase with different shape and different wettability is significative for the large-ganlion dynamics regime in multiphase flow in porous media [110].

Chapter 5

Immiscible two-phase flows in artificial porous media

In this chapter, a two-dimensional high density ratio MRT LBM is applied to study the impact of geometrical properties on the immiscible two-phase flows in porous media. The porous media structures with different geometrical properties are artificially generated by a Boolean model based on a random distribution of overlapping ellipses/circles. Firstly, the capability and accuracy of the high density ratio MRT LBM is evaluated by simulating the immiscible two-phase co-current flow between two parallel plates. Then, the immiscible two-phase flow in porous media with different non-wetting phase saturation depending on the porosity, contour length and connectivity of solid phase in porous media is addressed.

5.1 Generation of the pore space

In this section, the mathematical framework to quantify and generate the artificial porous media is introduced. It has been demonstrated that the permeability of sedimentary rock samples is very close to those of Boolean models [143]. Integral geometry furnishes a suitable family of morphological descriptors, known as Minkowski functionals [144, 145]. Minkowski functionals are defined for sets Ξ which can be written as finite unions of compact convex sets Ξ_i, $\Xi = \bigcup_{i=1}^{n} \Xi_i$. In two dimensions there are three Minkowski functionals, namely the area A, the contour length C and the Euler characteristic χ which is the number of connected objects minus the number of enclosed cavities. The Boolean model is a certain random set $Z \subset \mathbb{R}^d$ which is used to model various random geometric patterns. The Boolean process can be realized in two simple steps: Firstly, points x_i (called germs) are scattered randomly and independent of each other across space according to a stationary Poisson process. Secondly, a random object Z_i which is called a grain is placed in every random point x_i. An outcome of the Boolean model is then generated as the union set of all such germ-grain pairs.

$$Z = \bigcup_{i=1}^{\infty}(Z_i + x_i). \tag{5.1}$$

We consider a two-component medium filling a square area $S = l^2$. The global morphology of this two-phase complex material is defined by the global Minkowski functionals per unit area, namely: the solid phase fraction ϕ, the contour length to area ratio L and the mean value of the Euler characteristic $\bar{\chi}$. The global morphology can be related to a Boolean process defined by the morphological measures of the individual grains $V_\nu(Z)$ [146, 147]

$$\phi = 1 - e^{-\rho V_0}, \tag{5.2}$$

$$\frac{L}{4} = e^{-\rho V_0}(1 - e^{-\rho V_1}), \tag{5.3}$$

$$\bar{\chi} = e^{-\rho V_0}(-1 + 2e^{-\rho V_1} - e^{-2\rho V_1 - \rho V_2}), \tag{5.4}$$

where ρ is the intensity of the germs in the two dimensional porous media. In other word, ρ is defined as the number of particles per area. The measures V_ν are related to the Minkowski functionals of individual grains which include the surface area A, the contour length C and the Euler characteristic χ with a value of 1 for convex sets.

$$V_0 = A/lu^3, \tag{5.5}$$

$$V_1 = C/(4lu^2), \tag{5.6}$$

$$V_2 = \chi = 1, \tag{5.7}$$

where lu is defined as lattice unit. V_ν for an ensemble of n grains is given by averaged values $V_\nu = \sum_{j=1}^{n} p_j V_{vj}$, weighted by the probability of their occurrence, p_j. In the current work, the porous media are created by using uniform grains (circles or ellipses) with same size.

Two groups including four artificial structures each with given values of the specific global Minkowski functionals are generated. These values can be fixed arbitrarily in an attempt to compare porous media with different geometric properties. The intrinsic permeability, global Minkowski functionals, as well as the representative elementary volume (REV) of the different artificial porous structures are shown in Table. 5.1. The porous structures obtained with these properties are shown in Fig. 5.1. The Euler characteristic [148] of the conducting phase ($\bar{\chi}_0$) in Table. 5.1 is distinguished from the $\bar{\chi}$, by neglecting the cavities inside the solid clusters which do not contribute to the fluid

flow. From these global morphological parameters and Eqs. (5.2-5.4) one can determine the Minkowski functionals of individual grains with intensity ρ, and consequently the generation of the artificial structures can be realized by a Boolean process. In some cases the results of the global Minkowski functionals for a specific realization might not be exactly the same as the predefined ones. In this case, the code should keep looping until the structure with similar global Minkowski functionals compared with the predefined ones is obtained (as shown in the Fig. B.1 in the appendix). The deviation is controlled at a level of 0.1%.

5.2 Model validation: viscous coupling in co-current flow in a two-dimensional channel

In this section, the immiscible two-phase co-current flow between two parallel plates to evaluate the accuracy of the MRT LBM is studied. In the immiscible two-phase flow in porous media, the wetting phase typically attaches to and moves along the solid surface in the form of films, while the non-wetting phase flows in the center of the pores. Hence, for the simulation of immiscible two-phase flows in a 2D channel, the non-wetting phase is sandwiched by the wetting phase which is in contact with the solid walls as depicted in Fig. 5.2. The degree of saturation of each fluid phase can be defined as the occupied width of the same fluid divided by the entire width of the channel. Assuming a Poiseuille-type of flow in the channel, the analytical solutions for the velocity distribution can be derived by solving the relevant Navier-Stokes equations [136]:

$$u(x) = \begin{cases} \frac{G}{2\nu_w\rho_w}(l^2 - x^2), & l' < |x| < l, \\ \frac{G}{2\nu_w\rho_w}(l^2 - l'^2) + \frac{G}{2\nu_{nw}\rho_{nw}}(l'^2 - x^2), & 0 < |x| < l', \end{cases} \tag{5.8}$$

where ν_w, ν_{nw}, ρ_w, ρ_{nw} are the kinematic viscosities and densities of the wetting non-wetting phases respectively. The distance from the centreline between the two plates

Structure	ϕ	L	$\bar{\chi}_0(10^{-3})$	κ	REV(ϕ)	REV(L)	REV($\bar{\chi}_0$)
Group 1							
1	0.3744	0.094	-0.536	4.4986	700	700	600
2	0.3259	0.0928	-0.534	5.1601	600	600	500
3	0.3738	0.0828	-0.537	6.5142	650	600	600
4	0.3738	0.094	-0.711	5.6838	700	700	700
Group 2							
1	0.3260	0.0988	-0.711	5.0936	500	700	600
2	0.2641	0.0984	-0.717	5.5500	700	700	600
3	0.3297	0.0844	-0.710	8.3375	600	700	600
4	0.3294	0.0980	-0.925	6.6612	650	700	700

Table 5.1: Geometrical properties of the porous structures.

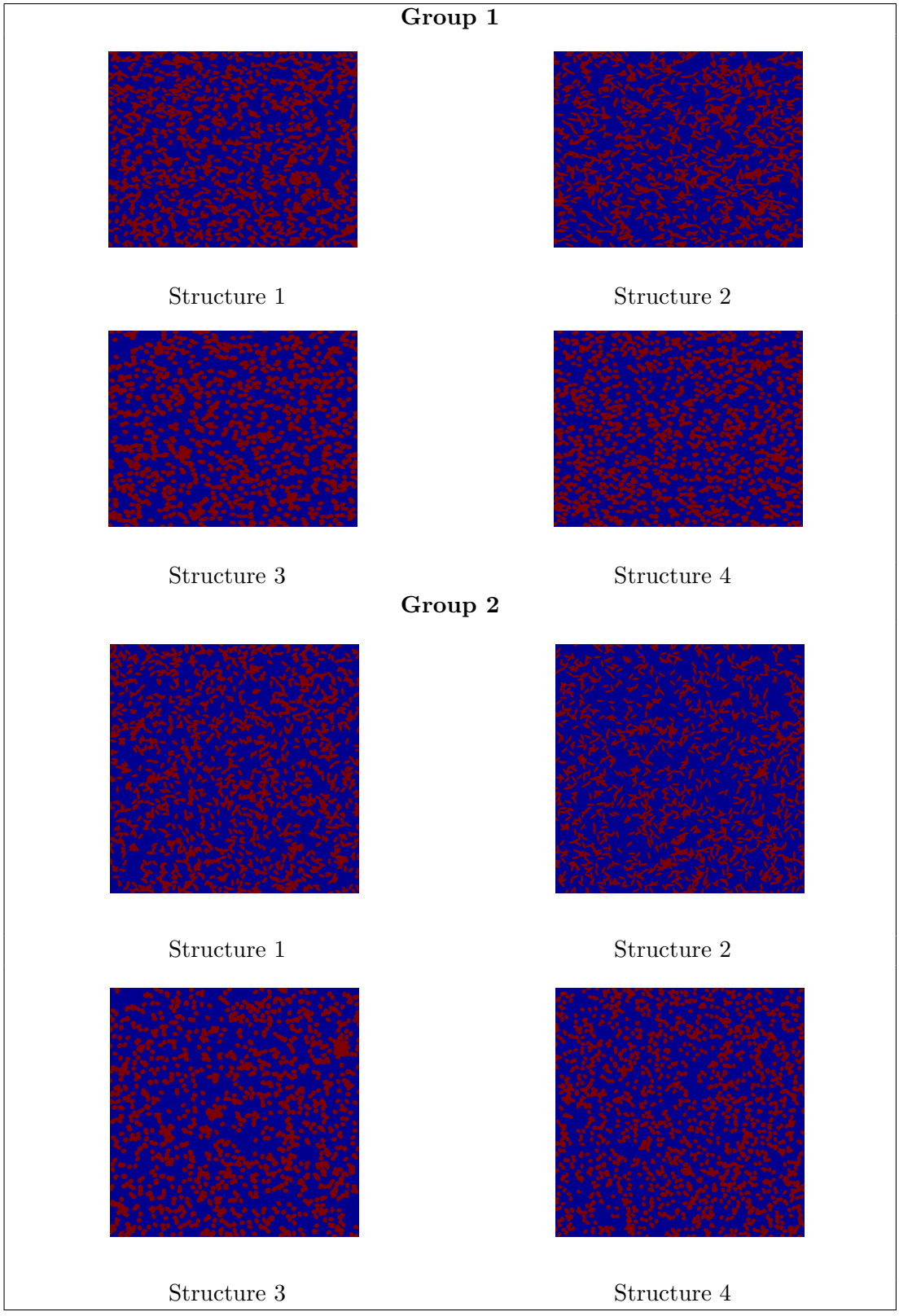

Figure 5.1: Porous media corresponding to the properties shown in Table. 5.1.

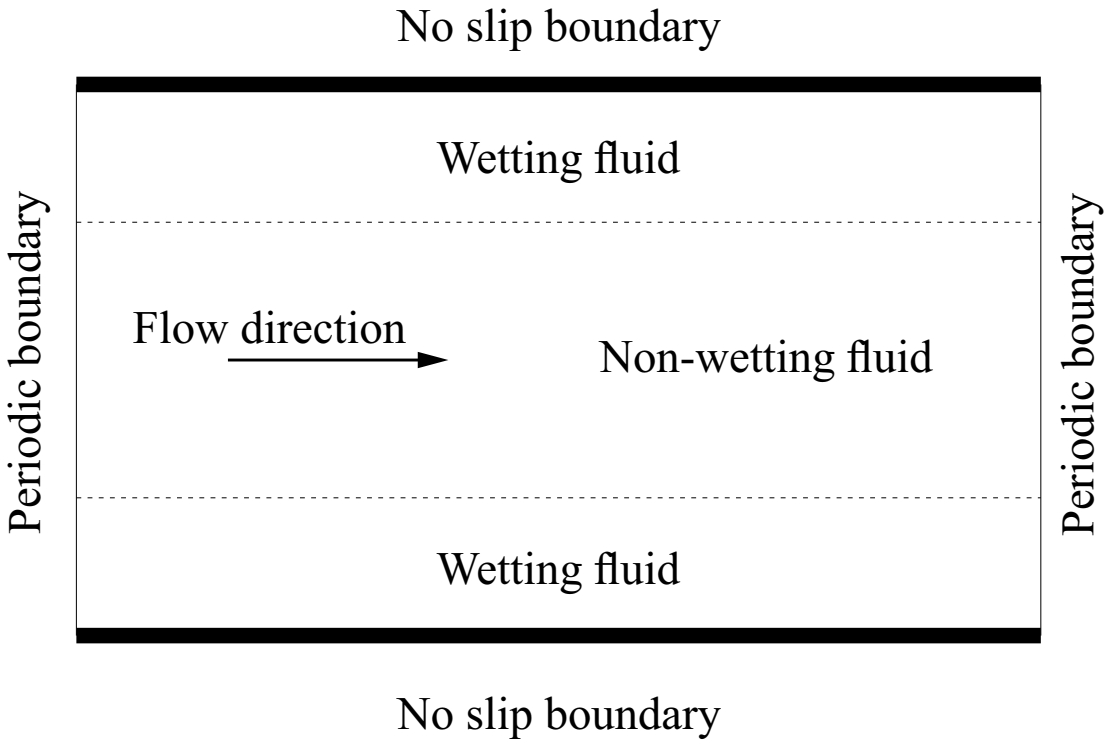

Figure 5.2: Schematic of two phase flow between two parallel plates.

to the solid boundary is l, while l' represents the distance from the centreline to the wetting-non wetting phase interface. The pressure gradient in the direction of the flow is taken as G. The relative permeability of each phase is defined in terms of the superficial velocity of the fluid particles across a cross-section perpendicular to the flow direction.

$$k_{r,w} = \frac{\int_{|x|=l'}^{l} \nu_w dx}{\int_{|x|=0}^{l} \nu_w dx}. \tag{5.9}$$

$$k_{r,nw} = \frac{\int_{|x|=0}^{l'} \nu_{nw} dx}{\int_{|x|=0}^{l} \nu_{nw} dx}. \tag{5.10}$$

From Eqs. (5.8)-(5.10), the relative permeabilities are given by [135]

$$k_{r,w} = \frac{1}{2} S_w^2 (3 - S_w) \tag{5.11}$$

$$k_{r,nw} = S_{nw}[\frac{3}{2}M + S_{nw}^2(1 - \frac{3}{2}M)], \tag{5.12}$$

where M is defined as the viscosity ratio ν_{nw}/ν_w. The relative permeability of the wetting phase in the channel is only a function of the wetting saturation S_w, while the relative permeability of the non-wetting phase is a function of both the wetting saturation S_w and the viscosity ratio M. A computational domain of 300×50 lu^2 is

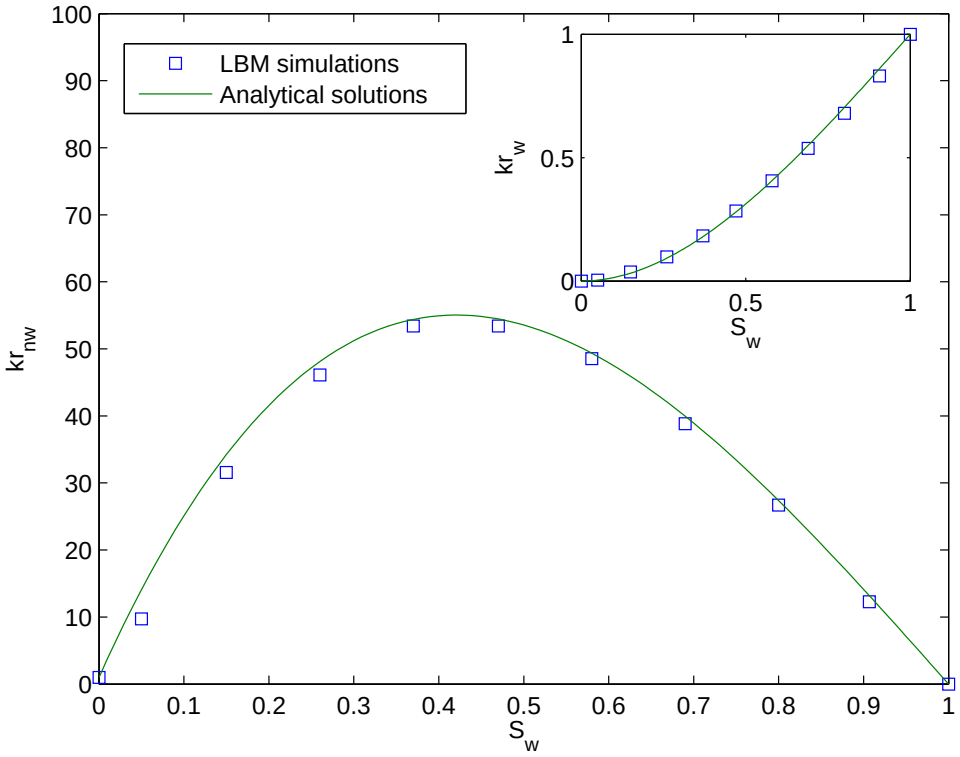

Figure 5.3: Relative permeabilities from LBM model and analytical solutions for the wetting and non-wetting phases in a channel with $M \approx 95$ and $G = 10^{-8}$.

established. One lattice unit is defined as 1 lu. Periodic boundary conditions have been used at the inlet and outlet of the domain and no-slip wall boundary conditions have been applied to the top and bottom boundaries of the domain. A constant external force ($G = 5 \times 10^{-8}$) has been added to each phase and the dynamic viscosity ratio has been set to 95. The relative permeabilities of the wetting phase and non-wetting phases from the numerical simulations and the analytical solutions are shown in Fig. 5.3. It can be seen that the simulation results are in good agreement with the results from the analytical solutions.Therefore, it can be concluded that the MRT LBM model can accurately predict the flow behaviour and fluid phase relative permeability of two phase flows in porous media.

5.3 The impact of the geometrical properties of porous media on the steady state relative permeabilities on immiscible two-phase flows

Following the validation of the MRT LBM with the 2D channel flow, the attention is now focused on the simulation of the immiscible two-phase flow in 2D porous media

structures generated with different Minkowski functionals.

The eight artificial porous media are generated as shown in Fig. 5.1. The size of every computational domain is 800×800 lu^2 and the global Minkowski functionals for each porous medium are given in table. 5.1. Periodic boundary conditions have been applied in all directions, while no-slip wall boundary conditions have been used on the solid surfaces. Initially, the wetting and non-wetting phases are uniformly-distributed in the porous media such that the desired wetting saturation is obtained. Obtaining different wetting saturation depends on the different choice for uniformly distributed random variable. The constant external force G is applied on both fluids along the flow direction. The reasons for using body forces instead of imposing a pressure gradient as a driving force are that body forces are convenient to implement and also can avoid capillary pressure gradients and saturation gradients along the flow direction [134]. Since we are interested in the impact of the geometrical properties on the two-phase flow in porous media, the viscosity ratio between the two phases and the contact angle are set to $M \approx 103$ and $\theta = 180^{\circ}$. The interfacial tension is 0.0044 and the density ratio has been set to 103. It is assumed that the final steady state is achieved when the following criterion is satisfied:

$$\frac{\sqrt{\sum_x^2[u_x(x,t) - u_x(x,t-10000)]}}{\sum_x u_x(x)} < 10^{-4}, \tag{5.13}$$

where u_x is the macroscopic velocity along the flow direction x. The number of time steps needed to achieve the steady state increases significantly as the wetting phase saturation increases. This should be attributed to the wetting phase being less viscous than the non-wetting phase [135]. In order to estimate the relative permeabilities for both phases, the steady state superficial velocity of each phase is calculated. The relative permeabilities for the non-wetting phase and wetting phase are calculated following the extension of Darcy's law defined. The intrinsic permeability of a specific porous medium is determined by Darcy's law after applying a constant body force for a single phase and setting the density of the other fluid equal to zero at all void locations.

In the case of immiscible two-phase flows in porous media, the interfacial geometry, phase distribution patterns and dynamics vary with the fluid saturation. Fig. 5.4 shows the initial and steady state two-phase distribution patters when the wetting saturations are $S_{nw} = 0.15$, $S_{nw} = 0.6$ and $S_{nw} = 0.85$. The geometrical properties of the selected porous medium are $\phi = 0.3744$, $L = 0.094$ and $\bar{\chi} = -0.536 \times 10^{-3}$. From Fig. 5.4, it can be seen that the wetting phase is continuous, while the non-wetting phase is disconnected and trapped into big pores as form of blobs when its saturation is 0.15. For the case of $S_{nw} = 0.6$, the non-wetting phase is partially connected, while the wetting phase is still continuous. For the case of $S_{nw} = 0.85$, the wetting phase covers the solid surfaces, while the non-wetting phase is fully continuous and flows among the wetting phase films. For this case, three flow regimes have been identified in the

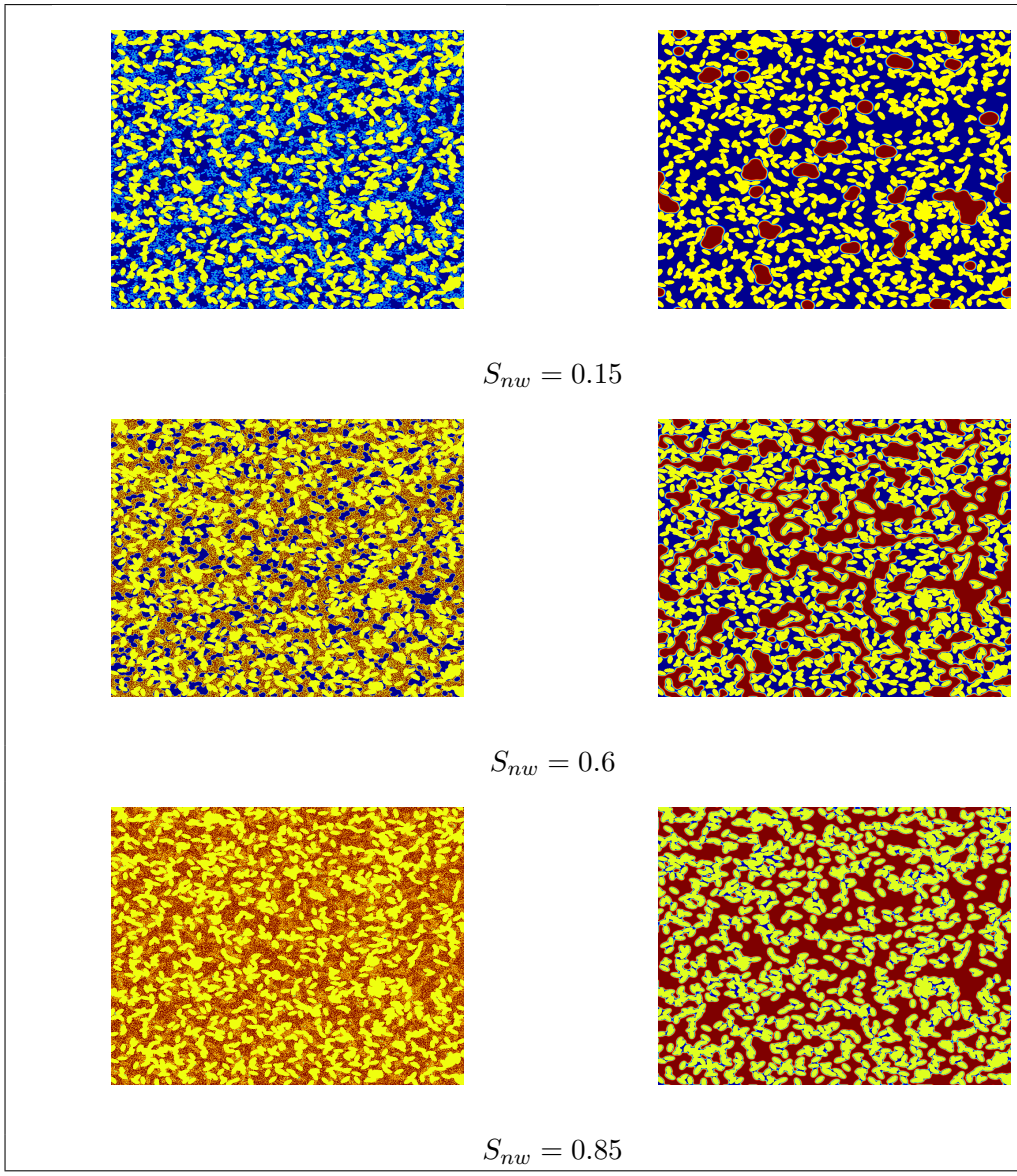

Figure 5.4: The initial co-current flow (left column) and the final steady-state (right column) two-phase distribution patterns in the cases of $S_{nw} = 0.15$, $S_{nw} = 0.6$ and $S_{nw} = 0.85$ when $G = 10^{-5}$. The non-wetting phase is indicated by red colour, while blue colour represents the wetting phase.

previously published literature [133, 138]. A wetting phase Darcy-type regime can be observed for very low levels of driving forces where the capillary pressure dominates the viscous forces. At intermediate values of driving forces, which result to a corresponding intermediate capillary number, the effect of viscous force becomes important and a non-linear two-phase flow regime is observed. Further increase of the driving force leads to a Darcy-type two-phase regime where the effect of capillary forces can be neglected. It was observed that an increased viscosity ratio leads to an apparently increased non-wetting phase relative permeability due to the lubricating effect of the

wetting phase film attached to the pore wall [136]. The current study focuses on the intermediate and high capillary number regimes.

In contrast to constructing porous media statistically, in the current work, the value of a single Minkowski functional is varied while the other functionals are kept constant during the artificial porous media generation. With this procedure, the effect of each geometrical property (porosity, surface area, connectivity) to the immiscible two-phase flow in 2D porous media can be determined and quantified. The problem of how each individual Minkowski functional affects the relative permeabilities of both phases in non-linear and linear two-phase flow regimes for various G and S_{nw} is investigated. It has to be also noted that 2D simulations present certain shortcomings compared to 3D simulations, where the percolation thresholds of the porous structures are significantly lower than the 2D ones. Hence, one should expect that the critical fluid phase saturation values in the real 3D porous structure will be lower than the corresponding 2D, since the probability of finding a connected pore network is higher. Differences in the long range connectivity of the wetting phase in the form of thin films and corner flow

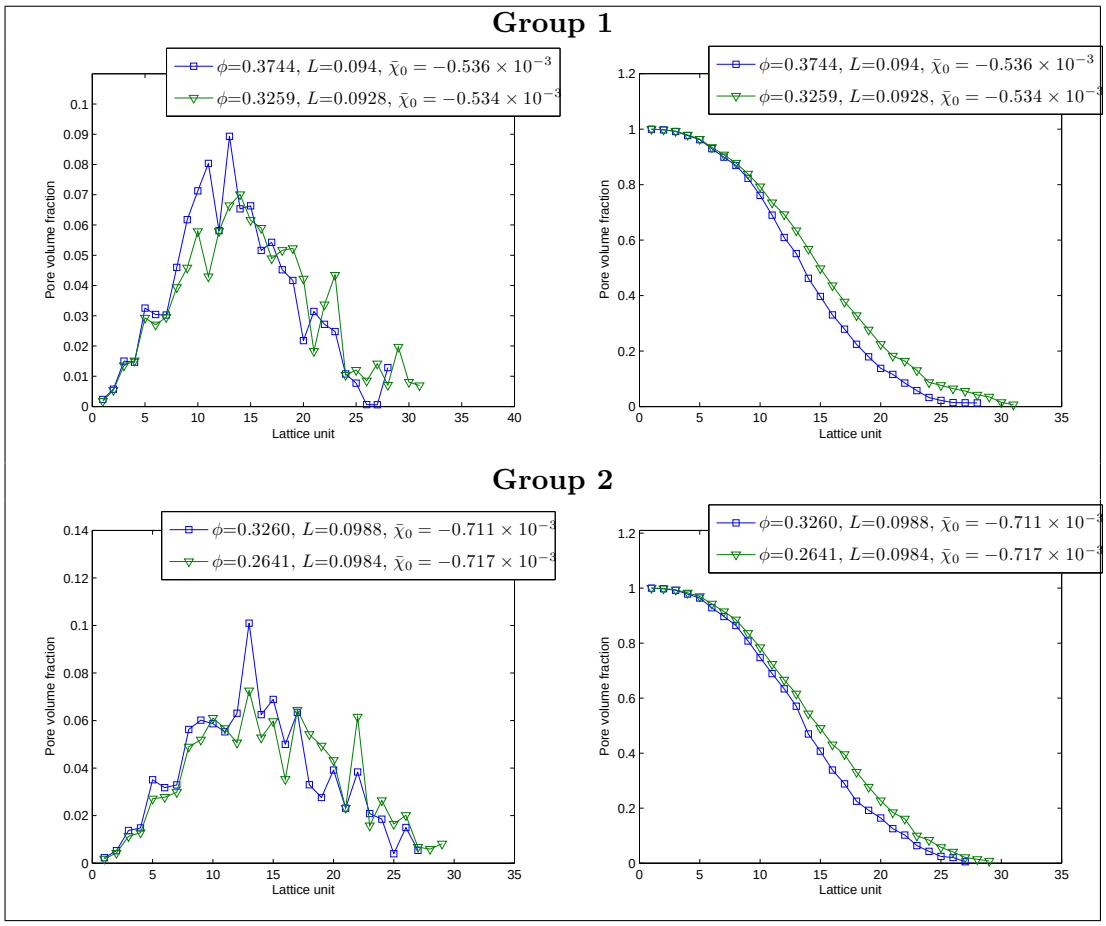

Figure 5.5: Pore size (left column) and cumulative (right column) distributions of porous structures 1 and 2 of Groups 1 and 2.

are also present.

5.3.1 Porosity effects

Geometrical properties

In order to investigate the effect of volume fraction, four artificial porous structures (1 and 2 in Groups 1 and 2 of Table. 5.1) with different porosity but similar surface area and connectivity have been generated. Capillary forces in two-phase flow in porous media depend on the pore size distribution. The pore size distribution can be characterized through the computation of the density of the spherical contact distribution [149]. The distance of each pore pixel to the solid phase is determined by inserting discrete circles with increasing diameters until they touch the solid phase. As a pixel close to the wall can nevertheless be an element of a large circle centred at another position, the size of each pore pixel could be computed as the diameter of the largest sphere that includes this pore pixel. The pore size distributions together with their corresponding cumulative distributions of the four artificial porous media are given in Fig. 5.5.
The cumulative distributions which are defined as the volume fraction of all pores with pore size larger or equal to a certain diameter are shown in Fig. 5.5. It is evident that the density of larger pore sizes is smaller in the structure with low porosity (i.e. larger solid phase fraction ϕ) than in the structure with high porosity. Comparing structures 1 and 2 in each of group, the latter structure has larger porosity with the same contour length and Euler characteristic as structure 1. Increased porous media porosity, given that the rest of the Minkowski functionals are similar, indicates an increased number/fraction of large pore sizes in the medium.

Fully connected flow

In order to verify that the results for the fully connected flow of the non-wetting phase in porous media are not affected by the different initial uniform distribution of the two phases, simulations with different random initial uniform distributions have been carried out. Fig. 5.6 illustrates the average superficial velocity of the non-wetting and wetting phases in artificial structure 1 as as function of the time-step for two cases with different initial uniform distributions. It can be observed that the convergent superficial velocity in both cases is similar. Therefore, the results for fully connected flow in porous media will not be affected by the different initial uniform distribution of the two phases. Generally though, the application of uniform distribution cannot reflect either drainage or imbibition relative permeabilities which are dependent on history [150].

Fig. 5.7 shows the relative permeabilities of the wetting and non-wetting phases as a function of the applied external force G. A set of simulations with high saturation of the non-wetting fluid and a dynamic viscosity ratio of 103 in the two different structures for each of group was performed. The saturation of the non-wetting phase was set up

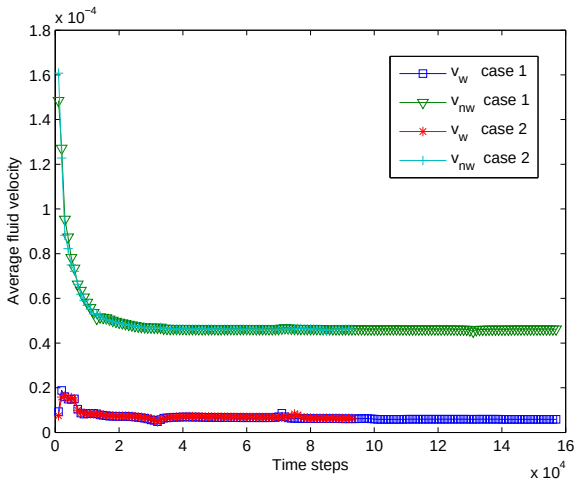

Figure 5.6: The average superficial velocity of the non-wetting and wetting phases as a function of time-step for two cases with different initial uniform distribution; $S_{nw} = 0.85$, $G = 0.5 \times 10^{-6}$ and $M \approx 103$.

as 0.85 in group 1, while $S_{nw} = 0.9$ in group 2. It can be observed that the relative permeabilities of the non-wetting phase in both media are significantly larger than unity due to the lubricating effect. The relative permeabilities of the wetting phase are significantly lower (very close to zero) in both artificial structures, caused by the film flow around the solid surfaces as well as its low saturation. Figs. 5.7 and 5.8 show that the flow rate of the non-wetting phase exhibits a non-linear behaviour at low driving forces through all porous structures. In contrast to that, the relative permeabilities seem to approach a constant value at higher levels of driving forces. This indicates that as the driving force increases, the non-wetting phase is able to overcome capillary pressures associated with the smaller pores in the structure and forms new additional flow paths. The constant relative permeability for different levels of driving forces indicates that there are no newly available flow paths in the structure and thus no further increase is observed. Correlating the previously mentioned observations with the pore size distribution in the different structures, it becomes evident that between two porous media, the one with a higher density of small pores will experience a wider non-linear region. This becomes more clear in the logarithmic plots of Fig. 5.7 as well as the Capillary number vs driving force plots (Fig. 5.8). The non-linear effects of the pore size distribution on the correlation of the relative permeability and Capillary number ($Ca = \mu_{nw} v_{nw}/\sigma$) with the driving forces become more significant at lower porosities of the porous media. It has to be noted that the pore body to pore throat ratio is implicitly embedded into the pore volume distribution of each porous medium and it is not incorporated as an explicit separate parameter in the system.

Fig. 5.7 shows that in the linear region the relative permeability of the non-wetting

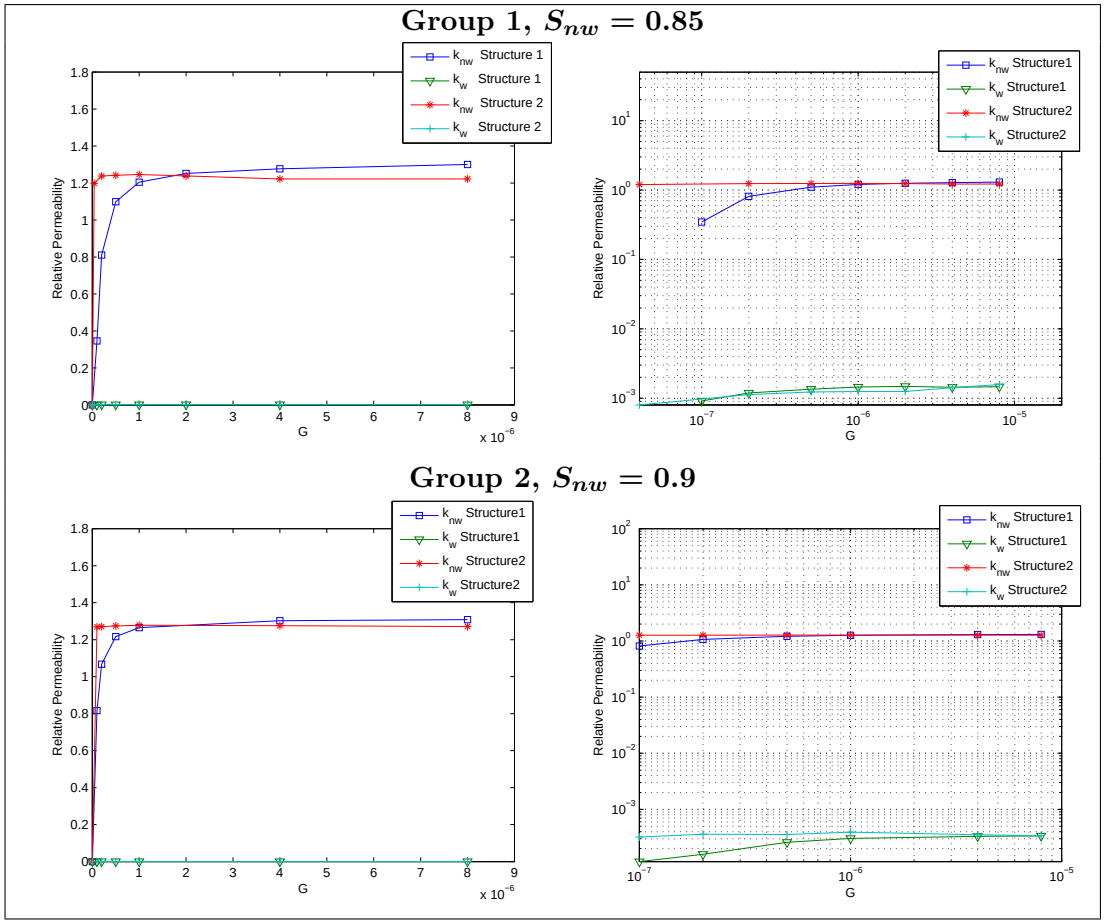

Figure 5.7: Normal (left column) and logarithmic (right column) plots of the relative permeabilities as a function of the driving force G for structures 1 and 2 of Groups 1 and 2.

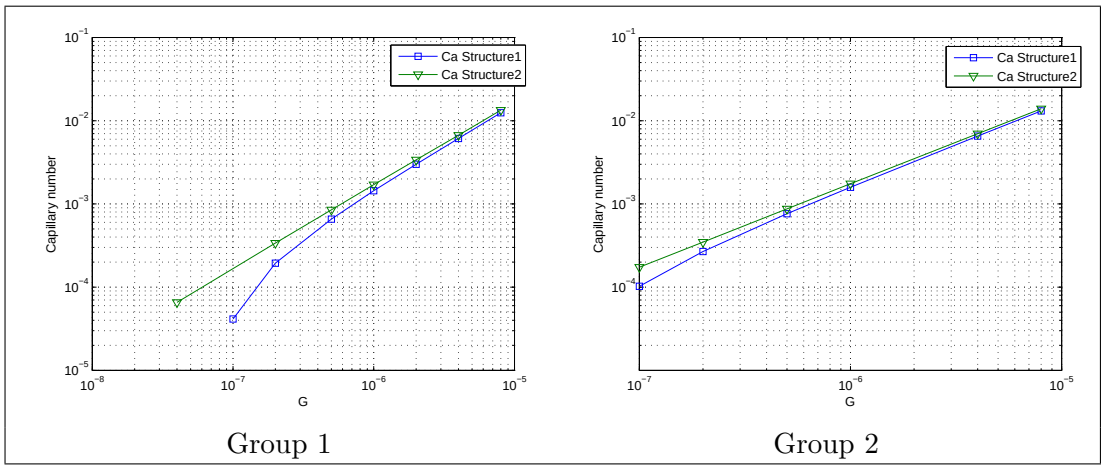

Figure 5.8: Capillary number against the driving force G for two-phase flow in porous structures 1 and 2 of Groups 1 and 2.

phase in structure 1 is greater (≈ 1.3) than in structure 2 (≈ 1.2). It is found that in this region the value of the surface ratios between fluid-fluid, non-wetting fluid-solid and wetting fluid-solid are similar. The surface ratio between the non-wetting fluid-solid and fluid-fluid approaches 0.015 for both structures in group 1, while it approaches a value of 0.1 in group 2. Hence, the difference in the values of the relative permeabilities between structures 1 and 2 in Fig. 5.7 are not a result of the changes between the fluid-fluid, non-wetting fluid-solid and wetting fluid-solid surface ratios. Fully connected flows of the non-wetting phase in porous structures can be treated as pipe like flows once the linear region is reached (i.e the influence of capillary pressure becomes negligible). In this case, the flow rate of the non-wetting phase increases since the effective pore size decreases due to the existence of a slip boundary caused by the film of the wetting phase covering the solid phase. This observation is in great agreement with the research conducted by Berg et al. [151] regarding pipe flows with slip at the wall. From Fig. 5.8 it can be observed that the Capillary number presents a non-linear behaviour at low driving forces in accordance with the non-wetting phase relative permeabilities. Moreover, the Capillary number versus driving forces relationship approximately collapses onto a single curve for the two structures at high levels of driving forces. However, the fact that structure 1 presents similar Capillary numbers with structure 2 in that region, is attributed to its lower intrinsic permeability, which further enhances capillary pressure effects.

Partially connected flow

Fig. 5.9 shows the average superficial velocity of the non-wetting and wetting phases as a function of the time-step for partially connected flow for two different initial uniform distributions in porous structure 1. The convergent superficial velocity from the two cases is similar, thus the results of the partially connected flow in porous media will not be affected by the different initial uniform distribution of the two phases.

The wetting and non-wetting phase relative permeabilities are investigated at intermediate saturations ($S_{nw} = 0.6$) and high levels of driving forces. As in the case of fully connected flow, the two structures in each group possess the same Minkowski functionals except for the solid phase fraction ϕ. As shown in Fig. 5.10, the non-wetting phase relative permeability is higher for structure 2 in both groups. In contrast to the fully connected flow regime, capillary pressure effects in partially connected flow impose significant restrictions to the motion of the non-wetting phase due to the increased fluid-fluid interfacial line. It becomes evident that the higher fraction of small pores in the porous structures has a negative impact on the non-wetting phase relative permeability at large driving forces due to capillary pressure effects. For partially connected flow, the relative permeabilities of the non-wetting phase in structures 1 and 2

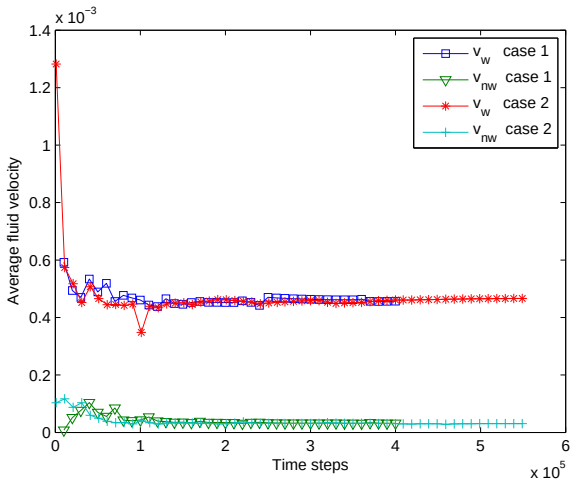

Figure 5.9: The average superficial velocity of the non-wetting and wetting phases as a function of the time-step for two cases with different initial uniform distributions; $S_{nw} = 0.6$, $G = 0.0000005$ and $M \approx 103$.

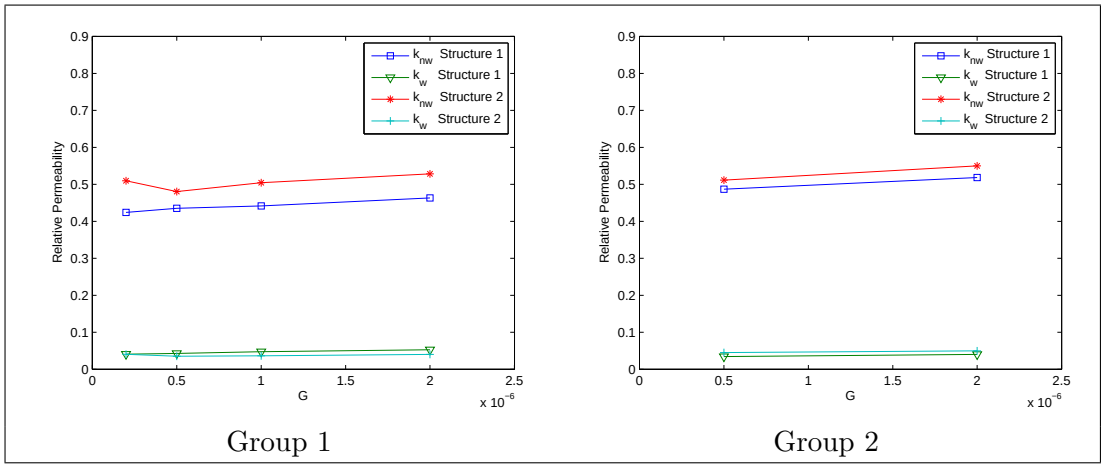

Figure 5.10: Relative permeabilities as a function of G in porous structures 1 and 2 of Groups 1 and 2; $S_{nw} = 0.6$.

of Group 1 are ≈ 0.45 and ≈ 0.5 respectively, whereas for structures 1 and 2 of Group 2 are ≈ 0.5 and ≈ 0.53 respectively. The previously mentioned values are an average approximation in the studied range of driving forces since all values show an increasing trend as the driving forces increase. This phenomenon can be also noticed in Fig. 5.11 where the capillary number for structure 2 is higher in both groups for the same level of driving forces. This comes in contrast with the observations in the fully connected regime, where the higher fraction of small pores has a significant negative impact only at low levels of driving forces by widening the non-linear region as described in section 5.3.1. However, at large driving forces, where the formation of new flow paths is nearly saturated and pressure can be transmitted uninterruptedly through the non-wetting

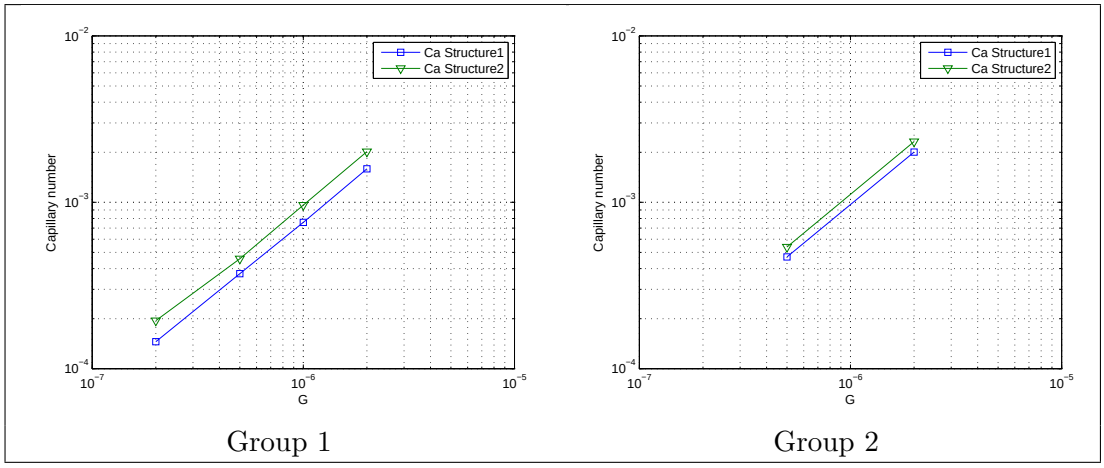

Figure 5.11: Capillary number against the driving force G for two-phase flow in porous structures 1 and 2 of Groups 1 and 2; $M \approx 103$ and $S_{nw} = 0.6$

fluid, the high fraction of small pores enhances the flow through the structure (i.e. pipe like flow).

5.3.2 Surface area effects

Geometrical properties

Two artificial porous media with different contour lengths and similar values of porosity and Euler characteristic are generated to investigate the effect of the contour length between the solid phase and the immiscible fluids. The pore size and cumulative distributions for structures 1 and 3 of both groups of Table. 5.1 are shown in Fig. 5.12. As shown in Fig. 5.12, the largest pore size for structure 1 is smaller than for structure 3 in each group. It is also shown that the number of occurrences of pore pixels located at pores with a size larger than 5 lattice units in structure 3 is higher than the corresponding number in structure 1. It can be concluded that the solid phase contour length has a direct impact not only on the pore size distribution, but also on the peak magnitudes of the pore volumes even at the same porosity values. The volume fraction occupied by small pores becomes larger with increasing contour length.

Fully connected flow

In order to investigate the effect of the solid phase contour length in two-phase flow in porous media, simulations at high saturations of the non-wetting phase (group 1: $S_{nw} = 0.85$, group 2: $S_{nw} = 0.9$, $M \approx 103$) at various levels of driving forces were performed in the artificial structures 1 and 3 for both groups of Table. 5.1. Fig. 5.13 shows the relative permeabilities as a function of the external forces G. As before, the relative permeabilities of the non-wetting phase in both media take values larger than unity at high driving forces. On the other hand, the relative permeabilities of

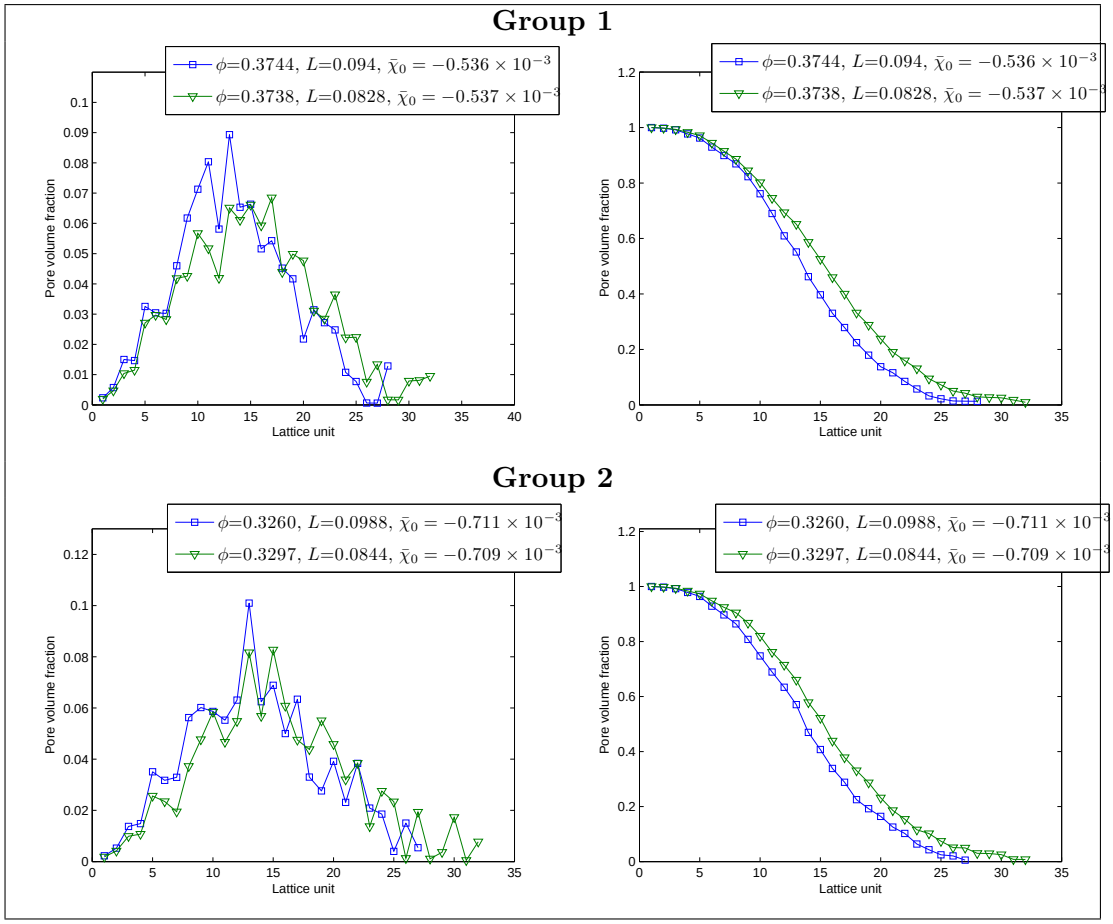

Figure 5.12: Pore size (left column) and cumulative (right column) distributions of porous structures 1 and 3 of Groups 1 and 2.

the wetting phase take values very close to zero. The flow rate through the structure becomes linear at high driving forces, while it displays a non-linear behaviour at low driving forces. It is evident that for structure 3 in each group, a lower pressure gradient is needed for the flow to reach the linear flow region compared with the two-phase flow in artificial structure 1. As shown in Fig. 5.12, the number of small pore sizes in structure 1 is higher than in structure 3. This is an additional indication that the required external force magnitude to reach the linear flow region is highly dependent on the pore size distribution. However, the corresponding relative permeabilities of the non-wetting phase are different from the previous case (i.e. effect of porosity). For both groups, the relative permeabilities of the non-wetting phase in structure 3 are greater than the relative permeabilities attained in structure 1 in the linear region. The discrepancy between the two cases is attributed to the different fluid-fluid interfacial lengths. Unlike the phase distributions in structures 1 and 2, where both have a similar fluid-fluid interfacial length (i.e. similar solid phase contour length), the length of the interface between the two phases in structure 3 is less than the length of the

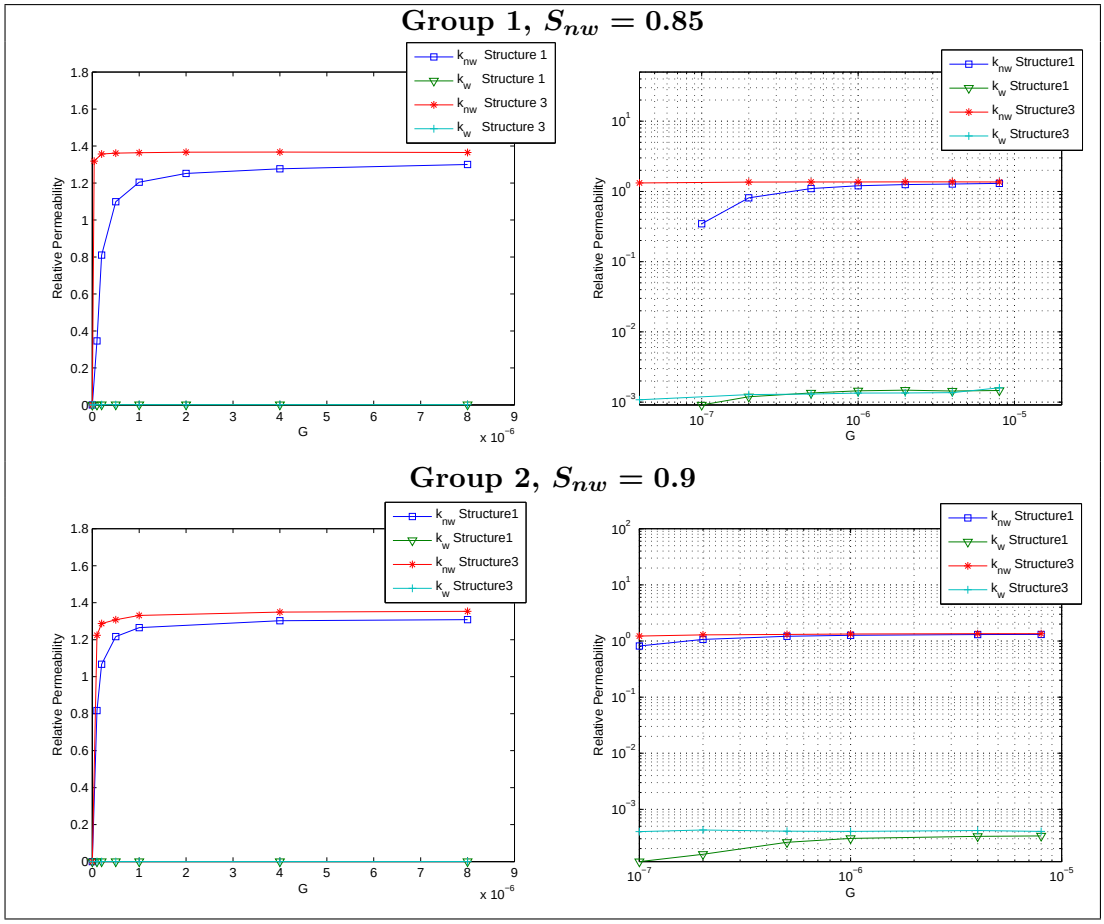

Figure 5.13: Normal (left column) and logarithmic (right column) plots of the relative permeabilities as a function of the driving force G for structures 1 and 3 of Groups 1 and 2.

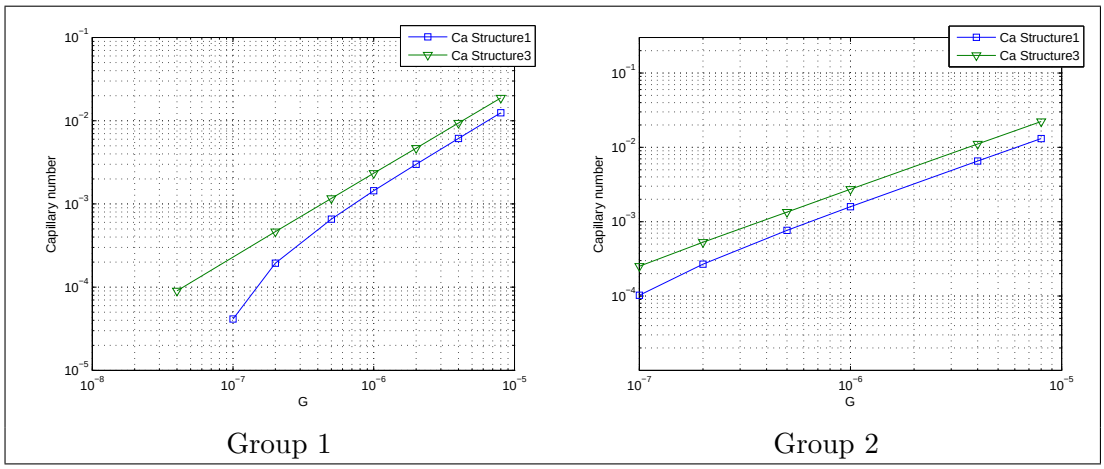

Figure 5.14: Capillary number as a function of G for two-phase flow in artificial structures 1 and 3 of Groups 1 and 2.

interface in structure 1 for both groups. The values of the fluid-fluid interfacial contour

Structure	Fully connected flow	Partially connected flow
Group 1		
1	0.0758	0.0465
3	0.067	0.0405
Group 2		
1	0.0869	0.0492
3	0.0763	0.0437

Table 5.2: Fluid-fluid interfacial contour lengths per unit pixel.

lengths for the different cases are given in Table. 5.2. It is evident that in the case of fully connected flow of the non-wetting phase, the contour length of the fluid-fluid interface depends on the the solid phase perimeter. In this specific case, the fluid-fluid interfacial contour length in structure 1 of both groups is higher than in structure 3. This eventually results in an increased viscous momentum exchange length between the two phases, resulting in an elongated shear flow path (i.e. higher resistance in the flow). Hence, for a given magnitude of the driving force, an increased fluid-fluid interfacial contour length in particular porous medium results in a reduced value at its linear region. Fig. 5.14 displays the relationship between the Capillary number with driving forces. In accordance with the observations regarding the non-wetting phase relative permeabilities, a wider non-linear region is observed at low driving forces for structure 1 which tends to diminish as the driving force is increased. In contrast with the effects of porosity, it can be observed that the Capillary number does not collapse onto a single curve when the porous structures possess different solid phase contour lengths. This indicates that the increased interfacial contour lengths result in lower non-wetting phase velocities in the porous medium at the same levels of driving forces.

Partially connected flow

The dependence of the partially connected flow of the non-wetting phase on the perimeter of the solid phase in porous media is also investigated. Fig. 5.15 illustrates the relative permeabilities of the wetting and non-wetting phases under high levels of driving forces and saturation of 60% for the non-wetting phase. The corresponding fluid-fluid interfacial lengths for the partially connected flow are also shown in Table. 5.2 and can be directly compared with the ones for the fully connected flow. The relative permeabilities of the non-wetting phase are higher for structure 3 which has a shorter perimeter of the solid phase. In addition, the effects of capillary forces and surface tension at the fluid-fluid interface on the non-wetting phase are more intense in structure 1 since it possesses a higher fraction of small pores and a longer fluid-fluid interfacial contour length. This has a direct effect on the relationship of the Capillary number of the

different structures with driving forces as it is clearly shown in Fig. 5.16. Hence, it can be concluded that porous structures of similar porosity and solid phase connectivity but with lower solid phase contour length will significantly aid the prevalence of the viscous forces over interfacial tension at the same magnitudes of driving forces.

5.3.3 Connectivity effects

Geometrical properties

The pore size and the corresponding cumulative distributions for structures 1 and 4 of groups 1 and 2 are shown in Fig. 5.17. Each pair has similar values of porosity and solid contour length, however different values of connectivity. It can be seen that the overall distribution of pore sizes as well as their peak sizes are similar for the two structures in each group. Looking at the cumulative pore size distribution, it is observed that the volume fraction of all pores with size larger or equal to 18 lu in structure 1 is greater than that in structure 4. The large pores in structure 4 are slightly smaller than those in structure 1. However, within the margin of numerical accuracy on the porosity and solid line contour length values, it can be concluded that the effect of connectivity on the pore size distribution can be safely ignored. This result indicates that the two phase flow observations will exclusively depend on the shape of the structure (i.e. the topological space).

Fully connected flow

Fig. 5.18 shows the relative permeabilities of the wetting and non-wetting phases in structure 1 and 4 of groups 1 and 2 as a function of the driving force G at high non-wetting fluid saturations (Group 1; $S_{nw} = 0.85$, Group 2; $S_{nw} = 0.9$) and dynamic viscosity ratio $M \approx 103$. Neglecting pore size distribution effects (i.e. similar in both

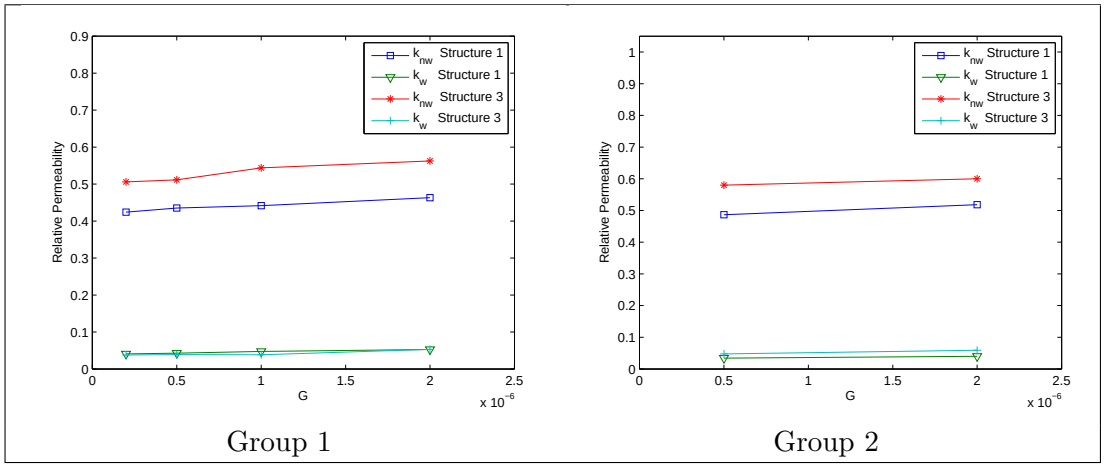

Figure 5.15: Relative permeabilities as a function of G in porous structures 1 and 3 of Groups 1 and 2; $S_{nw} = 0.6$.

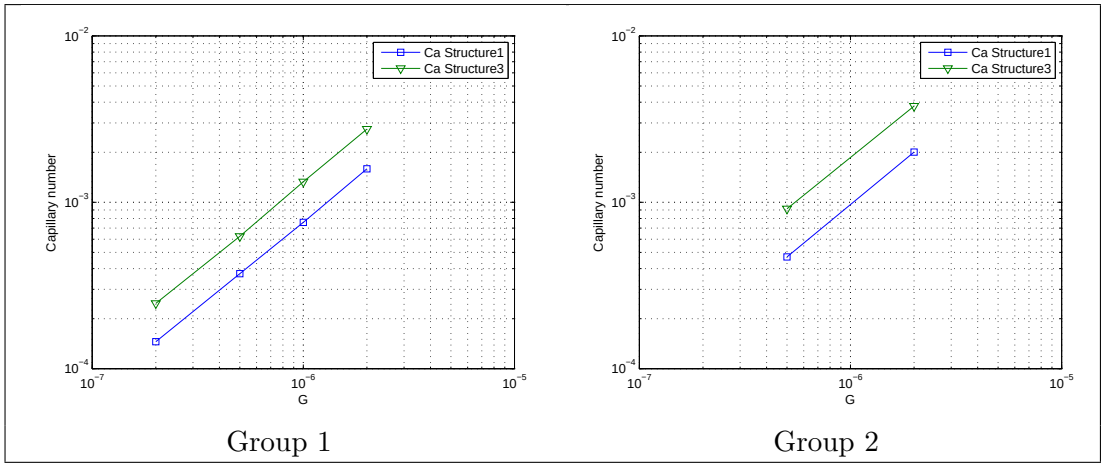

Figure 5.16: Capillary number against the driving force G for two-phase flow in porous structures 1 and 3 of Groups 1 and 2; $M \approx 103$ and $S_{nw} = 0.6$

structures from each group), it can be observed that the solid grain connectivity has a significant impact on the range of the driving force necessary to reach the linear flow region. More specifically, large values of the Euler characteristics imply a smaller number of solid clusters formed by isolated or overlapping grains. Considering similar levels of grains, a small number of solid clusters indicates a higher morphological complexity clusters in the porous structure. In this case, the larger value of the Euler characteristic of structure 1 in both groups results in a higher complexity structure as depicted in the magnified regions shown in Fig. 5.19. In the research of single phase flow through porous materials, Scholz et al. [152] pointed out that the clusters with complex morphology which are defined as extended clusters lead to tortuous streamlines and thus reduce the permeability of the porous medium. In the case of two-phase flow in porous media, the extended clusters will give rise to strong resistance to the non-wetting phase flow. The sharp corners tend to pin interfaces when the non-wetting phase attempts to penetrate into the pores. Thus, greater driving forces are needed to reach the linear region for structure 1 in each group, despite that the pore size distribution is similar to structure 4. In contrast to the curve of the non-linear region, the relative permeabilities in the linear region collapse onto a single curve with increasing driving forces. Both structures in each of group possess similar pore size distribution and fluid-fluid interfacial length. It can be concluded that the relative permeabilities of the non-wetting phase in the linear region depend only on the pore size distribution of the porous structure rather than the morphological characteristics of the conducting phase. The influence of the resistance on the non-wetting phase caused by interface pinning at the corner of external clusters disappear in the linear region as fully connected paths are constructed. As shown in Fig. 5.20 the Capillary number presents a non-linear behaviour at low driving forces, whereas a linear relationship is observed at

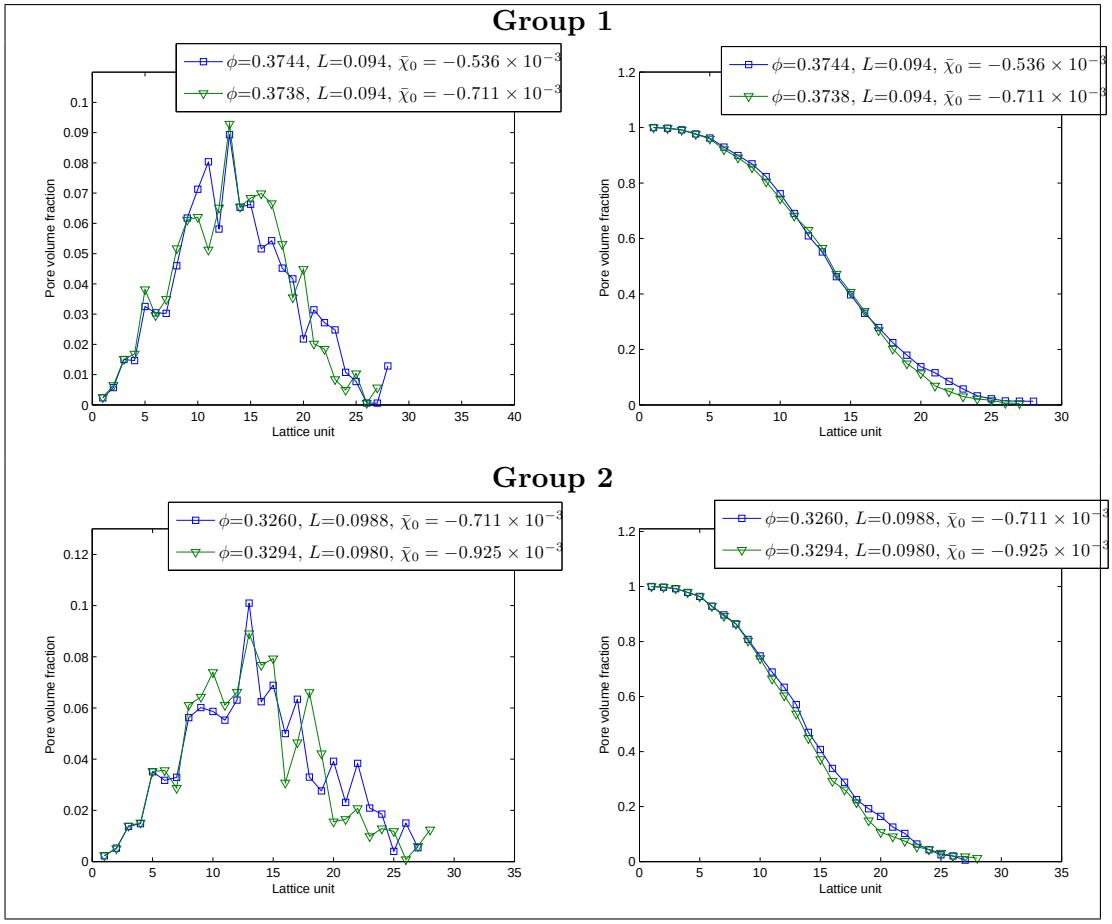

Figure 5.17: Pore size (left column) and cumulative (right column) distributions of porous structures 1 and 4 of Groups 1 and 2.

higher driving forces. Since the relative permeabilities of the two structures collapse onto a single curve at high driving forces, the deviation in their capillary numbers is attributed to their corresponding intrinsic permeabilities (i.e. lower for structure 1). Thus higher driving forces are needed to overcome resistance effects for structures with higher Euler characteristic, due to their increased morphological complexity which also lowers their intrinsic permeability.

Partially connected flow

Simulations have also been performed in structures 1 and 4 of Groups 1 and 2 at intermediate values of the non-wetting phase saturation ($S_{nw} = 0.6$ and $M \approx 103$) at high levels of driving forces. As shown in Fig. 5.21, the relative permeabilities of non-wetting phase are lower in structure 1 for both groups comparing with those in structure 4 which has a lower $\bar{\chi}_0$. This observation comes in contrast with the fully connected flow case in which the relative permeabilities collapse onto a single curve at higher levels of driving forces. The reason for the variance of the relative permeabilities

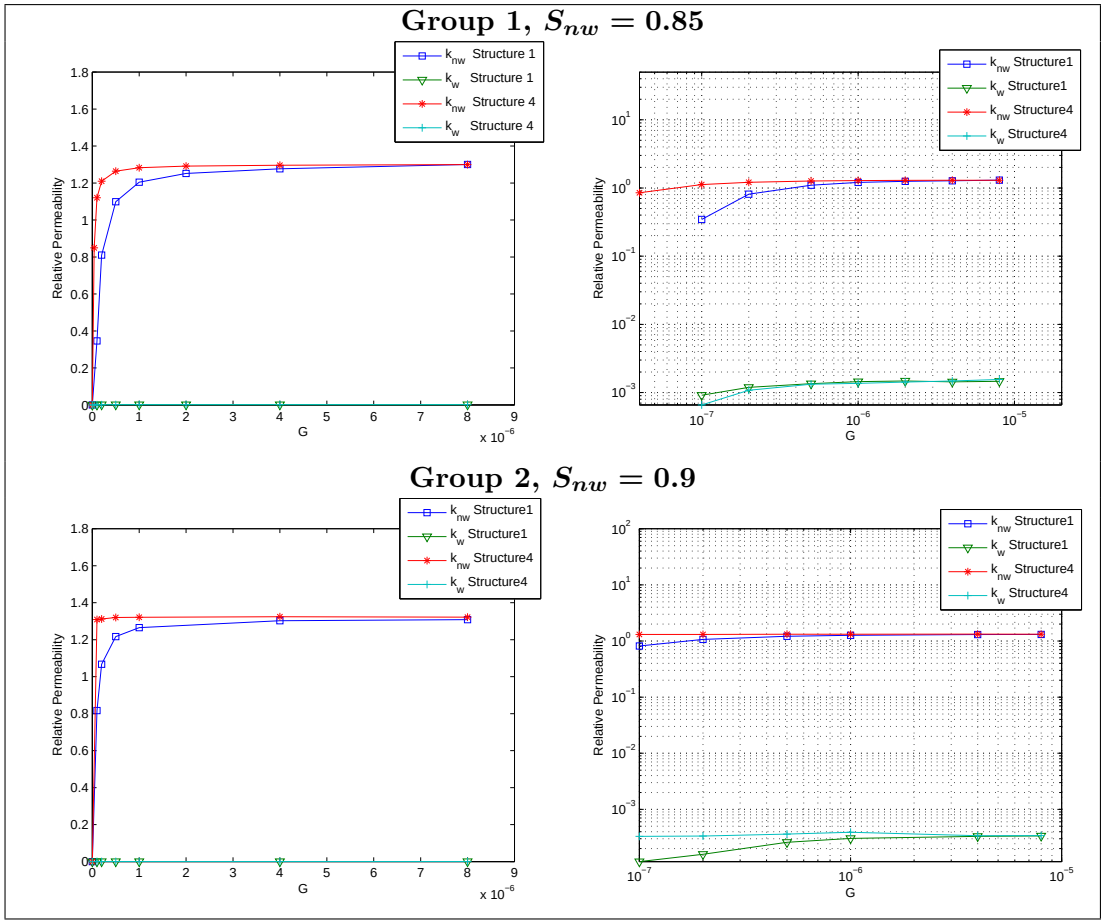

Figure 5.18: Normal (left column) and logarithmic (right column) plots of the relative permeabilities as a function of the driving force G for structures 1 and 4 of Groups 1 and 2.

of the non-wetting phase should be attributed to the existence of extended clusters with complex morphology in structure 1, since the pore size distribution and solid contour length are similar. The resistance effect formed by the interface penetration into the pores constructed with sharp and concave bulge cannot be neglected for the partially connected flow of the non-wetting phase. Thus, it can be concluded that the relative permeabilities of the non-wetting phase are higher for the porous media with lower Euler characteristic of the conducting phase $\bar{\chi}_0$ in the linear region. Ahmadlouydarab et al. [123] has also observed that sharp corners tend to reduce the k_{nw} in relation to the rounded geometry in the study of two-phase flow through corrugated tubes. This effect is also reflected in Fig. 5.22, where significantly lower Capillary numbers are observed for structure 1 due to the combined effects of reduced intrinsic permeability and non-wetting phase relative permeability.

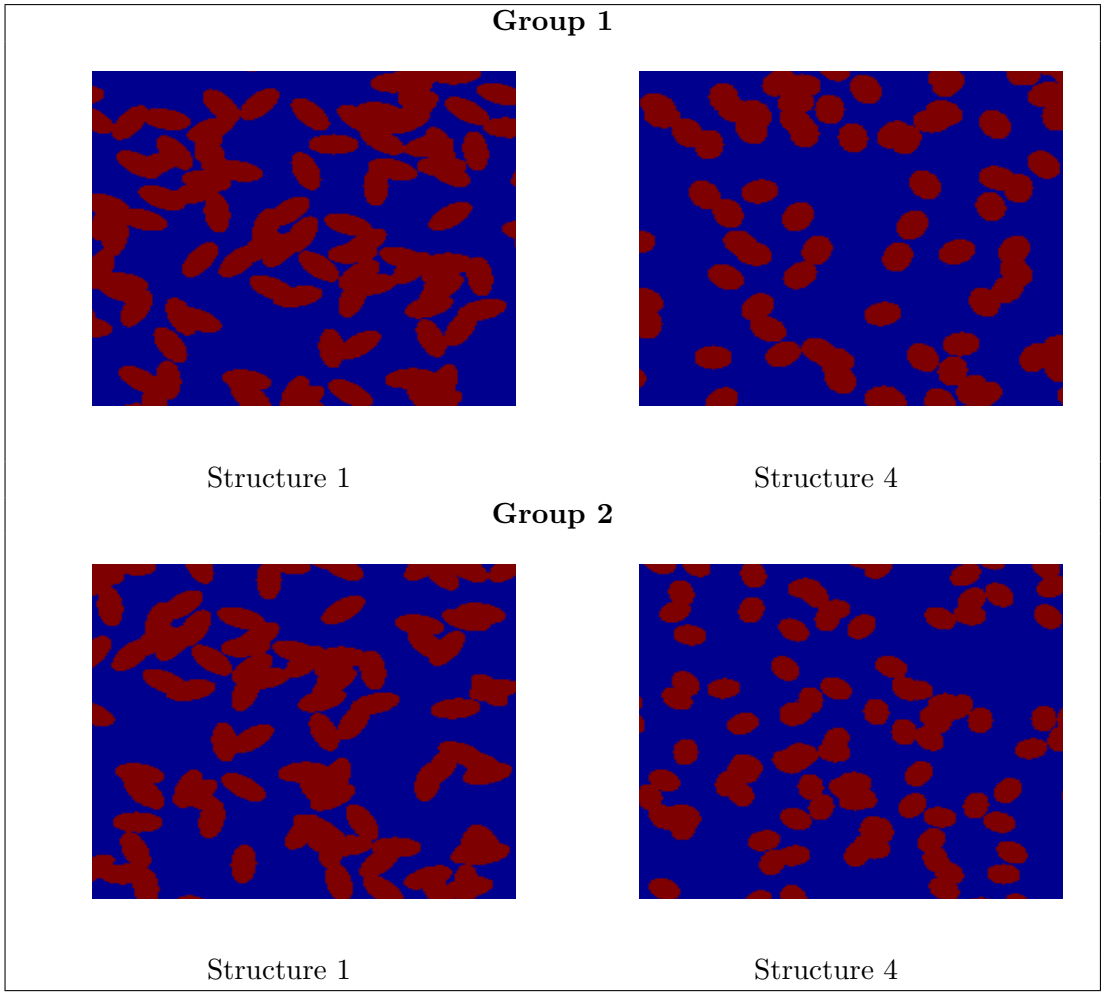

Figure 5.19: Magnified regions of structures 1 and 4 of Groups 1 and 2.

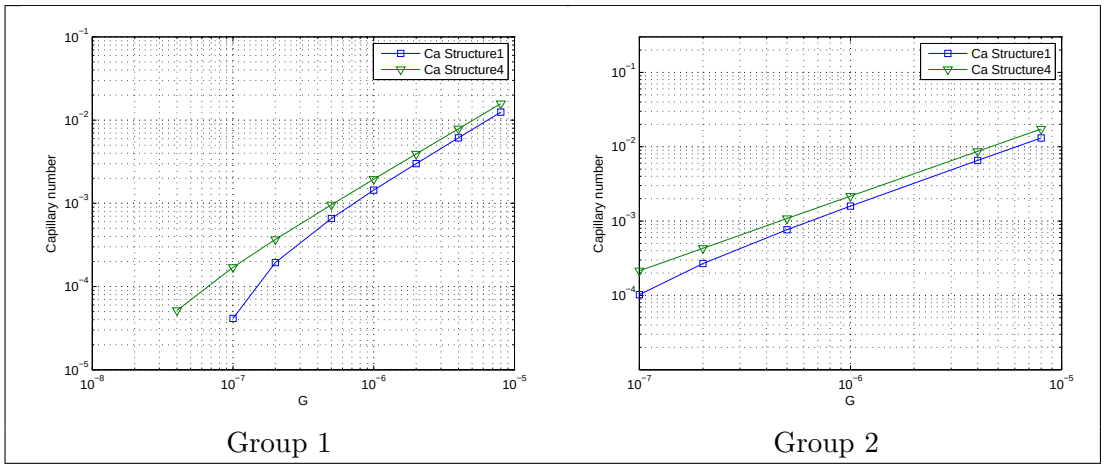

Figure 5.20: Capillary number against the driving force G for two-phase flow in porous structures 1 and 4 of Group 1 and 2.

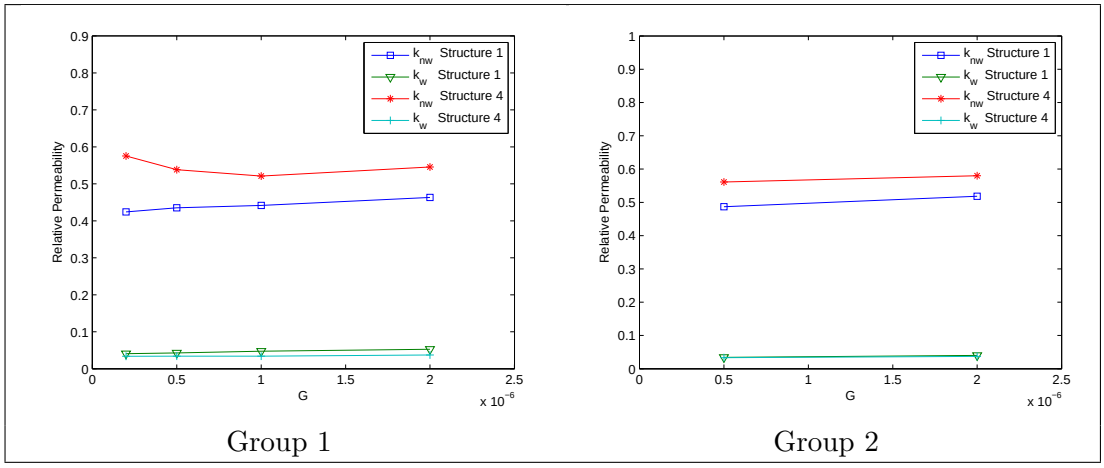

Figure 5.21: Relative permeabilities as a function of G in porous structures 1 and 4 of Groups 1 and 2; $S_{nw} = 0.6$.

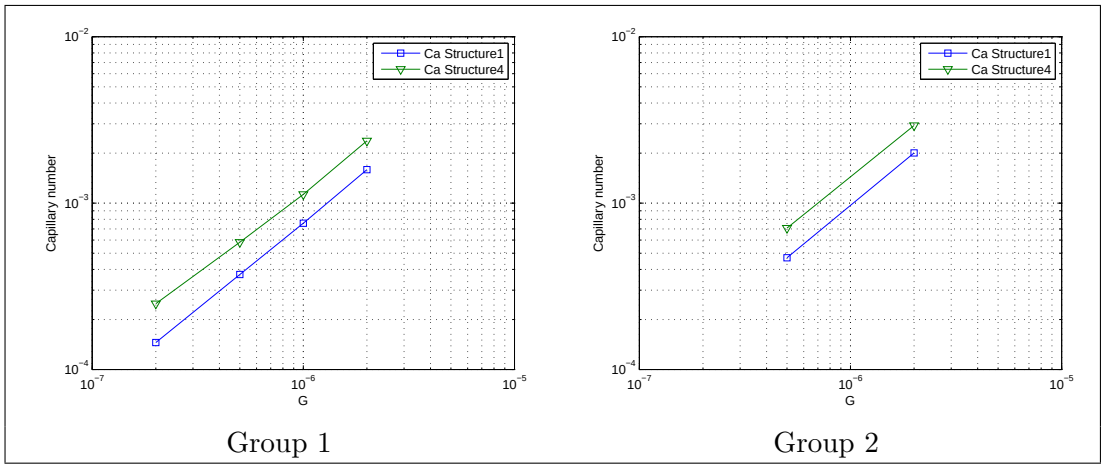

Figure 5.22: Capillary number against the driving force G for two-phase flow in porous structures 1 and 4 of Groups 1 and 2; $M \approx 103$ and $S_{nw} = 0.6$

5.3.4 Conclusions

In the present work, the effect of the geometrical properties of 2D porous media on the relative permeabilities of the non-wetting phase for steady-state immiscible two-phase flows was investigated. The simulations have been performed for various saturations of the non-wetting phase using a two-dimensional MRT LBM which can tolerate high density ratios. Two groups of four artificial porous structures with different Minkowski functionals were generated with a Boolean model based on a random distribution of overlapping ellipses/circles. The pore size distributions of each artificial structure was computed. As expected, a higher fraction of small pores was found in the porous structures with longer solid phase contour length and higher solid phase fraction. It was shown that the relative permeability of the non-wetting phase, k_{nw}, is much more sen-

sitive to the geometric properties of the porous media than the relative permeability of the wetting phase, k_w, for the cases of fully connected flow ($S_{nw} = 0.85$ and $S_{nw} = 0.9$) and partially connected flow ($S_{nw} = 0.6$).

In the case of fully connected flow, it was found that the flow rate of the non-wetting fluid and the driving force exhibit highly non-linear relations at low force magnitudes, while the relative permeabilities are almost constant, something that indicates linear flows, when the driving forces were increased. It became clear that the external force needed to reach the linear flow region is highly dependent on the pore size distribution and solid phase connectivity of the porous structure. As the fraction of small pores and the Euler characteristic of the conducting phase $\bar{\chi}_0$ increases, the required external force needed to reach the linear flow region also increases. The non-wetting phase can be treated as a pipe flow once the linear region is reached, in which case the influence of capillary pressure becomes negligible. This was found to give rise to increased non-wetting phase relative permeabilities when porosity is the varied parameter (i.e. higher with increasing fraction of small pores), whilst they were found to collapse onto a single curve when the Euler characteristic (i.e. connectivity) was altered. On the other hand, lower values were observed for porous structures that present larger solid phase contour length.

At intermediate values of the non-wetting phase saturation (partially connected flow), it was shown that the relative permeabilities are significantly reduced as the fraction of small pores, the solid phase/interfacial contour length and Euler characteristic (higher morphological complexity) increase. It was observed that capillary pressure effects become more significant as the fraction of small pores increases. Increased solid phase contour length gives rise to an increased fluid-fluid interfacial length, which also affects the relative permeabilities in a negative way. In addition, a larger value of the Euler characteristic, implying a porous structure with higher morphological complexity, was found to reduce the values of the non-wetting phase relative permeability. This phenomenon was attributed to the resistance caused by the interface penetration into the pores shaped with sharp and concave bulges.

Chapter 6

Conclusions

6.1 Research summary & conclusions

The primary motivation for the current research is to develop a numerical model that will be able to simulate multi-phase flows in porous media. Traditional CFD methods are not suitable for pore scale simulations in porous media due to their inevitable geometrical complexities. It is also a huge challenge for the continuum models to capture topological changes in the interface between wetting and non-wetting phase. As a mesoscopic method, the pseudopotential lattice Boltzmann model has native advantages to treat the multiphase flow in the complex systems without the need to trace the interfaces between different phases. Hence, the pseudo-potential LB model was chosen as the numerical model in current research. The research start from studying the process of droplet impingement onto flat surface and single cylinder as most of artificial packed porous media is composed of union set of grains with different shapes. The understanding of the dynamic behaviour of the dynamic behavior of liquid droplet on the solid phase will be useful and valuable in the efficient design and optimization for the types of structured packing of artificial porous structure. Especially in large-ganlion dynamics regime, the non-wetting phase is totally disconnected in the form of ganglia. The study on the dynamic behavior of non-wetting phase blob depending on the solid phase with different shape and different wettability is significative. Furthermore, in order to overcome the limitation of low density ratio between two phases and instability with a relaxation time τ less than 1 for the pesudopotential model, an improved force scheme is proposed for the three-dimensional multi-relaxation time pseudopotential lattice Boltzmann model. The investigation on the immiscible two phases flow in porous media is carried out by the multi-relaxation time (MRT) lattice Boltzmann model. Two groups including eight artificial structures with given values of the specific global Minkowski functionals are generated by a Boolean model based on a random distribution of overlapping ellipases/circles. An additional MATLAB code is developed to measure the pore size distributions for every porous structure. The effects of geometrical properties of pore structure on the pore size distribution, as well as the

immiscible two-phase flows in porous media are revealed.
As it is mentioned in the chapter 2, most of the LBM studies on the droplet impingement onto solid surfaces and the immiscible two phases in porous media are limited to low density ratio between two phases and instability with a relaxation time τ less than 1. In addition, previous numerical works on the immiscible two phase flows in porous media focus on the influence of the properties of liquids, such as capillary number, wetting angle and viscosity ratio, while few previous publications revealed the effect of the packed structure on the multi-phase flow in porous media. The understanding of the effect of the properties of porous structures on the multi-phase flow has great significance for industrial operations such as, enhanced oil recovery, geologic CO_2 sequestration, catalytic processing in trick bed reactors. In current study, the process of liquid droplet impact onto solid phase is investigated by 2-dimensional and 3-dimensional lattice Boltzmann model which can tolerate the high density ratio between two phases. The simulations support the information about the influence of Reynolds number, Weber number, Ohnesorge number and the target-to-drop size ratio on the impingement process. Moreover, an improved force scheme is proposed for the three-dimensional MRT pseudopotential lattice Boltzmann model which can simulate the multi-phase flow with large density ratio and low kinematic viscosity. The immiscible two phases flow in porous media is simulated by a MRT lattice Boltzmann model. The properties of porous structures is decided by the global Minkowski functionals which can be controlled by a Boolean process. So, the pore structure is characterized and the relation between relative permeability with pore structure is constructed.
The study showed in section 3.3, that in order to handle multi-phase flows at high density ratios and low viscosities in a efficient way, an improved force scheme is proposed for the three-dimensional multi-relaxation time (MRT) pseudopotential lattice Boltzmann model based on the improved force scheme for the single relaxation time (SRT) pseudopotential lattice Botlzmann model [60] and the Chapman-Enskog analysis [141]. The 3-dimensional MRT lattice Boltzmann model is validated through following aspects.

- The satisfaction of Laplace law.
- Thermodynamic consistency verified.
- The contact angle is a linear function of fluid-solid interaction potential parameter G_w.

In the chapter 4, lattice Boltzmann model was applied on studying the impaction of a liquid droplet on a dry flat surface and a cylindrical surface for a liquid-gas system with large density ratio and low viscosity. The dynamics behavior of droplet impact on a flat surface was discussed in section 4.1.

- There are four phases during the droplet impact on flat surface including the

kinematic phase, the spreading phase, the relaxation phase and the equilibrium phase.

- In the kinematic phase, the droplet spread factor depend on the non-dimensional time rather than the physical properties.
- In the spreading phase, the maximum spread factor increases with increasing inertia.
- In the spreading phase, the maximum diameter and the time needed to reach the maximum diameter are decided by the inertia for given Ohnesorge number.
- In the relaxation phase, the wettability of the surface becomes significant.
- In the equilibrium phase, the time reaches the equilibrium shape is controlled by Weber and Reynolds number.

In section 4.2. the liquid droplet impact on a cylindrical surface were modeled. It is found:

- There are three distinct temporal phases of the film dynamics.
- In the first phase, the non-dimensional film thickness follows the correlation given by $h^\star = 1 - t^\star$.
- In the second phase, the inertia dominates the viscous forces, the non-dimensional film thickness follows the correlation given by $h^\star = 0.33/(t^\star)^{0.9}$.
- In the third phase, the film thickness increases under the action of the interfacial tension and reaches a constant value at last.
- In the first and second phases, the non-dimensional time and film thickness curve collapses onto a single curve for different values of Reynolds number.
- In the second phase, the influence of the viscous force cannot be neglected for the low Reynolds number case.
- In the second phase, the influence of gravity appears with increasing Galilei number.
- In the first phase, the effect of surface tension can be neglected, while the surface tension dominates the inertial force at the end of the second phase.

In section 4.3, the dynamics behaviour for the droplet impact onto the cylinder from 45° with horizon was modeled, as well as the effects of surface characteristics and impact velocity on the dynamic behavior were investigated. From the simulation study, it can be concluded that:

- The contact line between liquid and solid surface on hydrophilic wall is longer than for hydrophobic surface.
- The kinetic energy dissipated on hydrophilic wall is higher than on hydrophobic surface.
- Droplet breakup will happen as increasing the initial kinetic energy.
- Hydrophilic surface can assist in averting the surface droplet breakup during the impacting process.

The study on the immiscible tow-phase flows in porous media was shown in chapter 5. The studies were focused on the effect of properties of porous structure on relative permeability for both two phases which can be of great help to the for industrial operations such as, enhanced oil recovery, geologic CO_2 sequestration, catalytic processing in trick bed reactors. In the case of high value of the non-wetting phase saturation, it is found:

- The flow rate of the non-wetting fluid and the driving force exhibit highly non-linear relations at low force at low magnitude of driving force, the relative permeabilities will reach a constant value with increasing driving force.
- The external force needed to reach the linear flow region is dependent on the pore size distribution and solid phase connectivity of the porous structure.
- In linear region, then non-wetting phase relative permeabilities increase with increasing fraction of small pores of porous media.
- In the linear region, the non-wetting phase relative permeabilities are not dependent on the Euler characteristic.

In the case of intermediate values of the non-wetting phase saturation, it is found that:

- The relative permeabilities are significantly reduced as the fraction of small pores, the solid phase/interfacial contour length and Euler characteristic increase.

6.2 Recommendations for future work

The current study was focused on the development of a lattice Boltzmann model to simulate the droplet impact onto solid substrates, as well as the immiscible two-phase flows in porous media. Due to the demands of the current research, a great amount of time was spent on the development of code and model. A substantial amount of work is still needed for a complete description of immiscible two phase flows. Additional recommendations for future work are proposed from three different aspects.
Firstly, it is important to continue the development of the current lattice Boltzmann

model to include heat transfer and reaction between different phases in order to make the model applicable to the chemical process equipment such as trickle beds reactor etc. It is required that the researcher has a good knowledge of lattice Boltzmann model and appropriate experience in numerical analysis or applied mathematics to achieve this objective.

Also, several studies could be performed regarding the effect of properties of porous structures on the immiscible two-phase flows in porous media. The work should include the effect of geometrical properties characterized by global Minkowski functionals on the process of displacement and imbibition, as well as the cluster size distribution for the non-wetting phase. The final objective is a quantitative relation between pore structure and relative permeability which could be achieved for two-phase flow in porous media. The difficulty of such a task is that advanced knowledge of two-phase flow in porous media is required by the researcher as well as the mathematical framework to generated the various porous structures. In addition, our current work about the two-phase flow in porous media was limited in 2-dimensional studies due to the much higher computational cost of a 3-dimensional study. We expect that the current study be extended to three dimensions.

Finally, there is a recommendation for further development of the code. It is required to speed up the simulations, especially for the two-phase flow in porous media with large three dimensional domain. The code should be further developed based on parallel computing or GPU accelerated computing. Advanced programming abilities are necessary for the researcher and the cooperation with computer science students may be a necessity.

Appendix A

Derivation of there-dimensional macroscopic equations for D3Q19 model

Introducing the expansions [153]

$$f_\alpha(\boldsymbol{x}+\boldsymbol{e}_\alpha\delta t, t+\delta t)=\sum_{n=0}^{\infty}\frac{\beta^n}{n!}D_{t_n}^n f_\alpha(\boldsymbol{x},t), \tag{A.1}$$

$$D_{t_n}\equiv\partial_{t_n}+e_{\alpha k}\partial_k, \tag{A.2}$$

$$f_\alpha=\sum_{n=0}^{\infty}\beta^n f_\alpha^{(n)}, \tag{A.3}$$

$$\partial_t=\sum_{n=0}^{\infty}\beta^n\partial_{t_n}, \tag{A.4}$$

where $\beta=\delta_t$, Appling the expansions in Eq. (A.1) to Eq. (A.4) to Eq. (3.35), the following relationship for the zeroth, first and second-order of the parameter β are obtained:

$$f_\alpha^{(0)}=f_\alpha^{eq}, \tag{A.5}$$

$$D_{t_0}f_\alpha^{(0)}=-\sum_\beta\Omega_{\alpha\beta}f_\beta^{(1)}+S_\alpha, \tag{A.6}$$

$$\partial_{t_1}f_\alpha^{(0)}+D_{t_0}(I_{\alpha\beta}-\frac{1}{2}\Omega)f_\beta^{(1)}=-\sum_\beta\Omega_{\alpha\beta}f_\beta^{(2)}, \tag{A.7}$$

These can be easily converted into moment space by multiplying Eqs. A.5-A.7 by the transformation matrix $\boldsymbol{M}$,

$$\boldsymbol{m}^{(0)}=\boldsymbol{m}^{eq}, \tag{A.8}$$

$$(\partial_{t_0}+\boldsymbol{\zeta}_i\partial_i)\boldsymbol{m}^{(0)}=-\boldsymbol{\Lambda}\boldsymbol{m}^{(1)}+\bar{\boldsymbol{S}} \tag{A.9}$$

$$\partial_{t_1}\boldsymbol{m}^{(0)}+(\partial_{t_0}+\boldsymbol{\zeta}_i\partial_i)(\boldsymbol{I}-\frac{1}{2}\boldsymbol{\Lambda})\boldsymbol{m}^{(1)}=-\boldsymbol{\Lambda}\boldsymbol{m}^{(2)}, \tag{A.10}$$

where $\boldsymbol{\zeta} = \boldsymbol{M} e_{\alpha_i} \boldsymbol{M}^{-1}$. The components of the first-order equations in moment space are obtained from Eq. A.9, Eq. 3.43 and Eq. 3.54,

$$\partial_{t_0}\rho + \partial x j_x + \partial_y j_y + \partial_z j_z = 0, \tag{A.11}$$

$$\partial t_0(-11\rho + 19\frac{j_x^2 + j_y^2 + j_z^2}{\rho}) + \partial x(\frac{5}{3}j_x) + \partial y(\frac{5}{3}j_y) + \partial z(\frac{5}{3}j_z) = -s_2 e^{(1)} + 38(\boldsymbol{u}\cdot\boldsymbol{F}) + \frac{114\epsilon \boldsymbol{F}^2}{\psi^2(1/s_2 - 0.5)}, \tag{A.12}$$

$$\partial t_0(3\rho - \frac{11}{2}\frac{j_x^2 + j_y^2 + j_z^2}{\rho}) + \partial x(-\frac{2}{3}j_x) + \partial y(-\frac{2}{3}j_y) + \partial z(-\frac{2}{3}j_z) = -s_3 {e^{(1)}}^2 - 11(\boldsymbol{u}\cdot\boldsymbol{F}), \tag{A.13}$$

$$\partial t_0(j_x) + \partial x(\frac{1}{3}\rho + \frac{{j_x}^2}{\rho}) + \partial y(\frac{j_x j_y}{\rho}) + \partial z(\frac{j_x j_z}{\rho}) = F_x, \tag{A.14}$$

$$\partial t_0(-\frac{2}{3}j_x) + \partial x(-\frac{2}{9}\rho + \frac{-4{j_x}^2 + 5{j_y}^2 + 5{j_z}^2}{6\rho}) + \partial y(\frac{j_x j_y}{\rho}) + \partial z(\frac{j_x j_z}{\rho}) = -s_5 {q_x}^{(1)} - \frac{2}{3}F_x, \tag{A.15}$$

$$\partial t_0(j_y) + \partial x(\frac{j_x j_y}{\rho}) + \partial y(\frac{1}{3}\rho + \frac{{j_y}^2}{\rho}) + \partial z(\frac{j_y j_z}{\rho}) = F_y, \tag{A.16}$$

$$\partial t_0(-\frac{2}{3}j_y) + \partial x(\frac{j_x j_y}{\rho}) + \partial y(-\frac{2}{9}\rho + \frac{5{j_x}^2 - 4{j_y}^2 + 5{j_z}^2}{6\rho}) + \partial z(\frac{j_y j_z}{\rho}) = -s_7 {q_y}^{(1)} - \frac{2}{3}F_y, \tag{A.17}$$

$$\partial t_0(j_z) + \partial x(\frac{j_x j_z}{\rho}) + \partial y(\frac{j_y j_z}{\rho}) + \partial z(\frac{1}{3}\rho + \frac{{j_z}^2}{\rho}) = F_z, \tag{A.18}$$

$$\partial t_0(-\frac{2}{3}j_z) + \partial x(\frac{j_x j_z}{\rho}) + \partial y(\frac{j_y j_z}{\rho}) + \partial z(-\frac{2}{9}\rho + \frac{5{j_x}^2 + 5{j_y}^2 - 4{j_z}^2}{6\rho}) = -s_9 {q_z}^{(1)} - \frac{2}{3}F_z, \tag{A.19}$$

$$\partial t_0(\frac{2{j_x}^2 - {j_y}^2 - {j_z}^2}{\rho}) + \partial x(\frac{4}{3}j_x) + \partial y(-\frac{2}{3}j_y) + \partial z(-\frac{2}{3}j_z) = -s_{10} 3{p_{xx}}^{(1)} + 2(2u_x F_x - u_y F_y - u_z F_z), \tag{A.20}$$

$$\partial t_0(-\frac{1}{2}\frac{2{j_x}^2 - {j_y}^2 - {j_z}^2}{\rho}) + \partial x(-\frac{2}{3}j_x) + \partial y(\frac{1}{3}j_y) + \partial z(\frac{1}{3}j_z) = -s_{11} 3{\pi_{xx}}^{(1)} + 2(-2u_x F_x + u_y F_y + u_z F_z), \tag{A.21}$$

$$\partial t_0(\frac{{j_y}^2 - {j_z}^2}{\rho}) + \partial y(\frac{2}{3}j_y) + \partial z(-\frac{2}{3}j_z) = -s_{12} {p_{ww}}^{(1)} + 2(u_y F_y - u_z F_z), \tag{A.22}$$

$$\partial t_0(-\frac{1}{2}\frac{{j_y}^2 - {j_z}^2}{\rho}) + \partial y(-\frac{1}{3}j_y) + \partial z(\frac{1}{3}j_z) = -s_{13} {\pi_{ww}}^{(1)} + (-u_y F_y + u_z F_z), \tag{A.23}$$

$$\partial t_0(\frac{j_x j_y}{\rho}) + \partial x(\frac{1}{3}j_y) + \partial y(\frac{1}{3}j_x) = -s_{14} {p_{xy}}^{(1)} + (u_y F_x + u_x F_y), \tag{A.24}$$

$$\partial t_0(\frac{j_y j_z}{\rho}) + \partial y(\frac{1}{3}j_z) + \partial z(\frac{1}{3}j_y) = -s_{15} {p_{yz}}^{(1)} + (u_z F_y + u_y F_z), \tag{A.25}$$

$$\partial t_0(\frac{j_x j_z}{\rho}) + \partial x(\frac{1}{3}j_z) + \partial z(\frac{1}{3}j_x) = -s_{16} {p_{xz}}^{(1)} + (u_z F_x + u_x F_z), \tag{A.26}$$

$$\partial x(\frac{1}{2}\frac{{j_y}^2 - {j_z}^2}{\rho}) + \partial y(\frac{j_x j_y}{\rho}) + \partial z(-\frac{j_x j_z}{\rho}) = -s_{17} {m_x}^{(1)}, \tag{A.27}$$

$$\partial x(-\frac{j_x j_y}{\rho}) + \partial y(\frac{1}{2}\frac{-{j_x}^2 + {j_z}^2}{\rho}) + \partial z(\frac{j_y j_z}{\rho}) = -s_{18} {m_y}^{(1)}, \tag{A.28}$$

$$\partial x(-\frac{j_x j_z}{\rho}) + \partial y(-\frac{j_y j_z}{\rho}) + \partial z(\frac{1}{2}\frac{{j_x}^2 - {j_y}^2}{\rho}) = -s_{19}{m_z}^{(1)}, \tag{A.29}$$

The second order equations of the conserved moments from the components of the second-order equations in moment space are derived from Eq. (A.10),

$$\partial t_1 \rho = 0, \tag{A.30}$$

$$\partial t_1(j_x)+\partial x[\frac{1}{57}(1-\frac{1}{2}s_2)e^{(1)}+\frac{1}{3}(1-\frac{1}{2}s_{10})3{p_{xx}}^{(1)}]+\partial y[(1-\frac{1}{2}s_{14}){p_{xy}}^{(1)}]+\partial z[(1-\frac{1}{2}s_{16}){p_{xz}}^{(1)}] = 0, \tag{A.31}$$

$$\begin{aligned}\partial t_1(j_y) + \partial x[(1 - \frac{1}{2}s_{14}){p_{xy}}^{(1)}] + \partial y[\frac{1}{57}(1 - \frac{1}{2}s_2)e^{(1)} - \frac{1}{6}(1 - \frac{1}{2}s_{10})3{p_{xx}}^{(1)} + \frac{1}{2}(1 - \frac{1}{2}s_{12}){p_{ww}}^{(1)}] \\ +\partial z[(1 - \frac{1}{2}s_{15}){p_{yz}}^{(1)}] = 0,\end{aligned} \tag{A.32}$$

$$\begin{aligned}\partial t_1(j_z) + \partial x[(1 - \frac{1}{2}s_{16}){p_{xz}}^{(1)}] + \partial y[(1 - \frac{1}{2}s_{15}){p_{yz}}^{(1)}] \\ +\partial z[\frac{1}{57}(1 - \frac{1}{2}s_2)e^{(1)} - \frac{1}{6}(1 - \frac{1}{2}s_{10})3{p_{xx}}^{(1)} - \frac{1}{2}(1 - \frac{1}{2}s_{12}){p_{ww}}^{(1)}] = 0,\end{aligned} \tag{A.33}$$

Combining the first and second order equations for the conserved moments by using $\partial_t = \partial_{t_0} + \beta\partial_{t_1}$, i.e. Eqs. (A.11) and (A.30), Eqs. (A.14) and (A.31), Eqs. (A.16) and (A.32) and Eqs. (A.18) and (A.33), we get

$$\partial t\rho + \partial x j_x + \partial y j_y + \partial z j_z = 0, \tag{A.34}$$

$$\begin{aligned}\partial t(j_x) + \partial x[(\frac{1}{3}\rho + \frac{{j_x}^2}{\rho}) + \frac{1}{57}\beta(1 - \frac{1}{2}s_2)e^{(1)} + \beta(1 - \frac{1}{2}s_{10}){p_{xx}}^{(1)}] \\ +\partial y[\frac{j_x j_y}{\rho} + \beta(1 - \frac{1}{2}s_{14}){p_{xy}}^{(1)}] + \partial z[\ + \beta(1 - \frac{1}{2}s_{16}){p_{xz}}^{(1)}] = F_x,\end{aligned} \tag{A.35}$$

$$\begin{aligned}\partial t(j_y) + \partial x[\frac{j_x j_y}{\rho} + \beta(1 - \frac{1}{2}s_{14}){p_{xy}}^{(1)}] + \partial y[(\frac{1}{3}\rho + \frac{{j_y}^2}{\rho}) + \frac{1}{57}\beta(1 - \frac{1}{2}s_2)e^{(1)} - \frac{1}{2}(1 - \frac{1}{2}s_{10})\beta{p_{xx}}^{(1)} \\ +\frac{1}{2}(1 - \frac{1}{2}s_{12})\beta{p_{ww}}^{(1)}] + \partial z[\beta(1 - \frac{1}{2}s_{15}){p_{yz}}^{(1)} + \frac{j_y j_z}{\rho}] = F_y,\end{aligned} \tag{A.36}$$

$$\begin{aligned}\partial t(j_z) + \partial x[\frac{j_x j_z}{\rho} + \beta(1 - \frac{1}{2}s_{16}){p_{xz}}^{(1)}] + \partial y[\frac{j_y j_z}{\rho} + \beta(1 - \frac{1}{2}s_{15}){p_{yz}}^{(1)}] \\ +\partial z[(\frac{1}{3}\rho + \frac{{j_z}^2}{\rho}) + \frac{1}{57}\beta(1 - \frac{1}{2}s_2)e^{(1)} - \frac{1}{2}(1 - \frac{1}{2}s_{10}){p_{xx}}^{(1)} - \frac{1}{2}\beta(1 - \frac{1}{2}s_{12}){p_{ww}}^{(1)}] = F_z,\end{aligned} \tag{A.37}$$

${p_{xx}}^{(1)}$, ${p_{ww}}^{(1)}$, ${p_{xy}}^{(1)}$, ${p_{xz}}^{(1)}$, ${p_{yz}}^{(1)}$, $e^{(1)}$ are unknown and can be obtained from Eq. (A.12), Eq. (A.20), Eq. (A.22), Eq. (A.24), Eq. (A.25) and Eq. (A.26),

$$e^{(1)} = \frac{1}{s_2}[-\frac{38}{3}(\partial x j_x + \partial y j_y + \partial z j_z) + \frac{114\epsilon \boldsymbol{F}^2}{\psi^2(1/s_2 - 0.5)}], \tag{A.38}$$

$${p_{xx}}^{(1)} = \frac{1}{3s_{10}}[-\frac{2}{3}(2\partial x j_x - \partial y j_y - \partial z j_z)], \tag{A.39}$$

$$p_{ww}{}^{(1)} = \frac{1}{s_{12}}[-\frac{2}{3}(\partial y j_y - \partial z j_z)], \tag{A.40}$$

$$p_{xy}{}^{(1)} = \frac{1}{s_{14}}[-\frac{1}{3}(\partial x j_y) + \partial y j_x], \tag{A.41}$$

$$p_{yz}{}^{(1)} = \frac{1}{s_{15}}[-\frac{1}{3}(\partial y j_z + \partial z j_y)], \tag{A.42}$$

$$p_{xz}{}^{(1)} = \frac{1}{s_{16}}[-\frac{1}{3}(\partial x j_z + \partial z j_x)], \tag{A.43}$$

where $\boldsymbol{F} = -Gc^2[\Psi\nabla\Psi + \frac{1}{6}c^2\Psi\nabla(\nabla^2\Psi) + \cdots]$, Using Eqs. (A.38) to (A.43) in Eqs. (A.31) to (A.33), the momentum equations simplify to

$$\partial_t\rho + \partial_x(\rho v_x) + \partial_y(\rho v_y) + \partial_z(\rho v_z) = 0, \tag{A.44}$$

$$\begin{aligned}\partial_t(\rho v_x) + \partial_x(\rho v_x v_x) + \partial_y(\rho v_x v_y) + \partial_z(\rho v_x v_z) = -\partial_x(\rho c_s^2) + F_x + \partial_x(2\nu[\partial_x(\rho v_x) - \frac{1}{3}\nabla\cdot(\rho\boldsymbol{v})] \\ +\xi\nabla\cdot(\rho\boldsymbol{v})) + \partial_y(\nu(\partial_x(\rho v_y) + \partial_y(\rho v_x))) + \partial_z(\nu(\partial_x(\rho v_z) + \partial_z(\rho v_x))) \\ -2G^2c^4\epsilon\partial_x(|\nabla\Psi|^2) + O(\partial^5),\end{aligned} \tag{A.45}$$

$$\begin{aligned}\partial_t(\rho v_y) + \partial_x(\rho v_x v_y) + \partial_y(\rho v_y v_y) + \partial_z(\rho v_y v_z) = -\partial_y(\rho c_s^2) + F_y + \partial_x(\nu(\partial_x(\rho v_y) + \partial_y(\rho v_x))) \\ +\partial_y(2\nu[\partial_y(\rho v_y) - \frac{1}{3}\nabla\cdot(\rho\boldsymbol{v})] + \xi\nabla\cdot(\rho\boldsymbol{v})) + \partial_z(\nu(\partial_y(\rho v_z) + \partial_z(\rho v_y))) \\ -2G^2c^4\epsilon\partial_y(|\nabla\Psi|^2) + O(\partial^5),\end{aligned} \tag{A.46}$$

$$\begin{aligned}\partial_t(\rho v_z) + \partial_x(\rho v_x v_z) + \partial_y(\rho v_y v_z) + \partial_z(\rho v_z v_z) = -\partial_z(\rho c_s^2) + F_z + \partial_x(\nu(\partial_x(\rho v_z) + \partial_z(\rho v_x))) \\ +\partial_y(\nu(\partial_y(\rho v_z) + \partial_z(\rho v_y))) + \partial_z(2\nu[\partial_z(\rho v_z - \frac{1}{3}\nabla\cdot(\rho\boldsymbol{v}))] + \xi\nabla\cdot(\rho\boldsymbol{v})) \\ -2G^2c^4\epsilon\partial_z(|\nabla\Psi|^2) + O(\partial^5),\end{aligned} \tag{A.47}$$

The bulk viscosity and kinematic viscosity in the multi-relaxation-time lattice Boltzmann model are given by

$$\xi = \frac{2}{9}(\frac{1}{s_2} - \frac{1}{2}), \tag{A.48}$$

and

$$\nu = \frac{1}{3}(\frac{1}{s_\beta} - \frac{1}{2}), \beta = 10, 12, 14, 15, 16. \tag{A.49}$$

Appendix B

Generation of porous media with specific global Minkowski functionals

The flow chart and MATLAB code for the generation of artificial porous media with specific Minkowski functionals are presented in this section.

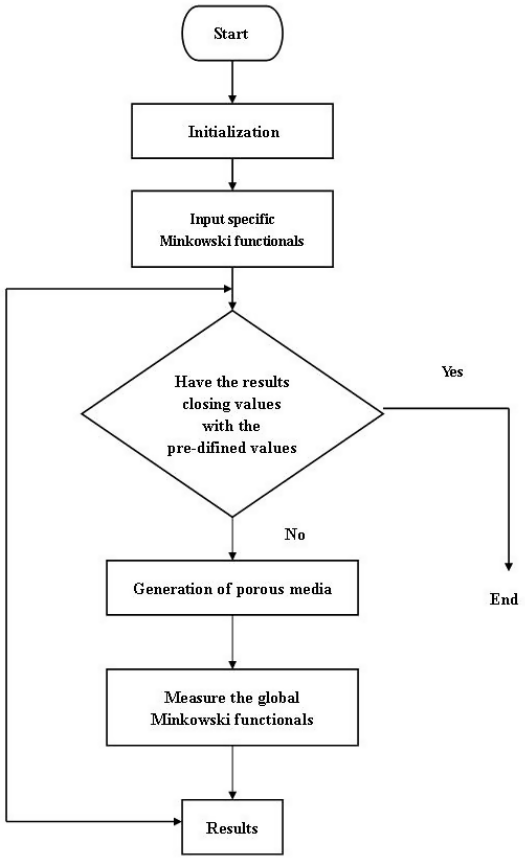

Figure B.1: Flow chart for the generation of the artificial porous media.

```
tic
clear
edge=0; % initial value of contour length
fraction=0; % initial value of solid fraction
solid_clusters=0; % initial value of solid cluster
while abs(solid_clusters-343)>3 % specify the solid clusters for the artificial porous media
edge=0;
fraction=0;
while abs(edge-0.0236)>0.00005 || abs(fraction-0.324)>0.0002 % specify the contour length and
solid fraction for the artificial porous media
lambda=0.0018; % the value of intensity of germs
sizeW=800; % domain size
noEvents=lambda*sizeW*sizeW;
noEvents=round(noEvents);
coords=rand(noEvents,2).*sizeW;
coords=round(coords);
obst=zeros(sizeW,sizeW);
[lx,ly]=size(obst);
[x,y] = meshgrid(1:lx,1:ly);
random_angle=rand(noEvents).*180;
random_angle=round(random_angle);
a=14; % length of long axis of ellipse
b=5; % length of short axis of ellipse
grain_number=size(coords,1);
for i=1:grain_number
center_x=coords(i,1);
center_y=coords(i,2);
Liquid=((x-center_x).*cos(random_angle(i))+(y-center_y).*sin(random_angle(i))).
^2/a^2+((y-center_y).*cos(random_angle(i))-(x-center_x).*sin(random_angle(i))).^2/b^2<=1;
bbRegion_Liquid=find(Liquid);
obst(bbRegion_Liquid)=1;
end
surface_area=0;
for i=1:lx
for j=1:ly
if obst(i,j)==1
surface_area=surface_area+1;
end
end
```

```
end
fraction=surface_area/sizeW/sizeW;
obst_fluid=zeros(lx,ly);
for i=1:lx
for j=1:ly
if obst(i,j)==0
obst_fluid(i,j)=1;
end
end
end
bbRegion_solid=find(obst);
size_solid=length(bbRegion_solid);
nearest_boundary=zeros(lx,ly);
obst2=circshift(obst_fluid,[1,0]);
obst3=circshift(obst_fluid,[0,1]);
obst4=circshift(obst_fluid,[-1,0]);
obst5=circshift(obst_fluid,[0,-1]);
obst6=circshift(obst_fluid,[1,1]);
obst7=circshift(obst_fluid,[-1,1]);
obst8=circshift(obst_fluid,[-1,-1]);
obst9=circshift(obst_fluid,[1,-1]);
for i=1:size_solid
if
obst2(bbRegion_solid(i))==1||obst3(bbRegion_solid(i))==1||obst4(bbRegion_solid(i))==1||
obst5(bbRegion_solid(i))==1||obst6(bbRegion_solid(i))==1||
obst7(bbRegion_solid(i))==1||obst8(bbRegion_solid(i))==1||obst9(bbRegion_solid(i))==1
nearest_boundary(bbRegion_solid(i))=1;
end
end
bbRegion_nearest=find(nearest_boundary);
size_nearest_boundary=length(bbRegion_nearest);
side_number=zeros(lx,ly);
side_number(bbRegion_nearest)=4;
obst2=circshift(obst,[-1,0]);
obst3=circshift(obst,[0,1]);
obst4=circshift(obst,[1,0]);
obst5=circshift(obst,[0,-1]);
for i=1:size_nearest_boundary
if obst2(bbRegion_nearest(i))==1
```

```
side_number(bbRegion_nearest(i))=side_number(bbRegion_nearest(i))-1;
end
if obst3(bbRegion_nearest(i))==1
side_number(bbRegion_nearest(i))=side_number(bbRegion_nearest(i))-1;
end
if obst4(bbRegion_nearest(i))==1
side_number(bbRegion_nearest(i))=side_number(bbRegion_nearest(i))-1;
end
if obst5(bbRegion_nearest(i))==1
side_number(bbRegion_nearest(i))=side_number(bbRegion_nearest(i))-1;
end
end
sum=0;
for i=1:size_nearest_boundary
sum=sum+side_number(bbRegion_nearest(i));
end
edge=sum/sizeW/sizeW/4;
end
save('800_0.32_0.0235_343.mat','obst');
mark_index=1;
while size_solid =0
mark_index=mark_index+1;
obst(bbRegion_solid(1))=mark_index;
bbRegion_solid(1)=0;
bbRegion_solid(find(bbRegion_solid==0))=[];
size_solid=length(bbRegion_solid);
k=0;
k1=1;
while k1-k>0
obst2=circshift(obst,[1,0]);
obst3=circshift(obst,[0,1]);
obst4=circshift(obst,[-1,0]);
obst5=circshift(obst,[0,-1]);
obst6=circshift(obst,[1,1]);
obst7=circshift(obst,[-1,1]);
obst8=circshift(obst,[-1,-1]);
obst9=circshift(obst,[1,-1]);
k=k1;
for i=1:size_solid
```

```
if obst2(bbRegion_solid(i))==mark_index || obst3(bbRegion_solid(i))==mark_index ||
obst4(bbRegion_solid(i))==mark_index
|| obst5(bbRegion_solid(i))==mark_index || obst6(bbRegion_solid(i))==mark_index ||
obst7(bbRegion_solid(i))==mark_index || obst8(bbRegion_solid(i))==mark_index ||
obst9(bbRegion_solid(i))==mark_index||
obst(bbRegion_solid(i))=mark_index;
bbRegion_solid(i)=0;
k1=k1+1;
end
end
bbRegion_solid(find(bbRegion_solid==0))=[];
size_solid=length(bbRegion_solid);
end
end
solid_clusters=mark_index-1;
end
toc
```

Appendix C

Measure of pore size distribution in artificial porous media

The flow chart and MATLAB code for the measure of the pore size distribution in the artificial porous media are presented in this section.

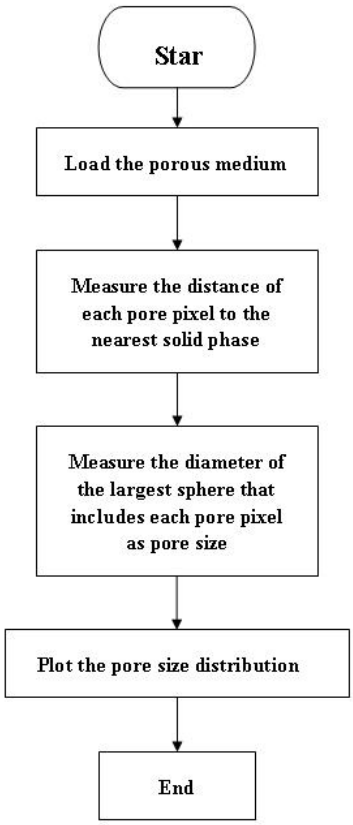

Figure C.1: Flow chart for determining the pore size distribution in the artificial porous media.

```
clear
load('obst.mat');
lx=2400;
ly=2400;
lx1=800;
ly1=800;
[x,y] = meshgrid(1:lx,1:ly);
number=0;
index_x_same_porous=zeros(1,lx1*ly1);
index_y_same_porous=zeros(1,lx1*ly1);
for i=1:lx1
for j=1:ly1
if obst(i,j) =1
number=number+1;
index_x_same_porous(1,number)=i;
index_y_same_porous(1,number)=j;
end
end
end
distance=zeros(1,number);
str1='/home/duo/duo/revision_paper4/group_2/800_0.3260_0.0247_456/pore_distance/mat';
for index=1:number
str2=[str1 num2str(index) '.mat'];
center_x=index_x_same_porous(1,index)+lx1;
center_y=index_y_same_porous(1,index)+ly1;
small_domain=zeros(lx1,ly1);
for radius=1:100
sphere=(x-center_y).^2+(y-center_x).^2<=radius.^2;
[index_x_bigdomain,index_y_bigdomain]=find(sphere);
number_sphere=size(index_x_bigdomain,1);
index_x_smalldomain=zeros(1,number_sphere);
index_y_smalldomain=zeros(1,number_sphere);
for i=1:number_sphere
if index_x_bigdomain(i)>=(lx1+1) && index_x_bigdomain(i)<=(2*lx1)
index_x_smalldomain(i)=index_x_bigdomain(i)-lx1;
end
if index_y_bigdomain(i)>=(ly1+1) && index_y_bigdomain(i)¡=(2*ly1)
index_y_smalldomain(i)=index_y_bigdomain(i)-ly1;
end
```

```
if index_x_bigdomain(i)>(2*lx1)
index_x_smalldomain(i)=index_x_bigdomain(i)-2*lx1;
end
if index_y_bigdomain(i)>(2*ly1)
index_y_smalldomain(i)=index_y_bigdomain(i)-2*ly1;
end
if index_x_bigdomain(i)<(lx1+1)
index_x_smalldomain(i)=index_x_bigdomain(i);
end
if index_y_bigdomain(i)<(ly1+1)
index_y_smalldomain(i)=index_y_bigdomain(i);
end
end
k=0;
for i=1:number_sphere
if obst(index_x_smalldomain(i),index_y_smalldomain(i))==1
k=1;
break
end
end
if k==1
distance(1,index)=radius;
bbRegion_sphere=sub2ind(size(small_domain),index_x_smalldomain,index_y_smalldomain);
break
end
end
save(str2,'bbRegion_sphere','radius');
end
str3='/home/duo/duo/revision_paper4/group_2/800_0.3260_0.0247_456/distance';
save(str3,'distance');
maximum=max(distance);
minimum=min(distance);
lx=800;
ly=800;
[x,y] = meshgrid(1:lx,1:ly);
number=0;
for i=1:lx
for j=1:ly
if obst(i,j) =1
```

```
number=number+1;
obst(i,j)=1;
else
obst(i,j)=0;
end
end
end
bbRegion_pore_space=find(obst);
for index=1:number
str2=[str1 num2str(index) '.mat'];
load(str2);
str4=['bbRegion_radius',num2str(radius)];
k=exist(eval('str4'),'var');
if k==0
eval(['bbRegion_radius',num2str(radius),'=','bbRegion_sphere',';'])
else
eval(['bbRegion_radius',num2str(radius),'=','[','bbRegion_radius',num2str(radius),';','bbRegion_sphere',']',';'])
end
end
bbRegion_pore_space=find(obst);
pore_volume_fraction=zeros(1,maximum);
for i=1:number
k=0;
for j=maximum:-1:minimum
k=any(eval(['any','(','bbRegion_radius',num2str(j),'==','bbRegion_pore_space(i)',')']));
if k==1
pore_volume_fraction(j)=pore_volume_fraction(j)+1; break
end
end
end
pore_volume_fraction=pore_volume_fraction/number;
pore_size=(minimum:1:maximum);
plot(pore_size,pore_volume_fraction,'-s');
pore_size_cumulative_distribution=zeros(1,maximum-minimum+1);
for i=1:1:maximum-minimum+1
pore_size_cumulative_distribution(i)=sum(pore_volume_fraction(i:maximum-minimum+1));
end
plot(pore_size,pore_size_cumulative_distribution,'-s');
```

List of Publications

1. D. Zhang and K. Papadikis and S. Gu. 2 Dimensional simulation of the hydrodeoxygenation of bio-oil in a trickle bed reactor. World Academy of Science, Engineering and Technology, 71:1617-1624, 2012.

2. D. Zhang and K. Papadikis and S. Gu. Application of a high density ratio lattice-Boltzmann model for the droplet impingement on flat and spherical surfaces. Int. J. Therm. Sci, 84:75-85, 2014.

3. D. Zhang and K. Papadikis and S. Gu. Investigations on the droplet impact onto a spherical surface with a high density ratio multi-relaxation time lattice-Boltzmann model. Commun. Comput. Phys, 16:892-912, 2014.

4. D. Zhang and K. Papadikis and S. Gu. Three-dimensional multi-relaxation time lattice-Boltzmann model for the drop impact on a dry surface at large density ratio. Int. J. Multiphase. Flow, 64:11-18, 2014.

5. D. Zhang and K. Papadikis and S. Gu. A lattice Boltzmann study on the impact of the geometrical properties of porous media on the steady state relative permeabilities on two-phase immiscible flows. Adv. Water Resour. (Submitted).

Bibliography

[1] A. L. Yarin. Drop impact dynamics: splashing, spreading, receding, bouncing...,. *Annu. Rev. Fluid Mech*, 38:159–192, 2006.

[2] R. Rioboo and C. Tropea. Outcomes from a drop impact on solid surfaces. *Atomization and Sprays*, 11:155–165, 2001.

[3] H. Darcy. *Les Fontaines Publiques da la Ville de Dijon.* Dalmont, Paris, 1856.

[4] M. Muskat and M. H. Meres. The flow of heterogeneous fluids through porous media. *Physics*, 7:346–363, 1936.

[5] J. F. Zhang. Lattice boltzmann method for microfluidics: models and applications. *Microfluid. Nanofluid*, 10:1–28, 2011.

[6] A. A. Mohamad. *Lattice Boltzmann Method.* Springer, 2011.

[7] E. D. Sloan A. K. Sum M. R. Walsh, C. A. Koh and D. T. Wu. Microsecond simuations of spontaneous methane hydrate nucleation and growth. *Science*, 326(5956):1095–1098, 2009.

[8] Y. Kobayashi S. Kiyoshima J. Shimizu, E. Ohmura and H. Eda. Molecular dynamics simulation of flattening process of a high-temperature, high-speed droplet-influence of impact parameters. *JTTEE5*, 16:722–728, 2007.

[9] G. Besold, I. Vattulainen, M. Kartunen, and J. M. Polson. Towards betterr integrators for dissipative particle dynamics simulations. *Phys Rev E*, 62:R7611–R7614, 2000.

[10] E. Monaco. *Multiphase lattice Boltzmann simulation of microfluidics.* PhD thesis, University of Southampton, School of Engineering Sciences, 2009.

[11] S. Wolfram. *Theory and applications of cellular automata.* World Scientific Publication, 1986.

[12] S. Succi. *The lattice Boltzmann equation.* Oxford University Press, Oxford, 2001.

[13] G. R. McNamara and G. Zanetti. Use of the boltzmann equation to simulate lattice-gas automata. *Phys. Rev. Lett*, 61(20):2332–2335, 1988.

[14] F. Higuera and J. Jimenez. Boltzmann approach to lattice gas simulations. *Europhys. Lett.*, 9(7):663–668, 1989.

[15] F. Higuera, S. Succi, and R. Benzi. Lattice gas dynamics with enhanced collison. *Europhys. Lett.*, 9(4):345–349, 1989.

[16] Y. H. Qian, D. d'Humieres, and P. Lallemand. Lattice-bgk models for navier-stokes equation. *Europhys. Lett.*, 17(6):479–484, 1992.

[17] P. Yuan and L. Schaefer. Equations of state in a lattice boltzmann model. *Phys. Fluids*, 18:042101, 2006.

[18] D. A. Drew and S. L. Passman. *Theory of multicomponent fluids.* Springer, New York, 1999.

[19] M. Ishii and T. Hibiki. *Thermo-fluid dynamics of two-phase flow.* Springer, New York, 2006.

[20] C. T. Crowe, M. Sommerfeld, and Y. Tsuji. *Multiphase flows with droplets and particles.* CRC Press, Boca Raton, 1998.

[21] S. Unverdi and G. Tryggvason. A front-tracking method for viscous, incompressible, multi-fluid flows. *J. Comput. Phys*, 100:25–37, 1992.

[22] M. Sussman, P. Smereka, and S. Osher. A level set approach for computing solutions to incompressible wwo-phase flow. *J. Comput. Phys*, 114:146–159, 1994.

[23] D. M. Anderson, G. B. McFadden, and A. A. Wheeler. Diffuse-interface methods in fluid mechanics. *Annu. Rev. Fluid Mech*, 30:139–165, 1998.

[24] D. Jacqmin. Calculation of two-phase navier-stokes flows using phase-field modeling. *J. Comput. Phys*, 155(1):96–127, 1999.

[25] S. W. J. Welch. Local simulation of two-phase flows including interface tracking with mass transfer. *J. Comput. Phys*, 121(1):142–154, 1995.

[26] H. H. Hu, N. A. Patankar, and M. Y. Zhu. Direct numerical simulations of fluid-solid systems using the arbitrary lagrangian-eulerian technique. *J. Comput. Phys*, 169(2):427–462, 2001.

[27] S. Quan and D. P. Schmidt. A moving mesh interface tracking method for 3d incompressible two-phase flows. *J. Comput. Phys*, 221(2):761–780, 2007.

[28] S. Ganesan and L. Tobiska. An accurate finite element scheme with moving meshes for computing 3d-axisymmetric interface flows. *Int. J. Numer. Methods. Fluids*, 57(2):119–138, 2008.

[29] S. Quan, J. Lou, and D. P. Schmidt. Modeling merging and breakup in the moving mesh interface tracking method for multiphase flow simulations. *J. Comput. Phys*, 228(7):2660–2675, 2009.

[30] R. Scardovelli and S. Zaleski. Direct numerical simulation of free-surface and interfacial flow. *Ann. Rev. Fluid Mech*, 31:67–603, 1999.

[31] S. Osher and R. P. Fedkiw. Level set methods: an overview and some recent results. *J. Comput. Phy*, 169:463–502, 2001.

[32] J. A. Sethian and P. Smereka. Level set methods for fluid interfaces. *Ann. Rev. Fluid Mech*, 35:341–372, 2003.

[33] G. Tryggvason, B. Bunner, A. Esmaeeli, D. Juric, N. Al-Rawahi, W. Tauber, J. Han, S. Nas, and Y. J. Jan. A front-tracking method for the computations of multiphase flow. *J. Comput. Phys*, 169:708–759, 2001.

[34] C. W. Hirt and B. D. Nichols. Volume of fluid (vof) methods for the dynamics of free boundaries. *J. Comput. Phys*, 39:201–225, 1981.

[35] M. Rudman. Volume-tracking methods for interfacial flow calculations. *Int. J. Numer. Methods. Fluids*, 24(7):671–691, 1997.

[36] S. T. Zalesak. Fully multidimensional flux-corrected transport algorthms for fluids. *J. Comput. Phys*, 31(3):335–362, 1979.

[37] T. Bonometti and J. Magnaudet. An interface-capturing method for imcompressible two-phase flows. validation and application to bubble dynamics. *Int. J. Multiph. Flow*, 33(2):109–133, 2007.

[38] E. Olsson and G. Kreiss. A conservative level set method for two phase flow. *J. Comput. Phys*, 210(1):225–246, 2005.

[39] E. Olsson, G. Kreiss, and S. Zahedi. A conservative level set method for two phase flow ii. *J. Comput. Phys*, 225:785–807, 2007.

[40] V. E. Badalassi, H. D. Ceniceros, and S. Banerjee. Computation of multiphase systems with phase field models. *J. Comput. Phys*, 190:371–397, 2003.

[41] S. Chen and G. Doolen. Lattice boltzmann method for fluid flows. *Annu. Rev. Fluid Mech*, 30:329–364, 1998.

[42] S. Hou, X. Shan, Q. Zou, G. D. Doolen, and W. Soll. Evaluation of two lattice boltzmann models for multiphase flows. *J. Comput. Phys*, 138:695–713, 1997.

[43] D. H. Rothman and J. M. Keller. Immiscible cellular-automation fluids. *J. Stat. Phys*, 52:1119–1129, 1988.

[44] A. K. Gunstensen, D. H. Rothman, S. Zaleski, and G. L. G. Zanetti. Lattice boltzmann model of immiscible fluids. *Phys. Rev. A*, 43:4320–4327, 1991.

[45] X. Shan and H. Chen. Simulation of nonideal gases and liquid-gas phase transitions by the lattice boltzmann equation. *Phys. Rev. E*, 49:2941–2948, 1994.

[46] M. R. Swift, E. Orlandini, W. R. Osborn, and J. M. Yeomans. Lattice boltzmann simulations of liquid-gas and binary fluid systems. *Phys. Rev. E*, 54:5041–5052, 1996.

[47] X. He, S. Chen, and R. Zhang. A lattice boltzmann scheme for incopressible multiphase flow and its application in simulation of rayleigh-taylor instbility. *J. Comput. Phys*, 152:642–663, 1999.

[48] L. O. E. Santos, P. C. Facin, and P. C. Philippi. Lattice-boltzmann model based on field mediators for immiscible fluids. *Phys. Rev. E*, 68:056302, 2003.

[49] D. Grunau, S. Chen, and K. Eggert. A lattice boltzmann model for multiphase fluid flows. *Physics of Fluids A: Fluid Dynamics*, 5(10):2557–2562, 1993.

[50] S. V. Lishchuk, C. M. Care, and I. Halliday. Lattice boltzmann algorithm for surface tension with greatly reduced microcurrents. *Physical review E*, 67:036701, 2003.

[51] M. Latva-Kokko and D. H. Rothman. Diffusion properties of gradient-based lattice boltzmann models of immiscible fluids. *Physical review E*, 71:056702, 2005.

[52] T. Reis and T. N. Phillips. Lattice boltzmann model for simulating immiscible two-phase flows. *J. Phys. A. Math. Theor*, 40:4033–4053, 2007.

[53] H. Liu and A. J. Valocchi. Three-dimensional lattice boltzmann model for immiscible two-phase flow simulations. *Phys. Rev. E*, 85:046309, 2012.

[54] S. Leclaire, M. Reggio, and J. Y. Trepanier. Numerical evaluation of two recoloring operators for an immiscible two-phase flow lattice boltzmann model. *Appl. Math. Model*, 36:2237–2252, 2012.

[55] S. Leclaire, N. Pellerin, M. Reggio, and J-Y. Trepanier. Unsteady immiscible multiphase flow validation of a multiple-relaxation-time lattice boltzmann method. *J. Phys. A: Math. Theor.*, 47:105501, 2014.

[56] X. Shan. Analysis and reduction of the spurious current in a class of multiphase lattice boltzmann models. *Phys. Rev. E*, 73:047701, 2006.

[57] M. Sbragaglia, R. Benzi, L. Biferale, S. Succi, K. Sugiyama, and F. Toschi. Generalized lattice boltzmann method with multirange pseudopotential. *Phys. Rev. E*, 75:026702, 2007.

[58] Z. L. Guo, C. G. Zheng, and B. C. Shi. Discrete lattice effects on the forcing term in the lattice boltzmann method. *Phys. Rev. E*, 65:046308, 2002.

[59] A. L. Kupershtokh, D. A. Medvedev, and D. I. Karpov. On equations of state in a lattice boltzmann method. *Comput. Math. Appl*, 58:965–974, 2009.

[60] Q. Li, K. H. Luo, and X. J. Li. Forcing scheme in pseudopotential lattice boltzmann model multiphase flows. *Phys. Rev. E*, 86:016709, 2012.

[61] S. Mukherjee and J. Abraham. A pressure-evolution-based multi-relaxation-time high-density-ratio two-phase lattice-boltzmann model. *Comput. Fluids*, 36:1149–1158, 2007.

[62] A. Fakhari and T. Lee. Multiple-relaxation-time lattice boltzmann method for immiscible fluids at high reynolds numbers. *Phys. Rev. E*, 87:023304, 2013.

[63] Q. Li, K. H. Luo, and X. J. Li. Lattice boltzmann modeling of multiphase flows at large density ratio with an improved pseudopotential model. *Phys. Rev. E*, 87:053301, 2013.

[64] A. N. kalarakis, V. N. Burganos, and A. C. Payatakes. Galilean-invariant lattice-boltzmann simulation of liquid-vapor interface dyanmics. *Phys. Rev. E*, 65:056702, 2002.

[65] A. N. kalarakis, V. N. Burganos, and A. C. Payatakes. Three-dimensional lattice-boltzmann model of van der waals fluids. *Phys. Rev. E*, 67:016702, 2003.

[66] T. Inamuro, T. Ogata, S. Tajima, and N. Konishi. A lattice boltzmann method for incompressible two-phase flows with large density differences. *J. Comput. Phys*, 198:628–644, 2004.

[67] Y. Y. Yan and Y. Q. Zu. A lattice boltzmann method for incompressible two-phase flows on partial wetting surface with large density ratio. *J. Comput. Phys*, 227:763–775, 2007.

[68] A. J. Briant, P. Papatzacos, and J. M. Yeomans. Lattice boltzmann simulations of contact line motion in a liquid-gas system. *Philos. Trans. R. Soc. Lond. A*, 360:485–495, 2002.

[69] X. Y. He, X. W. Shan, and G. D. Doolen. Discrete boltzmann equation model for nonideal gases. *Phys. Rev. E*, 57:R13(R), 1998.

[70] T. Lee and L. Lin. Lattice boltzmann simulations of micron-scale drop impact on dry surfaces. *J. Comput. Phys*, 229:8045–8063, 2010.

[71] T. Lee and C. L. Lin. A stable discretization of the lattice boltzmann equation for simulaton of incompressible two-phase flows at high density ratio. *J. Comput. Phys*, 206:16–47, 2005.

[72] H. W. Zheng, C. Shu, and Y. T. Chew. Lattice boltzmann interface capturing method for incompressible flows. *Phys. Rev. E*, 72:056705, 2005.

[73] H. W. Zheng, C. Shu, and Y. T. Chew. A lattice boltzmann model for multiphase flows with large density ratio. *J. Comput. Phys*, 218:353–371, 2006.

[74] A. Fakhari and M. H. Rahimian. Phase-field modeling by the method of lattice boltzmann equations. *Phys. Rev. E*, 81:036707, 2010.

[75] J. Y. Shao, C. Shu, H. B. Huang, and Y. T. Chew. Free-energy-based lattice boltzmann model for the simulation of multiphase flows with density contrast. *Phys. Rev. E*, 89:033309, 2014.

[76] Y. Q. Zu and S. He. Phase-field-based lattice boltzmann model for incompressible binary fluid systems with density and viscosity contrasts. *Phys. Rev. E*, 87:043301, 2013.

[77] H. Liang, B. C .Shi, Z. L. Guo, and Z. H. Chai. Phase-field-based multiple-relaxation-time lattice boltzmann model for incompressible multiphase flows. *Phys. Rev. E*, 89:053320, 2014.

[78] M. Rein. Phenomena of liquid drop impact on solid and liquid surface. *Fluid. Dyn. Res*, 12:61–93, 1993.

[79] R. Rioboo, M. Marengo, and C. Tropea. Time evolution of liquid drop impact onto solid, dry surfaces. *Exp. Fluids*, 33:112–124, 2002.

[80] A. Asai, M. Shioya, S. Hirasawa, and T. Okazaki. Impact of an ink drop on paper. *J. Imaging Sci. Technol*, 37:205–207, 1993.

[81] B. L. Scheller and D. W. Bousfield. Newtonian drop impact with a solid surface. *AIChE J*, 41:1357–1367, 1995.

[82] S. Chandra and C. T. Avedesian. On the collision of a droplet with a solid surface. *Proc. R. Soc. Lond. Ser. A*, 432:13, 1991.

[83] M. Pasandideh-Fard, Y. M. Qiao, S. Chandra, and J. Mostaghimi. Capillary effects during droplet impact on a solid surface. *Phys. Fluids*, 8:650–660, 1996.

[84] T. Mao, D. C. S. Kuhn, and H. Tran. Spread and rebound of liquid droplets upon impact on flat surfaces. *AIChE J*, 43:2169–2179, 1997.

[85] I. V. Roisman, R. Rioboo, and C. Tropea. Normal impact of a liquid drop on a dry surface: model for spreading and receding. *Proc. R. Soc. Lond. Ser. A*, 458:1411–1430, 2002.

[86] H. Dong, W. W. Carr, D. G. Bucknall, and J. F. Morris. Temporally-resolved inkjet drop impaction on surfaces. *AIChE J*, 53:2606–2617, 2007.

[87] L. S. Hung and S. C. Yao. Experimental investigation of the impaction of water droplets on cylindrical objects. *Int. J. Multiphase Flow*, 25:1545–1559, 1999.

[88] Y. Hardalupas, A. M. K. P. Taylor, and J. H. Wilkins. Experimental investigation of submillimeter droplet impingement onto spherical surfaces. *Int. J. Heat Fluid Flow*, 20:477–485, 1999.

[89] S. Bakshi, L. V. Roisman, and C. Tropea. Investigations on the impact of a drop onto a small spherical target. *Phys. Fluids*, 19:032102, 2007.

[90] S. Mukherjee. *Simulation of Wall Impinging Drops*. PhD thesis, School of Mechanical Engineering, Purdue University, 2006.

[91] G. Trapaga and J. Szekely. Mathematical modeling of the isothermal impingement of liquid droplets in spraying processes. *Metall. Trans. B*, 22:901–914, 1991.

[92] M. Bussmann and S. Afkhami. Drop impact simualtion with a velocity-dependent contact angle. *Chem. Eng. Sci*, 62:7214, 2007.

[93] M. Pasandideh-Fard, M. Bussmann, S. Chandra, and J. Mostaghimi. Simulating droplet impact on a substrate of arbitrary shape. *Atomization Spray*, 11:397–414, 2001.

[94] H. Liu, S. Krishnan, S. Marella, and H. S. Udaykumar. Sharp interface cartesian grid method ii: A technique for simulating droplet interactions with surfaces of arbitrary shape. *J. Comput. Phys*, 210:32–54, 2005.

[95] Y. Ge and L. S. Fan. Droplet-particle collison mechanics with film-boiling evaporation. *J. Fluid Mech*, 573:331–337, 2007.

[96] A. Gupta and R. Kumar. Droplet impingement and breakup on a dry surface. *Comput. Fluids*, 39:1696–1703, 2010.

[97] A. Gupta and R. Kumar. Two-dimensional lattice boltzmann model for droplet impingement and breakup in low density ratio liquids. *Comm. Comp. Phys*, 10:767–784, 2011.

[98] S. Q. Shen, F. F. Bi, and Y. L. Guo. Simulation of droplets impact on curved surfaces with lattice boltzmann method. *Int. J. Heat Mass Trans*, 55:6938–6943, 2012.

[99] Y. Bachmat and J. Bear. Macroscopic modelling of transport phenomena in porous media. 1: The continuum approach. *Transp. Porous Media*, 1(3):213–240, 1986.

[100] S. Whitaker. Flow in porous media i: A theoretical derivation of darcy's law. *Transp. Porous Media*, 1:3–25, 1986.

[101] W. G. Gray. Thermodynamics and constitutive theory for multiphase porous-media flow considering internal geometric constraints. *Adv. Water Resour*, 22(5):521–547, 1999.

[102] C. M. Marle. On macroscopic equations governing multiphase flow with diffusion and chemical reactions in porous media. *Int. J. Eng. Sci*, 20(5):643–662, 1982.

[103] F. Kalaydjian. A macroscopic description of multiphase flow in porous media involving spacetime evolution of fluid/fluid interface. *Transp. Porous Media*, 2:537–552, 1987.

[104] F. Kalaydjian. Origin and quantification of coupling between relative permeabilities for two-phase flows in porous media. *Transp. Porous Media*, 5(3):215–229, 1990.

[105] W. G. Gray and C. T. Miller. Thermodynamically constrained averaging theory approach for modeling of flow in porous media: 1. motivation and overview. *Adv. Water Resour*, 28(2):161–180, 2005.

[106] C. T. Miller and W. G. Gray. Thermodynamically constrained averaging theory approach for modeling flow and transport phenomena in porous medium systems: 2. foundation. *Adv. Water Resour*, 28:181–202, 2005.

[107] A. Jackson, C. Miller, and W. Gray. Thermodynamically constrained averaging theory approach for modeling flow and transport phenomena in porous medium systerms: 6. two-fluid-phase flow. *Adv. Water Resour*, 32(6):779–795, 2009.

[108] S. M. Hassanizadeh and W. G. Gray. Mechanics and thermodynamics of multiphase flow in porous media including interphase boundaries. *Adv. Water Resour*, 13(4):169–186, 1990.

[109] R. Bowen. Compressible porous media models by use of the theory of mixtures. *Int. J. Eng. Sci*, 20(6):697–735, 1982.

[110] D. G. Avraam and A. C. Payatakes. Flow regimes and relative permeabilities during steady-state two-phase flow in porous media. *J. Fluid Mech*, 293:207–236, 1995a.

[111] D. G. Avraam and A. C. Payatakes. Generalized relative permeability coefficients during steady-state two-phase flow in porous media, and correlation with the flow mechanisms. *Trans. Porous Media*, 20:135–168, 1995b.

[112] D. G. Avraam and A. C. Payatakes. Flow mechanics, relative permeabilities, and coupling effects in steady-state two-phase flow through porous media, the case of strong wettability. *Ind. Eng. Chem. Res*, 38:778–786, 1999.

[113] C. D. Tsakiroglou, D. G. Avraam, and A. C. Payatakes. Transient and steady-state relative permeabilities from two-phase flow experiments in planar pore networks. *Adv. Water Resour*, 30:1981–1992, 2007.

[114] C. D. Tsakiroglou, M. Theodoropoulou, and V. Karoutsos. Non-equilibrium capillary pressure and relative permeability curves of porous media. *AIChE J*, 49:2472–2486, 2003.

[115] C. D. Tsakiroglou, M. Theodoropoulou, and V. Karoutsos. Determination of the effective transport coefficients of pore networks from transient immiscible and miscible displacement experiments. *Water Resour. Res*, 41(2):W02014, 2005.

[116] C. A. Aggelopoulos and C. D. Tsakiroglou. The effect of micro-heterogeneity and capillary number on capillary pressure and relative permeability curves of soils. *Geoderma*, 148:25–34, 2008.

[117] B. Ataie-Ashtiani, S. M. Hassanizadeh, M. Oostrom, M. A. Celia, and M. D. White. Effective parameters for two-phase flow in a porous medium with peridic heterogeneities. *J. Contam. Hydrol*, 49:87–109, 2001.

[118] B. Ataie-Ashtiani, S. M. Hassanizadeh, and M. A. Celia. Effects of heterogeneities on capillary pressure-saturation-relative permeability relationships. *J. Contam. Hydrol*, 56:175–192, 2002.

[119] B. Ataie-Ashtiani, S. M. Hassanizadeh, O. Oung, F. A. Weststrate, and A. Bezuijen. Numerical modelling of two-phase flow in a geocentrifuge. *Environ. Modell. Softw*, 18:231–241, 2003.

[120] D. B. Das, S. M. Hassanizadeh, B. E. Rotter, and B. Ataie-ashtiani. A numerical study of micro-heterogeneity effects on upscaled properties of two-phase flow in porous media. *Trans. Porous. Media*, 56:329–350, 2004.

[121] D. B. Das, M. Mirzaei, and N. Widdows. Non-uniqueness in capillary pressure-saturation-relative permeability relationships for two-phase flow in porous media: interplay between intensity and distribution of random micro-heterogeneities. *Chem. Eng. Sci*, 61:6786–6803, 2006.

[122] A. Q. Raeini, M. J. Blunt, and B. Bijeljic. Modelling two-phase flow in porous media at the pore scale using volume-of-fluid method. *J. Comput. Phys*, 231:5653–5668, 2012.

[123] M. Ahmadlouydarab, Z. S. Liu, and J. J. Feng. Relative permeability for two-phase flow through corrugated tubes as model porous media. *Int. J. Multiph. Flow*, 47:85–93, 2012.

[124] H. A. Amiri and A. Hamouda. Evaluation of level set and phase field methods in modeling two phase flow with viscosity contrast through dual-permeability porous medium. *Int. J. Multiph. Flow*, 52:22–34, 2013.

[125] M. J. Blunt, M. D. Jackson, M. Piri, and P. H. Valvatne. Detailed physics, predictive capabilities and macroscopic consequences for pore-network models of multiphase flow. *Adv. Water Resour*, 25:1069–1089, 2002.

[126] D. B. Slin and T. W. Patzek. Pore space morphology analysis using maximal inscribed spheres. *Physica A: Statistical and Theoretical Physics*, 371(2):336–360, 2006.

[127] Z. Jiang, K. Wu, G. Couples, M. I. J. vanDijke, K. S. Sorbie, and J .Ma. Efficient extraction of networks from three-dimensional porous media. *Water Resour. Res*, 43:W12S03, 2007.

[128] V. Joekar-Niasar, S. M. Hassanizadeh, and A. Leijnse. Insights into the relationships among capillary pressure, saturation, interfacial area and relative permeability using pore-network modeling. *Transp. Porous Media*, 74(2):201–219, 2008.

[129] V. Joekar-Niasar, S. M. Hassanizadeh, and H. K. Dahle. Non-equilibrium effects in capillarity and interfacial area in two-phase flow: dynamic pore-network modelling. *J. Fluid Mech*, 655:38–71, 2010.

[130] V. Joekar-Niasar and S. M. Hassanizadeh. Effect of fluids properties on non-equilibrium capillarity effects: dynamic pore-network modeling. *Int. J. Multiphase Flow*, 37:198–214, 2011.

[131] V. Joekar-Niasar and S. M. Hassanizadeh. Uniqueness of specific interfacial area-caplillary pressure-saturation relationship under non-equilibrium conditions in two-phase porous media flow. *Transp. Porous Media*, 94:465–486, 2012.

[132] C. K. Aidun and J. R. Clausen. Lattice-boltzmann method for complex flows. *Annu. Rev. Fluid Mech*, 42(1):439–472, 2010.

[133] A. K. Gunstensen and D. H. Rothman. Lattice-boltzmann studies of immiscible two-phase flow through porous media. *J. Geophys. Res. & Solid Earth*, 98(B4):6431–6441, 1993.

[134] H. Li, C. Pan, and C. T. Miller. Pore-scale investigation of viscous coupling effects for two-phase flow in porous media. *Phys. Rev. E*, 72:026705, 2005.

[135] A. G. Yiotis, J. Psihogios, M. E. Kainourgiakis, A. Papaioannou, and A. K. Stubos. A lattice boltzmann study of viscous coupling effects in immiscible two-phase flow in porous media. *Colloid Surface A*, 300:35–49, 2007.

[136] H. B. Huang, H. W. Zheng, X. Y. Lu, and C. Shu. An evaluation of a 3d free-energy-based lattice boltzmann model for multiphase flows with large density ratio. *Int. J. Numer. Meth. Fluids*, 63:1193–1207, 2009.

[137] Z. Dou and Z. F. Zhou. Numerical study of non-uniqueness of the factors influencing relative permeability in heterogeneous porous media by lattice boltzmann method. *Int. J. Heat Fluid Flow*, 42:23–32, 2013.

[138] A. G. Yiotis, L. Talon, and D. Salin. Blob population dynamics during immiscible two-phase flows in reconstructed porous media. *Phys. Rev. E*, 87:033001, 2013.

[139] D. A. Perumal and A. K. Dass. Application of lattice boltzmann method for incompressible viscous flows. *Appl. Math. Model*, 37:4075–4092, 2013.

[140] Z. Yu and L. S. Fan. Multirelaxation-time interaction-potential-based lattice boltzmann model for two-phase flow. *Phys. Rev. E*, 82:046708, 2010.

[141] K. N. Premnath and J. Abraham. Three-dimensional multi-relaxation time (mrt) lattice-boltzmann models for multiphase flow. *J. Comput. Phys*, 224:539–559, 2007.

[142] M. E. McCracken and J. Abraham. Multiple-relaxation-time lattice-boltzmann model for multiphase flow. *Phys. Rev. E*, 71:036701, 2005.

[143] C. H. Arns, M. A. Knackstedt, and K. R. Meche. Reconstructing complex materials via effective grain shapes. *Phys. Rev. Lett*, 91:215506, 2003.

[144] C. H. Arns, M. A. Knackstedt, W. V. Pinczewski, and K. R. Mecke. Euler-poincare characteristics of classes of disordered media. *Phys. Rev. E*, 63:031112, 2001.

[145] H. J. Vogel. Morphological determination of pore connectivity as a function of pore size using serial sections. *Eur J Soil Sci*, 48:365–377, 1997.

[146] K. R. Mecke. Morphology of spatial patterns: porous media, spinodal decomposition, and dissipative structures. *Acta Physica Polonica B*, 28:1747–1782, 1997.

[147] K. R. Mecke. Additivity, convexity and beyond: applications of minkowski functionals in statistical physics. *Lect Notes Phys*, 554:111–184, 2000.

[148] A. L. Herring, E. J. Harper, E. A. Andersson, A. Sheppard, B. K. Bay, and D. Wildenschild. Effect of fluid topology on residual nonwetting phase trapping: Implications for geologic co2 sequestration. *Adv. Water Resour*, 62:47–58, 2013.

[149] D. Stoyan, W. S. Kendall, and J. Mecke. *Stochastic geometry and its application.* John Wiley and Sones, 1992.

[150] G. D. Prisco, J. Toelke, and M. R. Dernaika. Computation of relative permeability functions in 3d digital rocks by a fractional flow approach using the lattice boltzmann method. *International Symposium of the Society of Core Analysts, Aberdeen, Scotland, UK, August 27th-30th*, SCA:36, 2012.

[151] S. Berg, A. W. Cense, J. P. Hofman, and R. M. M. Smits. Two-phase flow in porous media with slip boundary condition. *Transp Porous Med*, 74:275–292, 2008.

[152] C. Scholz, F. Wirner, J. Gotz, Ulrich Rude, G. E. Schroder-Turk, K. Mecke, and C. Bechinger. Permeability of porous materials determined from the euler characteristic. *Phys. Rev. Lett*, 109:264504, 2012.

[153] X. He and L. S. Luo. Lattice boltzmann model for the incompressible navier-stokes equation. *J. Stat. Phys*, 88:927–944, 1997.